Developing Gold Nanocluster Based Cancer Theranostics

A Thesis

Submitted in partial fulfilment for the award of degree of

Doctor of Philosophy

By

Bandhan Chatterjee

Centre for Nanotechnology

Indian Institute of Technology Guwahati

Assam, India,

January 2018

Dedicated to My Parents

DECLARATION

This thesis entitled "**Gold nanoclusters based Nanotheranostics for Cancer Therapeutics**" is a work of research and investigation carried out under the supervision of Prof. Arun Chattopadhyay, Department of Chemistry, Indian Institute of Technology Guwahati and Prof. Siddhartha Sankar Ghosh, Department of Biosciences and Bioengineering, Indian Institute of Technology Guwahati. This thesis has been submitted to the Centre for Nanotechnology, Indian Institute of Technology Guwahati for the award of the degree of Doctor of Philosophy. I further declare that this work has not been submitted anywhere else for any degree, diploma, associateship or membership etc. at any Institute or University to the best of my knowledge.

Centre for Nanotechnology

Indian Institute of Technology Guwahati

Assam, India,

Bandhan Chatterjee

Roll No. 126153006

January 2018

INDIAN INSTITUTE OF TECHNOLOGY GUWAHATI

CERTIFICATE

This is to certify that this thesis entitled "**Gold Nanoclusters based Nanotheranostics for Cancer Therapeutics**" has been submitted by **Bandhan Chatterjee** (Roll No. **126153006**) to **Indian Institute of Technology Guwahati** for the award of the degree of **Doctor of Philosophy in Nanotechnology**. This thesis is a record of the bonafide research work carried out by him during his degree tenure. The findings presented here are purely derived from his own research work. He has meticulously performed the research and has been ardently adherent of lab protocols. This work in parts or as a whole is novel and is not been produced in any previous diploma or degree.

Prof. Siddhartha Sankar Ghosh (Supervisor)

Prof. Arun Chattopadhyay (Supervisor)

Acknowledgement

This is a rather futile job to carve out on paper, my gratitude and appreciation for people and the institute which bore me for 5 years, people who stood by me through my thick and thin and made me person that I am today. Nevertheless, I must try…

First and foremost, I would like to expresses my sincerest gratitude towards my mentors Prof. Arun Chattopadhyay and Prof. Siddhartha Sankar Ghosh for their relentless guidance and moral support that they have comforted me with during this whole journey. There were times when I was literally broken and was frustrated but both of them counselled me through these though times. You sirs, have taught me the value of patience and endurance, result of which is that I am able to complete my degree. You sirs have instilled scientific virtues and practises needed for this arduous job and have rendered me the freedom to explore my own potential and developed the ability to work both independently as well as in collaborative projects. Your guidance not only in experiment designs but also through the writing parts made things possible for me.

Further I would like to mention the incredible suggestions made by doctoral committee members Dr. Biplab Bose, Dr. Lal Mohan Kundu, Dr. Chandan K Jana throughout my Ph.D. They took keen interest in fundamental aspects of my work in and have constantly provided constructive critique which enabled my work to progress in a more scientific manner.

I would also like to express my gratitude towards the whole office staff of Centre for Nanotechnology for their endless support and help whenever I needed it. I would also like to express my gratitude towards CIF, IIT Guwahati, for they have provided me with the critical instrumentation facility like FESEM, FETEM, AFM, MALDI TOF, TRPL.

ESI MS. I also very grateful to Department of Biosciences and Bioengineering and Department of Chemistry for their letting me avail their instrumentation facility.

I would like mention the instrumental contributions of my lab mates (Upashi Goswami, Dr. Sunil Kumar Sailapu, Deepanjalee Dutta, Dr. Madhumita Das, Anitha. T. Simon and Debashree Debasmita and my seniors (Dr. Shilpa Sharma, Dr. Amit Jaiswal, Dr. Amaresh Kumar Sahoo, Dr. Rumi Khandelia, Dr. Satyapriya Bhandari, Anushree Dutta, Dr. Chockalingam, Dr. Subhomoy and Dr. Archita Ghosal during this whole journey. I am also indebted to my other group members, Shilaj, Sabyasachi, Uday, Srestha, Kafeel, Dr. Sharmila, Dr. Asif Raza, Neha, Anil, Srirupa and Rajib for their generous support.

I would like to acknowledge my gratitude towards my friends, Ashish, Rajul, Vinayak, Gowtham, Abhinav, Franklin, Shayan, Anil, Amrutha, Poloumi, Sandipan, Satyendra, Mahesh, K.K., Bapi, Subhajit, Deepojwal, Amritava, Oritro, Krishna and Anirban.

Last but not least I express my sincerest gratitude towards my parents and relatives for their constant support.

I thank you all with sincerest gratitude, without you all this journey would have not been possible for me.

Bandhan Chatterjee

CONTENTS

Abstract ..... **i - ii**

List of Abbreviations ..... **iii - iv**

Chapter 1: Introduction and Review of Literature

1.1. Introduction 3-4
1.2. Cancer: An old relic or a human made omen 4-6
1.3. Theranostics 6-15
  1.3.1 Immune Nanotheranostics 8-9
  1.3.2 Nanocluster based Theranostics 9-15
1.4. Targeting strategies 15-18
  1.4.1 Passive targeting 16
  1.4.2 Active targeting 17
  1.4.3 Stimuli responsive Nanoparticles 17-18
1.5. Objectives of the thesis 19-20
1.6. Outline of the thesis 20-22
1.7. References 22-28

Chapter 2: Interactive Luminescent Gold Nanocluster Embedded dsDNA and Cisplatin as Model Nanoparticles for Cancer Theranostics.

2.1. Introduction 31-33
2.2. Outline of the research work 33-35
2.3. Experimental section 35-39
2.4. Results and discussion 40-52
2.5. Conclusions 53
2.6. References 53-56

Chapter 3: dGTP Templated Luminescent Gold Nanocluster Based Composite Nanoparticles for Cancer Theranostics

3.1. Introduction 59-61
3.2. Outline of the research work 61-63
3.3. Experimental section 63-68
3.4. Results and discussion 68-82
3.5. Conclusions 83
3.6. References 83-87

Chapter 4: Developing single entity theranostic: Drug based fluorescent nanoclusters with augmented cytotoxicity

4.1. Introduction 91-92
4.2. Outline of the research work 92-94
4.3. Experimental section 94-96
4.4. Results and discussion 96-106
4.5. Conclusions 107
4.6. References 107-110

Chapter 5: Evaluating the potential of the MTX NCs to replace MTX on a Drug Delivery Platform

5.1. Introduction 113-114
5.2. Outline of the research work 114-115
5.3. Experimental section 115-118
5.4. Results and discussion 118-125
5.5. Conclusions 125-126
5.6. References 126-128

Chapter 6: Conclusions and Future Outlook

6.1. Summary of the Present Work 131-132
6.2. Future Outlook 132

Publications and Presentations 135

Permissions 139-140

ABSTRACT

Nanotheranostic, a combination of diagnostic and therapeutic modalities at a nanoscale range offers a promising prospect in cancer therapeutics. Besides having the edges offered by the nanomaterials, it further refutes the need of separate units for individual modalities. The current thesis work is to develop novel nanoscale theranostic materials as potential candidates for their further clinical translation.

The thesis is organised in six chapters. The first Chapter (Chapter 1) provides a holistic but comprehensive description about the need and basics of theranostics and current state of cancer theranostics. It also provides a comprehensive introduction of nanoclusters as majority of theranostic developed here are nanocluster based. The chapter also provides the background and objectives of the thesis.

Chapter 2 describes the development of DNA (plasmid DNA) based smart theranostics for cancer therapy. The chapter entails the development of the DNA templated Au NCs and their further use in conjugation with cisplatin (anti-cancer drug) for developing composite NPs. Further these composite NPs were thoroughly characterized with various analytical instruments. The composite NPs were stable and had bright fluorescent with decent quantum yield. The composite NPs were readily taken up the HeLa cells and inflicted augmented cytotoxicity on the host cells while bioimaging them simultaneously. The composite NPs also have on demand loading capacity and pH dependent release profile.

Chapter 3 deals with the synthesis of fluorescent gold nanocluster on dGTP, a small molecule. It should be borne here that whereas the previous work has gold nanocluster templated on DNA (have myriad of bases in it), this work is about stabilizing the gold nanocluster on a nucleotides (dGTP) rather the polymer of it. The

dGTP templated Au NCs displayed impressive physical characteristics deemed of an imaging moiety and was further interacted with cisplatin to form theranostic composite NPs, which were further coated with PEG to provide a space for surface functionalization. The composite NPs were successful in the shuttling the drug efficiently into the treated cells while concurrently bioimaging it.

Chapter 4 describes the development of a single unit theranostic. Here MTX (methotrexate), a commercial clinical drug is used as a template to synthesise gold nanoclusters. These single unit theranostics were extremely stable both in PBS and blood serum. They were brightly fluorescent, photostable and were efficiently taken by the cells. They inflicted highly augmented cytotoxicity on the host cells, also enabling the concurrent bioimaging the host cells.

Chapter 5 entails the formation of a folic acid conjugated chitosan NP on which these MTX NCs were loaded. The purpose of the chapter is to study the feasibility of replacing the free drug with MTX NCs which have higher cytotoxicity and additional fluorescent properties in a drug delivery vehicle. The NPs were efficiently taken up by the cells and bioimaged it. The host cells also displayed an almost two-fold reduction in IC_{50} value of the drug when subjected to NPs in MTX NCs form. This augurs well for the further development of such single unit theranostics.

Chapter 6 provides a comprehensive summary of the thesis and provides insight into the potential prospects of the thesis work.

Keywords: Nanoparticles, Gold Nanocluster, pDNA, dGTP, MTX, Composite NPs, Theranostics.

List of Abbreviations

AO	Acridine Orange	**G NCs**	dGTP templated Gold Nanoclusters
Au NC	Gold Nanocluster	**MALDI-**	Matrix Assisted Laser Desorption/Ionization
Cis	Cisplatin	**MTT**	3-(4,5-dimethylthiazol-2-yl)-2,5-diphenyltetrazolium bromide
DNA	Deoxyribonucleic acid	**MTX**	Methotrexate
DCFH-DA	Dichloro-dihydro-fluorescein diacetate	**NCs**	Nanoclusters
CTX	Chitosan	**NPs**	Nanoparticles
HeLa	Human Cervical Cancer Cell	**pDNA**	Plasmid DNA
E.coli	Escherichia coli	**QY**	Quantum Yield
EDC	1-Ethyl-3-(3-dimethylaminopropyl) carbodiimide	**ROS**	Reactive Oxygen Species
FA	Folic Acid	**RNase**	Ribonuclease

FACS	Fluorescence Activated Cells Sorter	**SEM**	Scanning Electron Microscope
FESEM	Field-Emission Scanning Electron Microscope	**TEM**	Transmission Electron Microscope
FETEM	Field-Emission Transmission Electron Microscope	**TPP**	Sodium Tri-Polyphosphate
FTIR	Fourier Transformed Infra-Red	**XPS**	X-ray photoelectron spectroscopy

CHAPTER 1

Introduction and Review of Literature

Introduction and Review of Literature

1.1 Introduction

"There is a plenty of room at the bottom"[1] with these words Feynman set the stage for the first recorded tryst of the world with the intriguing concept of manipulation at an atomic and molecular level only to be baptized as "**Nanotechnology"** 15 years later. In 1974 at a conference at Tokyo University of science Japanese scientist Norio Taniguchi first coined the term "Nanotechnology" that he used to describe "processing of, separation, consolidation, and deformation of materials by one atom or one molecule". Coming to late 1990, still obscure to masses, the term first gained wide recognition with Prof. K. Eric Drexler using the term unaware of its prior mention in his 1986 book "Engines of Creation: The Coming Era of Nanotechnology." In this work, he envisaged a nanoscale assembler capable of self-replicating as well as replicating other structures of arbitrary complexity[2]. At that point of time, he seemed futurist, and his prophecies were little substantiated with traditional experimental work. Such were his ideas, that it led famous novelist Michael Crichton to produce a bestselling book, **Prey**, a techno-thriller in which he wrote about the Drexler's nanobots. Establishment of research protocols and policy decision resulted in the technological development necessary to help understand several development of nanosciences and nanotechnology [3].

The development of Scanning Tunneling Microscope (STM) and Atomic Force Microscope, both at IBM Research Zurich in a successive manner offered the first major breakthrough in the technological advancement. First, in 1981 Gerd Binnig and Heinrich Rohrer reported the development of STM[4,5], which in turn acted as a precursor for the development of AFM initially developed by Gred Binnig in 1982 and later experimentally implemented by him along with Calvin F. Quate and Christoph Gerber

in 1986, which revolutionized the field[3]. Now it was possible for the scientific community not only to image a material at nanoscale but also manipulate at nanoscale level. Since then, the field has witnessed an exponential growth and percolated into almost every aspect of applied science spanning from computers to medicines.

Since its inception nanotechnology has promised a golden future in drug delivery. Speculations were initially fueled from the existing knowledge of antibacterial properties of silver, laying the basic foundation for study of its antimicrobial properties at a nanoscale range. However, modern drug delivery systems gained momentum with the introduction of liposomes in mid-1960s and with polymer-drug conjugates in the mid to late 1970s, the concept of nanoengineered drug delivery systems was established[6]. They offered several advantages over traditional free drug delivery systems like better transport, lesser systemic cytotoxicity, to name among many.[7] Since then the quest for designing better drug delivery systems had begun. Starting from the polymeric nanoparticles to metallic nanoparticles thrust has been given on all areas. However, the field remained significantly tilted towards the organic nanoparticles in its initial phase. This is largely attributable to the better understanding of ***in vivo*** metabolism and toxicity of organic materials. In addition, many organic nanoparticles such as liposomes, micelles, and dendrimers can carry drug molecules at a more substantial payload ratio than their inorganic counterparts. But with the advent of fluorescent metal nanoclusters, they readily began to be employed for cellular imaging. Nanoclusters of gold and copper are already being reported to have been used for cellular imaging and being the component of drug delivery system[8,9].

1.2 Cancer: An old relic or a humanmade omen

Cancer is a disease, characterized by uncontrolled cellular growth in a particular

part of the body. The normal cells in the body grow, differentiate and die according to signals relayed to them by the body, but in cancer, cells defy this normal cellular checks and balances and resort to continuous growth and division resulting in more abnormal cells[10]. The disease primarily is caused by a damaged cellular DNA whose products viz RNA and proteins are involved in the cellular checks and balances. The cause of this detrimental DNA damage can range from various external (pesticides, smoke, UV rays etc.) or internal (DNA replication error, DNA repair error). These transformed cells either stay at the point of its original development to form a tumor or they dissociate from its original site and enter the circulatory system (mainly blood circulation or lymphatic circulation) and migrate to some other sites in the body. The former condition is called a benign tumor and is not that much detrimental to body. In contrast, the later, called malignant tumor, has a more aggressive growth than the former and is much detrimental as it spreads the disease to other parts of the body[4] making it difficult to diagonose and hence, treat.

Traditionally, cancer has been treated with surgery (removing tumors) or by chemotherapy where drugs like cisplatin, doxorubicin (DOX), methotrexate (MTX) and cabazitaxel (CTX) are administrated into the body[4]. These drugs disrupt the essential molecular activities of the cells and eventually lead them to death. However, conventional therapy has some severe limitations, most prominent among them is systemic cytotoxicity[6]. Consequently, different therapeutic approaches have been developed in due course of time to overcome the limitations of the conventional therapy. For instance, instead of simply administrating the free drug, drug delivery vehicles have been developed, which later on were adorned with many additional features each aimed to reduce the systemic cytotoxicity and increase the efficacy[6,11–17]. Among the many recently developed strategies, theranostics are particularly intriguing

owing to many edges over their conventional as well as their contemporary counterparts.

1.3 Theranostics

Theranostics is a relatively new concept, with the term being coined by Funkhouser in 2002 [18]. It refers to the encapsulation of therapeutic and diagnostic functionalities into a single system. As for cancer or any other disease, diagnosis is a vital step in its therapy. So before starting a treatment, it is a perquisite to understand the phenotype and microenvironment of the cancer tissue, for which we need a diagnostic moiety. Administrating the diagnostic moiety and therapeutic moiety in separate doses can led to differential biodistribution and delivery of the therapeutic also cannot be confirmed. This complexity served as an incentive to integrate the therapeutic and diagnostic moiety into a single delivery "package" and thus developed the idea of a theranostic (**Figure 1.1**). A theranostic is a system which has both diagnostic and therapeutic modalities. This progress was in the pursuit of gaining the competency to concurrently deliver into and monitor the target tissue through imaging. It also generates the possibility of understanding the delivery kinetics and enhancing the shuttling efficiency and is an important step in reaching the utopian dream of continuous tuning of the therapy, which hitherto seemed implausible.

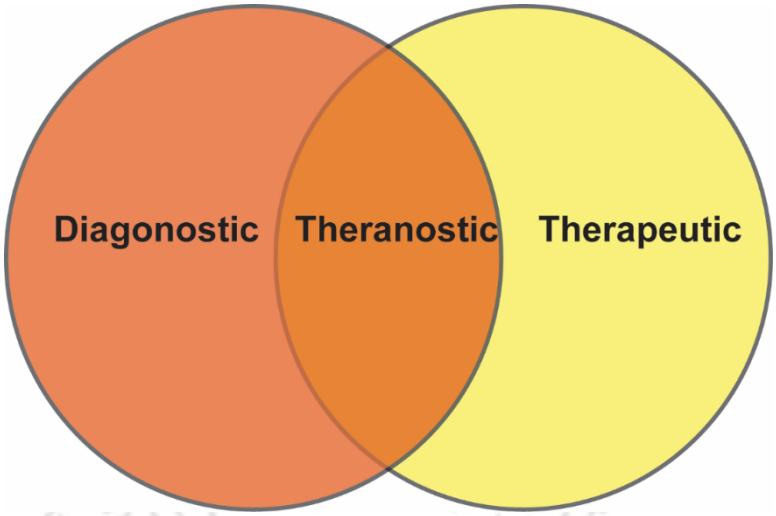

Figure 1.1: *A theranostic is a system having both diagnostic and therapeutic modalities.*

Having a theranostic in nanoscale range has several advantages. The size regime itself facilitates longer circulation time as they are not readily cleared from the circulation by the kidney. The nanoparticles bring the possibility of shuttling the payload in a very precise manner to the intended site, simultaneously reducing the random spillage and systemic cytotoxicity that ensues with their conventional counterparts. Less spillage during the transport also translates into higher quanta of the therapeutic reaching the intended site resulting into augmented cytotoxicity[6]. Additionally, these platforms come with the immense possibilities of requirement dependent functionalization and custom tailoring of the delivery system. For instance, simple surface functionalization with PEG results in a longer circulation time[19] or surface functionalization with targeting moieties leads to more payload accumulation in the destined site. Surface functionalization with stimuli (pH, temperature, redox and enzymatic activity) engenders very stringent payload release conditions. This translates into augmented transport efficiency as the payload is released only when the requisite stimulus is present hence, reducing the spillage at nonspecific sites. Tailoring a

multicomponent nanotheranostic is another step towards realizing the goal of personalized medicine. For instance, theranostic nanoparticles with multimodal imaging capabilities can facilitate superior images at multiple length scales or treatment stages, enabling disease diagnosis with enhanced precision and therefore more calibrated therapy[20] rather a generic one thus avoiding one shoe fits all approach.

1.3.1 Immune Nanotheranostics

This genus of nanotheranostics involves immune system to counter cancer. Unlike the conventional drug based nanotheranostics, here, the final targets of the two components (diagnostic and therapeutic) are separate[21]. While the diagnostic units remain primarily concerned with the tumour diagnosis and therapy monitoring, the therapeutic unit primary targets peripheral lymphocytes, tumour-infiltrating lymphocytes or tumour cells themselves. These systems either deliver some boost to the immune cells or an engineered immune cells (particularly the T cells) to instigate an immune response against the cancer cells. For generating the needed immune response, a plethora of payloads are established. Biomolecules like cytokines, interleukins (IL 2 in particular), interferons, angioinhibitors and various antigens can be produced *in vitro* and then can be transported using nanocarriers. Neoantigens, a caner specific antigen arising due to somatic mutation, presents an advantage for development of nanotheranostics. These antigens signature being unique to each patient, raising the possibility of personalized medicine. However, the frequency of neoantigens specific T cells being low so exogenous stimulus is required. This requirement can be easily gratified with nanovaccines. Nanovacines can also carry a mRNA, coding the antigens as present technologies take a longer period of production of neoantigens. This antigen encoding mRNA can then be delivered to the APC cells which will lead to enhanced

level of naturally scanty neoantigens. In a study, the feasibility of this concept was demonstrated, where liposome was used to deliver this mRNA to lymphoid dendritic cells in the spleen and resulted in augmented T cell response in Humans and mice.

1.3.2 Nanocluster based Theranostics

Nanoclusters are essentially cluster or aggregation of atoms with the constituent number typically ranging from 2-100 atoms and quintessentially particle size falling in < 2 nm regime. Aptly called the missing link between the isolated metal atoms and plasmonic metal nanoparticles, it observes molecule like behavior owing to its size regime. At a size regime comparable to the fermi wavelength of an electron (i.e., de Broglie's wavelength of an electron at the fermi energy, ~0.5 nm for gold and silver) the electronic structure of metals breaks away from its bulk counterpart and is manifested as the discretization of energy levels into separate against the continuous energy levels of later. This leads to the generation of sundry novel properties spanning over electrical, chemical and optical genres. These *de novo* properties are best explained by the jellium model; a simple Quantum mechanical theory which has its genesis in nuclear physics[22]. The background is drawn from the fact that the valence shell electrons experience a lesser amount of attraction from the positively charged core due both to the distance from the core (columbic attraction) and electron screening effect (electron-electron repulsion), engendering a loosely bound valence electron. These valence electrons are responsible for the observed electrical properties of bulk metals. Jellium model assumes the cluster as a spherical structure with positively charged core and jellium orbitals (analogous to electronic orbitals) around it filled with the valence electrons of the constituent atoms and essentially follows the Pauli's exclusion principle. Similar to its plasmonic counterpart (nanoparticles), the free

electrons in the clusters also feel the linear restoring force modeled by Hooke's law, in a manner that the quantized shells can be described by a simple 3D harmonic oscillator. As jellium model considers a spherical potential which acts from the center of the cluster, the solution for the Schrödinger equation is very much similar to single atoms.

The jellium orbitals and the atomic orbitals follow the same annotation although, they have different magic numbers. This arises due to the surface potential differences between the atomic and jellium orbitals. While the electrons in an atomic system are in a Coulomb (r^{-1}) potential, electrons in a metal cluster are in an approximately harmonic (r^2) potential. This translates into independence of the angular momentum quantum number from the principal quantum number. While the magic numbers in the nth shell of atoms are dictated as,

$$N^0 = \frac{2}{3} n \left(n + \frac{1}{2}\right), (n+1)$$

Where N^0 =2, 10, 28 translates into 1s, 2s, 2p, 3s, 3p, 3d…electronic shells.

The magic numbers for the nth shell of cluster are dictated as:

$$N^0 = \frac{1}{3}(n+1), (n+2), (n+3)$$

Where N^0 = 2, 8, 20, 40 translates into 1s, 1p, 1d, 2s, 1f, 2p …electronic shells.

Also the principal quantum number in jellium model (n) is related to the principal quantum number of atomic orbitals (n_{at}) as,

$$n = n_{at} - l,$$

Where l = angular quantum number.

Magic numbers arise due to complete filling of the jellium levels. However, the exact filling order (energy order) depends upon radial form of the assumed effective jellium potential. There are three different forms of radial jellium potential (**Figure 1.2, 3**).

1.3.2.1 The 3-D harmonic potential

This considers the cluster as a spherical structure and the mathematical expression for the potential energy function,

$$U\,(R) = -\kappa(R - R_0)^2,$$

Where R_0 is the cluster radius

Here all the orbitals having same $(2l + 1)$ value are degenerate (have same energy), as a result of which a new quantum number $(v = 2l + 1 - 2)$ can used to express the orbital energies. Here the degeneracy can be calculated as, $\frac{1}{2}(v + 1)(v + 2)$ and it generates the magic numbers as N^0=2, 8, 20, 40, 70, etc. While this justifies the stability of experimentally found 8, 20 and 40 electrons, it fails to explain the 58 electron clusters.

1.3.2.2 The 3-D square well potential

Here the potential is constant throughout the sphere and infinite at cluster radius (R_0), which can be mathematically expressed as,

$$U(R) = U_0, \qquad R < R_0$$

$$U(R) = \infty, \qquad R \geq R_0$$

The ordering of the jellium orbitals is 1s<1p<1d<2s<1f<2p<1g..., so on which translates into magic numbers (N^0) been =2, 8, 18, 20, 34, 40 and 58 (etc.) electrons. It does explain the stability of 58 electron cluster.

1.3.2.3 The Woods-Saxon potential

This is the most widely accepted radial potential and is an intermediate between the 3-D harmonic potential and 3-D square well potential and is represented by a largely square well with rounded sides. The potential here is expressed mathematically as,

$$U(R) = \frac{-U_0}{\exp\left[\frac{R-R_0}{\sigma}\right] + 1}$$

Where $U_0 = E_F + W$. Here E_F and W are the Fermi energy and the work-function of the bulk metal respectively.

$R_0 = R_{ws}N^{\frac{1}{3}}$, here R_{ws} = Wigner-Seitz radius and σ is a constant scaling distance of 1.5 bohr and R_0 is the effective radius of the cluster sphere.

Here, the general order of orbitals energies is an intermediate between the two aforementioned potentials with jellium level ordering as, 1s<1p< 1d<2s<1f<2p<1g and magic number as, N^0=2, 8, 18, 20, 34, 40, 58 etc. are the same as for the 3-D square well potential with the first difference in orbital ordering occurring above the 2d orbital (i.e. for more than 68 electrons) between them [23,24].

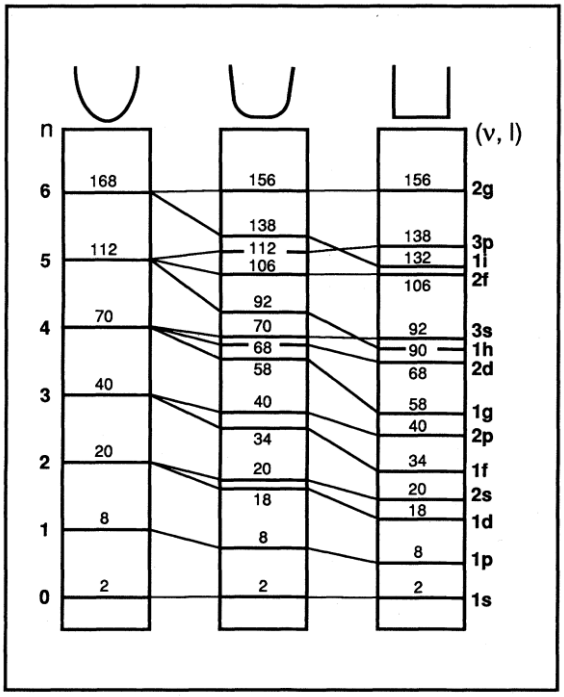

***Figure 1.2**: Energy-level occupations for spherical three dimensional, harmonic, intermediate, and square-well potentials. (After Mayer and Jensen, 1955. From the reference 24.)*

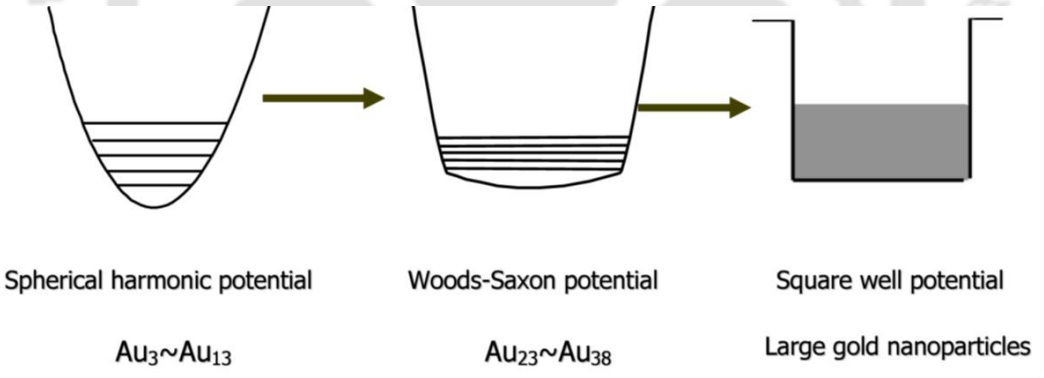

***Figure 1.3**: Schematic of size-dependent surface potentials of gold clusters on different size scales. For the smallest gold clusters (Au3 to Au13), cluster emission energies can be well fit with the energy scaling law $E_{fermi}/N^{1/3}$, where N is the number of atoms in each cluster, indicating that electronic structure transitions of these small gold clusters are well-described by a spherical harmonic potential. With increasing size, small an-harmonicities distort the potential well, which at larger sizes gradually distorts into a Woods-Saxon potential surface, and eventually becomes a square well potential characteristic of electrons in large metal nanoparticles. (From the reference 24. Copyright by American Physical Society 2004.)*

Among the many generated *de novo* properties, the optical properties of the nanoclusters find a special niche in the field of theranostics. When the size of the clusters commensurate with the fermi wavelength of an electron, the quasi continuous band structure of the metals become distinct due to discretization of its energy levels and the free electrons experience a strong quantum confinement in thus generated energy levels. This leads to generation of molecule-like properties (strong fluorescence in the region over near U.V. to far IR). The energy level spacing (E_δ) is of particular importance in determining the fluorescence behavior of the clusters.

$$E_\delta = E_{Fermi}/N^{1/3}$$

This equation underlines the inverse dependence of the emitted wavelength on the constituent number of atoms in cluster (**Figure 1.4**). Furthermore, the free electron density of the clusters also effects the electronic transitions. Therefore surface phenomenon like metal to ligand charge transfers(LMCT) also influences the excitation and emission properties of the cluster without altering the core metallic structure of the clusters[24].

Owing to its fluorescent properties nanoclusters, gold nanoclusters (has many advantages over other counterparts[25]) in particular have been intensely researched for their use in various theranostic platforms[8,20,26,27,27–32].

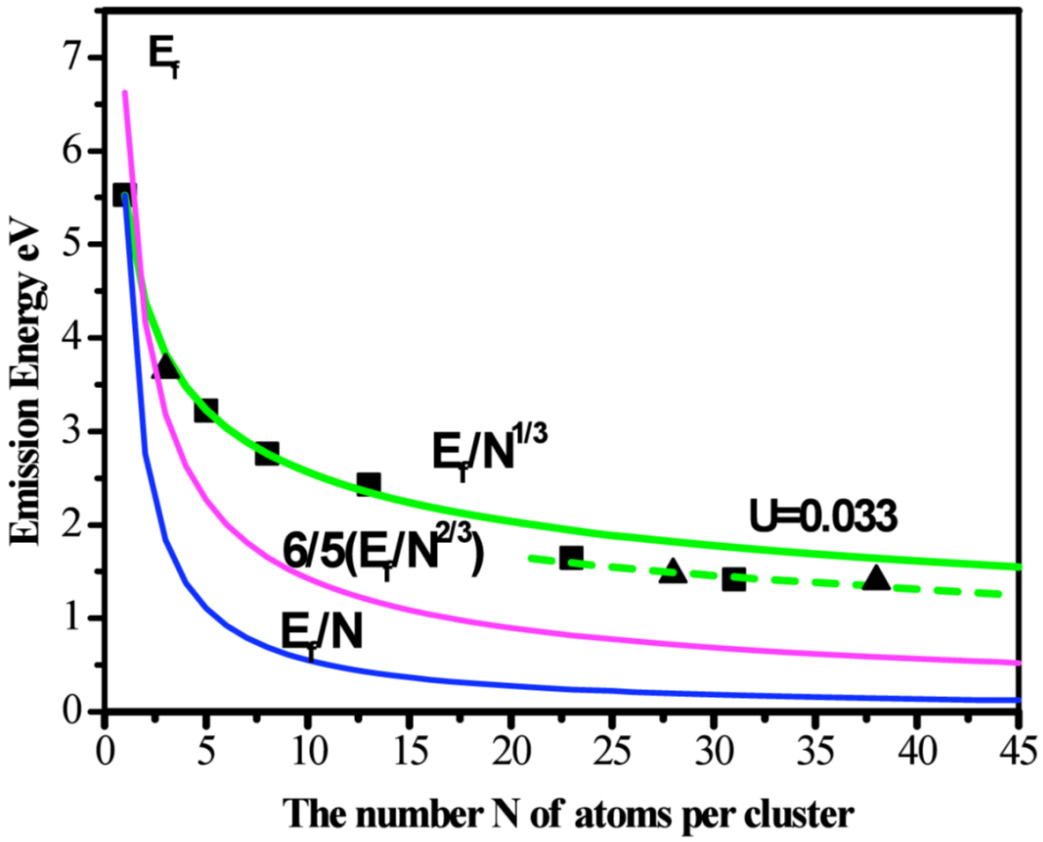

Figure 1.4: *Correlation of the number of atoms, N, per cluster with emission energy. Emission energy decreases with increasing number of atoms. The correlation of emission energy with N is quantitatively fit with $E_{fermi}/N^{1/3}$, as predicted by the jellium model. When N is equal to, the energy of valence electron is equal to Fermi energy because the valence electron is at the HOMO level. Emission energies of Au_{23} and Au_{31} exhibit slight deviations from the $E_{fermi}/N^{1/3}$ scaling. Consistent with the narrow excitation and emission spectra, the potential confining the free electrons flattens slightly for Au_{23} and Au_{31}, with an-harmonicity parameter U=0.033. The experimental values for the emission energies of Au_3, Au_{28} and Au_{38} are 3.66, 1.55, and 1.44 eV respectively (represented by ▲), which are all consistent with the observed scaling relations. Kubo's predicted model E_f/N and the square potential box model $6/5E_f/N^{2/3}$ are also shown in the figure. Obviously these models can not accurately fit the emission energy scalings of the gold clusters. (From the reference 24. Copyright by American Physical Society 2004.)*

1.4 Targeting strategies

An important aspect of any efficient theranostic has to be seen through its ability to reach the target site and discharge its payload at the desired site with

minimum transport spillage. For this, different modes of targeting strategies have been developed based on the tumor architecture and its microenvironment which are discussed below.

1.4.1 Passive targeting

The passive targeting heavily relies on the tumor architecture, which differs considerably from the normal vascular architecture[33]. Normal blood flow has a sequence where the blood flows successively through the arteries, arterioles, capillaries, venules and finally into veins which then return to the heart. The exchange of nutrients and other molecules largely occurs through the thin walled capillaries. In normal tissues, these capillaries have an architecture in which the capillaries are lined with tightly packed endothelium cells, which in turn are attached to pericytes and the whole system is further enveloped in a thin layer of basal membrane.[33] In contrast to normal vasculature the tumor vasculature has a non-continuous endothelial lining which lead to formation of larger pores (0.1−3 μm in diameter) along the vasculature compared to normal vasculature pores (5–10nm)[34]. Due to this reason, tumor vasculature has a higher permeability and hydraulic conductivity. Additionally, the pericytes and basal membrane are also loosely attached to the endothelial cells. With this reduced coverage of pericytes, it eventually leads to enhanced trans-endothelial permeability. The situation is further compounded by the poor lymphatic drainage system at the tumor site[34]. This eventually engenders high accumulation of particles of certain size regime at the tumor site due to more influx (due to higher permeability and hydrologic conductivity) and less efflux (impaired drainage system) and is called Enhanced Permeation and Retention effect (EPR)[6]. It was first reported by Matsumura and Maeda that nanoparticles have a higher accumulation rate at tumor site[35].

1.4.2 Active targeting

EPR, although an interesting phenomenon that increases the intratumoral accumulation of the nanoparticles, fails however, to yield desirable cellular uptake of the nanocarriers owing to many problems[34]. This in part can be overcome by using active targeting. Active targeting refers to functionalization of the nanocarrier with specific targeting moieties that are specific for the target cancer cells. Cancer cells in general overexpress certain ligand receptors (folic acid receptors) or have receptors that are exclusively expressed on certain type of cancer cells. These receptors facilitate receptor mediated endocytosis that results in specific uptake of the payload in the desired cells, while greatly reducing the nonspecific uptake by other cells simultaneously. However, it must be borne in mind that many studies suggest, intratumoral accumulation largely remained similar to that obtained from their untargeted counterpart, and the overall distribution profile of the targeted nanoparticles remain similar to their untargeted counterparts[36,37]. But it dramatically increases the delivery of the payloads into the cells[38]. This essentially translates into higher tumoral cytotoxicity but lower systemic cytotoxicity. The targeting moieties can include monoclonal antibodies (such as trastuzumab), specific peptides, aptamers, small molecules (e.g. folate)[39]. This mode of tumor targeting is rapidly gaining interest and already many of them are undergoing clinical trials. For instance, BIND-014, a polymeric nanoparticle carrying docetaxel with controlled-release property that entered phase I clinical investigation[40].

1.4.3 Stimuli responsive Nanoparticles

Nonetheless, both EPR based and surface ligand based nanocarriers have shown exciting results in preclinical animal models. Their clinical translation rates are

however, yet to take off. This, in part is because of certain inherent complexities with the EPR (abnormal tumor vasculature, high interstitial fluid and solid stress from abnormal stromal matrix) and targeted nanovehicles (due to stochastic nature of ligand-receptor interaction and lack of control over the release profile). Even the Fickian diffusion (determines the leakage of the drug from the carrier) is also tissue or cell specific, leaving the specter of systemic cytotoxicity minimized but not that of desired level[16]. Reduction in cargo spillage requires the nanocarriers to discharge their payload stringently only when they encounter specific stimuli. Such responsive nanocarriers can be designed with biocompatible nanomaterials, which can recognize microenvironments around them and then undergoe a specific conformational change (e.g. induced by specific protonation or hydrolytic cleavage) on encountering the stimuli. The first stimuli responsive nanocarrier was reported way back in 1978, a hypothermia triggered local drug release[41]. Since then the field has caught the fascination of the scientific community particularly with the concurrent developments in material science.

The provided stimuli can be exogenous (can be applied from outside) such as magnetic field[42], temperature changes[43,44], electric field, ultrasound etc. or the it can be an endogenous one. Endogenous stimuli are already there in the microenvironment of the nanocarriers. It includes pH variations associated with normal and cancerous tissues[45], high concentration of certain solutes like glutathione[46], specific or augmented enzymatic[47] activity in the microenvironment. The endogenous stimuli can also work even after the uptake of the nanocarrier inside the cell[48]. For instance, the pH change associated with endosomal pathway can trigger release of payload from a pH responsive nanocarrier[49].

1.5 Objectives of the thesis

- DNA based gold nanoclusters have been already reported in the literature. DNA origami, DNA nanocages have been reported as drug delivery vehicles. However, the design of the nanovehicles is a cumbersome process, which consumes a mammoth amount of technical expertise and costs a fortune. Essentially these nanocarriers carries payloads, which also includes various anticancer drugs. Now, many anticancer drugs like cisplatin act by intercalating in the DNA structure, subsequently hindering the DNA repair and replication processes. These intercalations are potential opportunities to be exploited. The key idea behind this objective was to develop a natural unaltered DNA based nanocarrier, which can bind with a DNA intercalating drug only to deliver the drug into the cancer cells. For this purpose, we have synthesized fluorescent gold nanoclusters on a plasmid DNA and conjugated the same with cisplatin to form composite nanoparticles. The NPs have theranostic prospective as they contain both requisite moieties, a diagnostic moiety due to presence of fluorescent gold nanoclusters as well as the therapeutic moiety due to cisplatin.
- Synthesizing gold nanoclusters on small molecules always poses a challenge. Owing to high surface energy of nanoclusters it is very difficult to stabilize it on a small template. Although considerable progress has been made in this field but it still has to grow a lot. The aim of this objective was to synthesize gold nanoclusters on small molecules and transform them into theranostic units. Now in the previous study we have already established the feasibility of the simple plasmid DNA templated Au NCs carrying cisplatin. Cisplatin is known to primarily bind with purines mostly forming guanine addicts. The objective of this study was to develop Au NCs on a dGTP (deoxy guanosine triphosphate, a

purine) template and then form a theranostic composite NP by interacting it with cisplatin with PEG coating.

- Up to this stage, we have largely remained invested into developing theranostic composite NPs that can deliver a drug payload, but it always intrigued us if the drug molecule could itself be transformed into a single molecule theranostic. The aim of the present study was to synthesize gold nanoclusters on a commercial anti-cancer drug. But the crux point was to develop this theranostic in a way that the templated drug should have similar cytotoxicity or higher.
- To check the amenability of as-synthesized single unit theranostics on drug delivery platforms.

1.6 Outline of the thesis

- **Chapter 1** includes a brief introduction of nanotechnology and description of cancer. The chapter reviews various cancer therapeutics in a comparative manner. The chapter also provides a compact introduction to nanoclusters and its involvement in various theranostic platforms.
- **Chapter 2** describes the development of a plasmid DNA templated Au NCs based composite NPs. The nanoparticles were formed by exploiting the DNA intercalating property of cisplatin and subsequent induced bending of the parent DNA molecule. The chapter provides a detailed physical characterization of the composite NPs using various analytical techniques. The chapter includes the stability study and release profile of the composite NPs. The bioimaging potential of the composite NPs was also evaluated using confocal microscopy. The cytotoxicity profile was measured by cell viability assay and the

mechanism of cellular death was further evaluated with flow cytometry assisted studies.

- **Chapter 3** deals with the synthesis and subsequent physical characterization of the dGTP templated gold nanoclusters. It entails the impressive physical characteristics of the dGTP and formation of composite NPs by exploiting the interaction with cisplatin and dGTP. The composite NPs were further coated with the PEG to provide the theranostic a stealth nature and a sustained release profile. The composite NPs successfully delivered the payload with concurrent cellular imaging of the host cells. The chapter also describes various flow cytometry based studies, which elucidate the apoptotic nature of the induced cellular death.
- **Chapter 4** describes the development of a single unit theranostic. The chapter entails the formation of methotrexate templated ultrasmall gold nanoclusters, which act as theranostic. The MTX NCs were thoroughly characterized with various analytical instruments to assess its diagnostic potential and stability in both serum (*in vivo*) and PBS (carrying medium). The chapter also includes the confocal studies performed to evaluate bioimaging potential of the theranostic. The MTX NCs were subjected to HeLa cells to assess its cytotoxicity in comparison with the parent drug. Various flow cytometry based studies were performed to identify the mode of cellular death.
- **Chapter 5** entails the study performed to assess the amenability of the aforementioned single unit theranostics (MTX NCs) to be delivered using an existing drug delivery platform. Chitosan-folic acid nanoparticles (NPs) were synthesized as drug delivery vehicles to shuttle these MTX NCs into cancer cells (HeLa). The NPs successfully delivered the payload with concurrent

cellular imaging of the host cells. The NPs inflicted a higher cytotoxicity on the host cells than the MTX NCs themselves owing to the better delivery of the MTX NCs than free transport of the MTX NCs.

- **Chapter 6** provides a summary of the present thesis and future prospects of the work.

1.7 References

(1) Editorial. Editorial " Plenty of Room " Revisited. *Nat. Nanotechnol.*, *4* (December), 2009.

(2) Drexler, K. E. *Engines of Creation*; Fourth Estate, 1996.

(3) Tolochko, N. K. HISTORY OF NANOTECHNOLOGY.

(4) Binnig, G.; Rohrer, H.; Gerber, C.; Weibel, E.; Binnig, G.; Rohrer, H.; Gerber, C.; Weibel, E. Tunneling through a Controllable Vacuum Gap Tunneling through a Controllable Vacuum Gap. *Appl. Phys. Lett.* **1982**, *40*, 178–180.

(5) Binnig, G.; Rohrer, H.; Gerber, C.; Weibel, E. Surface Studies by Scanning Tunneling Microscopy. *Phys. Rev. Lett.* **1982**, *49* (1), 57–61.

(6) Wang, A. Z.; Langer, R.; Farokhzad, O. C. Nanoparticle Delivery of Cancer Drugs. *Annu. Rev. Med.* **2012**, *63*, 185–198.

(7) Allen, T. M.; Cullis, P. R. Drug Delivery Systems : Entering the Mainstream. **2004**, *303* (March), 1818–1823.

(8) Qu, X.; Li, Y.; Li, L.; Wang, Y.; Liang, J.; Liang, J. Fluorescent Gold Nanoclusters: Synthesis and Recent Biological Application. *J. Nanomater.* **2015**,

2015.

(9) Wang, C.; Wang, C.; Xu, L.; Cheng, H.; Lin, Q.; Zhang, C.; Wang, C. X.; Zhang, D.; Xu, L.; Jiang, Y. N.; et al. Protein-Directed Synthesis of pH-Responsive Red Fluorescent Copper Nanoclusters and Their Applications in Cellular Imaging and Catalysis. *Nanoscale* **2014**, *6* (3), 1775–1781.

(10) Lodish, H.; Berk, A.; Matsudaira, P.; Kaiser, C. A.; Krieger, M.; Scott, M. P.; Zipursky, L.; Darnell, J. *Molecular Cell Biology*, 6th ed.; W. H. Freeman, **2008**.

(11) Timko, B. P.; Whitehead, K.; Gao, W.; Kohane, D. S.; Farokhzad, O.; Anderson, D.; Langer, R. Advances in Drug Delivery. **2011**, No. February, 1–20.

(12) Yoo, J.-W.; Irvine, D. J.; Discher, D. E.; Mitragotri, S. Bio-Inspired, Bioengineered and Biomimetic Drug Delivery Carriers. *Nat. Rev. Drug Discov.* **2011**, *10* (7), 521–535.

(13) Felice, B.; Prabhakaran, M. P.; Rodríguez, A. P.; Ramakrishna, S. Drug Delivery Vehicles on a Nano-Engineering Perspective. *Mater. Sci. Eng. C* **2014**, *41*, 178–195.

(14) La, T. H.; Nguyen, T. T. T.; Pham, V. P.; Nguyen, T. M. H.; Le, Q. H. Using DNA Nanotechnology to Produce a Drug Delivery System. *Adv. Nat. Sci. Nanosci. Nanotechnol.* **2013**, *4* (1), 15002.

(15) Li, J.; Fan, C.; Pei, H.; Shi, J.; Huang, Q. Smart Drug Delivery Nanocarriers with Self-Assembled DNA Nanostructures. *Adv. Mater.* **2013**, *25* (32), 4386–4396.

(16) Mura, S.; Nicolas, J.; Couvreur, P. Stimuli-Responsive Nanocarriers for Drug Delivery. *Nat. Mater.* **2013**, *12* (11), 991–1003.

(17) Torchilin, V. P. Multifunctional, Stimuli-Sensitive Nanoparticulate Systems for Drug Delivery. *Nat. Rev. Drug Discov.* **2014**, *13* (11), 813–827.

(18) Kelkar, S. S.; Reineke, T. M. Theranostics: Combining Imaging and Therapy. *Bioconjug. Chem.* **2011**, *22* (10), 1879–1903.

(19) Veronese, F. M.; Pasut, G. PEGylation, Successful Approach to Drug Delivery. *Drug Discov. Today* **2005**, *10* (21), 1451–1458.

(20) Bao, G.; Mitragotri, S.; Tong, S. Multifunctional Nanoparticles for Drug Delivery and Molecular Imaging. *Annu. Rev. Biomed. Eng.* **2013**, *15*, 253–282.

(21) Chen, H.; Zhang, W.; Zhu, G.; Xie, J.; Chen, X. Rethinking Cancer Nanotheranostics. *Nat. Rev. Mater.* **2017**, *2* (7), 17024.

(22) Heer, W. A. De. The Physics of Simple Metal Clusters : Experimental Aspects and Simple Models. **1993**, *65* (3).

(23) Johnston, R. L. *Atomic and Molecular Clusters*; 2002.

(24) Zheng, J.; Nicovich, P. R.; Dickson, R. M. Highly Fluorescent Noble Metal Quantum Dots. *Annu. Rev. Phys. Chem.* **2008**, *22* (5), 4109.

(25) Venkatesh, V.; Shukla, A.; Sivakumar, S.; Verma, S. Purine-Stabilized Green Fluorescent Gold Nanoclusters for Cell Nuclei Imaging Applications. *ACS Appl. Mater. Interfaces* **2014**, *6* (3), 2185–2191.

(26) Lei, Y.; Tang, L.; Xie, Y.; Xianyu, Y.; Zhang, L.; Wang, P.; Hamada, Y.; Jiang, K.; Zheng, W.; Jiang, X. Gold Nanoclusters-Assisted Delivery of NGF siRNA for Effective Treatment of Pancreatic Cancer. *Nat. Commun.* **2017**, *8*, 15130.

(27) Shang, L.; Dörlich, R. M.; Brandholt, S.; Schneider, R.; Trouillet, V.; Bruns, M.; Gerthsen, D.; Nienhaus, G. U.; Joo, C.; Balci, H.; et al. Facile Preparation of Water-Soluble Fluorescent Gold Nanoclusters for Cellular Imaging Applications. *Nanoscale* **2011**, *3* (5), 2009.

(28) Chen, D.; Li, B.; Cai, S.; Wang, P.; Peng, S.; Sheng, Y.; He, Y.; Gu, Y.; Chen, H. Dual Targeting Luminescent Gold Nanoclusters for Tumor Imaging and Deep Tissue Therapy. *Biomaterials* **2016**, *100*, 1–16.

(29) Zhou, F.; Feng, B.; Yu, H.; Wang, D.; Wang, T.; Liu, J.; Meng, Q.; Wang, S.; Zhang, P.; Zhang, Z.; et al. Cisplatin Prodrug-Conjugated Gold Nanocluster for Fluorescence Imaging and Targeted Therapy of the Breast Cancer. *Theranostics* **2016**, *6* (5), 679–687.

(30) Govindaraju, S.; Ankireddy, S. R.; Viswanath, B.; Kim, J.; Yun, K. Fluorescent Gold Nanoclusters for Selective Detection of Dopamine in Cerebrospinal Fluid. *Sci. Rep.* **2017**, *7*, 40298.

(31) Yahia-Ammar, A.; Sierra, D.; Mérola, F.; Hildebrandt, N.; Le Guével, X. Self-Assembled Gold Nanoclusters for Bright Fluorescence Imaging and Enhanced Drug Delivery. *ACS Nano* **2016**, acsnano.5b07596.

(32) Dutta, A.; Dutta, D.; Sanpui, P.; Chattopadhyay, A. Biomimetically Crystallized Protease Resistant Zinc Phosphate Decorated with Gold Atomic Clusters for Bioimaging. *Chem. Commun.* **2017**, *53* (7), 1277–1280.

(33) Nagy, J. A.; Chang, S. H.; Dvorak, A. M.; Dvorak, H. F. Why Are Tumour Blood Vessels Abnormal and Why Is It Important to Know? *Br. J. Cancer* **2009**, *100* (6), 865–869.

(34) Danquah, M. K.; Zhang, X. A.; Mahato, R. I. Extravasation of Polymeric Nanomedicines across Tumor Vasculature. *Adv. Drug Deliv. Rev.* **2011**, *63* (8), 623–639.

(35) Matsumura, Y.; Maeda, H. A New Concept for Macromolecular Therapeutics in Cnacer Chemotherapy: Mechanism of Tumoritropic Accumulatio of Proteins and the Antitumor Agents Smancs. *Cancer Res.* **1986**, *46* (12 Pt 1), 6387–6392.

(36) Kirpotin, D. B.; Drummond, D. C.; Shao, Y.; Shalaby, M. R.; Hong, K.; Nielsen, U. B.; Marks, J. D.; Benz, C. C.; Park, J. W. Antibody Targeting of Long-Circulating Lipidic Nanoparticles Does Not Increase Tumor Localization but Does Increase Internalization in Animal Models. *Cancer Res.* **2006**, *66* (13), 6732–6740.

(37) Schmidt, M. M.; Wittrup, K. D. A Modeling Analysis of the Effects of Molecular Size and Binding Affinity on Tumor Targeting. *Mol. Cancer Ther.* **2009**, *8* (10), 2861–2871.

(38) Choi, C. H. J.; Alabi, C. A.; Webster, P.; Davis, M. E. Mechanism of Active Targeting in Solid Tumors with Transferrin-Containing Gold Nanoparticles. *Proc. Natl. Acad. Sci.* **2010**, *107* (3), 1235–1240.

(39) Wang, A. Z.; Gu, F.; Zhang, L.; Chan, J. M.; Radovic-Moreno, A.; Shaikh, M. R.; Langer, R. S.; Farokhzad, O. C. Biofunctionalized Targeted Nanoparticles for Therapeutic Applications. *Expert Opin Biol Ther.* **2008**, *8* (8), 1063–1070.

(40) Von Hoff, D. D.; Mita, M. M.; Ramanathan, R. K.; Weiss, G. J.; Mita, A. C.; Lorusso, P. M.; Burris, H. A.; Hart, L. L.; Low, S. C.; Parsons, D. M.; et al. Phase I Study of PSMA-Targeted Docetaxel-Containing Nanoparticle BIND-014

in Patients with Advanced Solid Tumors. *Clin. Cancer Res.* **2016**, *22* (13), 3157–3163.

(41) Yatvin, M.; Weinstein, J.; Dennis, W.; Blumenthal, R. Design of Liposomes for Enhanced Local Release of Drugs by Hyperthermia. *Science (80-.).* **1978**, *202* (4374), 1290–1293.

(42) Plassat, V.; Wilhelm, C.; Marsaud, V.; Ménager, C.; Gazeau, F.; Renoir, J. M.; Lesieur, S. Anti-Estrogen-Loaded Superparamagnetic Liposomes for Intracellular Magnetic Targeting and Treatment of Breast Cancer Tumors. *Adv. Funct. Mater.* **2011**, *21* (1), 83–92.

(43) Chen, K. J.; Liang, H. F.; Chen, H. L.; Wang, Y.; Cheng, P. Y.; Liu, H. L.; Xia, Y.; Sung, H. W. A Thermoresponsive Bubble-Generating Liposomal System for Triggering Localized Extracellular Drug Delivery. *ACS Nano* **2013**, *7* (1), 438–446.

(44) Al-Ahmady, Z. S.; Al-Jamal, W. T.; Bossche, J. V.; Bui, T. T.; Drake, A. F.; Mason, A. J.; Kostarelos, K. Lipid-Peptide Vesicle Nanoscale Hybrids for Triggered Drug Release by Mild Hyperthermia in Vitro and in Vivo. *ACS Nano* **2012**, *6* (10), 9335–9346.

(45) Lee, E. S.; Gao, Z.; Kim, D.; Park, K.; Kwon, I. C.; Bae, Y. H. Super pH-Sensitive Multifunctional Polymeric Micelle for Tumor pHe Specific TAT Exposure and Multidrug Resistance. **2009**, *129* (3), 228–236.

(46) Koo, A. N.; Lee, H. J.; Kim, S. E.; Chang, J. H.; Park, C.; Kim, C.; Park, J. H.; Lee, S. C. Disulfide-Cross-Linked PEG-Poly(amino Acid)s Copolymer Micelles for Glutathione-Mediated Intracellular Drug Delivery. *Chem. Commun.* **2008**,

No. 48, 6570.

(47) Hatakeyama, H.; Akita, H.; Ito, E.; Hayashi, Y.; Oishi, M.; Nagasaki, Y.; Danev, R.; Nagayama, K.; Kaji, N.; Kikuchi, H.; et al. Systemic Delivery of siRNA to Tumors Using a Lipid Nanoparticle Containing a Tumor-Specific Cleavable PEG-Lipid. *Biomaterials* **2011**, *32* (18), 4306–4316.

(48) Lee, J. S.; Groothuis, T.; Cusan, C.; Mink, D.; Feijen, J. Lysosomally Cleavable Peptide-Containing Polymersomes Modified with Anti-EGFR Antibody for Systemic Cancer Chemotherapy. *Biomaterials* **2011**, *32* (34), 9144–9153.

(49) You, J. O.; Auguste, D. T. Nanocarrier Cross-Linking Density and pH Sensitivity Regulate Intracellular Gene Transfer. *Nano Lett.* **2009**, *9* (12), 4467–4473.

CHAPTER 2

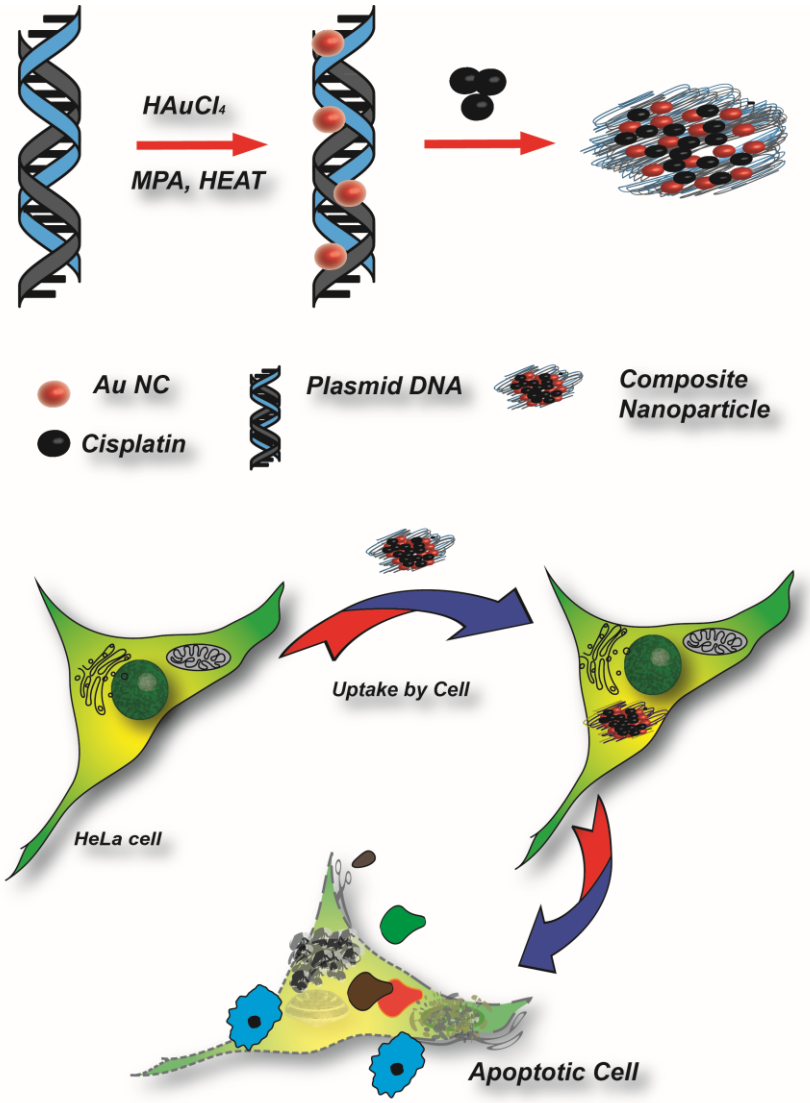

Interactive Luminescent Gold Nanocluster Embedded dsDNA and Cisplatin as Model Nanoparticle for Cancer Theranostics.

B. Chatterjee, A. K. Sahoo, S. S. Ghosh and A. Chattopadhyay, 2016. RSC Advances, 6, 113053-113057. Reproduced by permission of The Royal Society of Chemistry, Copyright RSC 2016.

ABSTRACT

Plasmid DNA embedded with luminescent gold nanoclusters were reacted with cisplatin to form composite nanoparticles (composite NPs) for theranostic application. The composite NPs delivered cisplatin to cervical cancer HeLa cells *in vitro*, inducing apoptosis mediated cell death. The luminescent gold nanoclusters were simultaneously used for cellular imaging.

Interactive Luminescent Gold Nanocluster Embedded dsDNA and Cisplatin as Model Nanoparticles for Cancer Theranostics

2.1 Introduction

The advent of theranostic agents promises to enhance the potential of targeted drug delivery with real-time tracking of the vehicle[1]. In this regard, biocompatible synthetic polymers have proven to be important hosts to organic and inorganic drugs and probes. The ease of synthesis and functionalization has helped improve their potential as carriers[2]. There are also micellar[3], liposomal[2] and virosomal carriers[4], which can efficiently host a myriad of payloads that may include DNA, drugs, siRNA, imaging molecules and have been used for their delivery *in vitro*. These carriers can also be made multifunctional through incorporation of individual entities in the same vehicle[5]. However, their equilibrium structures are subject to environmental variations and thus may release drugs on the way to the target[6]. Also, their (micron and sub-micron scale) dimensions prevent them from becoming the perfect choice for drug delivery [7]. The current trends in research indicate that multifunctional single component nanoscale carriers may become dominant players in this regard[8]. The key to success may lie in having a base structure, which can be engineered with ease and be able to host moieties with varying physicochemical properties.

A prominent candidate satisfying majority of the above mentioned criteria for the fabrication of nanoscale delivery vehicle is DNA. This is all the more exciting due to the availability of programmed synthetic DNA structures, in addition to their naturally occurring counterparts. That the nanostructures could be designed "*ab initio*" has opened new vistas in the form of DNA origami[9] with 2D and 3D architectures in the nanoscale regime. With deterministic structures, DNA origami has also been

employed for designing biosensors, theranostic agents, and nanorobots for biological applications[10]. The excellent biocompatibility[11], flexibility[12], and significant stability in cell lysates[13] make the DNA-based structures preferred choices for developing customized nanocarriers. Besides, the possibility of functionalization[14],[12] at the molecular level has helped design nanostructures, which facilitate targeted delivery of drugs and perform imaging simultaneously. For example, engineered nanovehicles having DNA as the core constituent are known to deliver small molecular drugs[9],[14], antibodies[10] and siRNA[15]. Also, self-assembled oligonucleotide nanotubes have been used for delivery of Cy3 to KB cells efficiently[16]. There is a report of M13 dsDNA being used for delivery of doxorubicin to MCF 7 cells; however, it failed to cause significant cytoxicity, while similar approach with the engineered form of DNA (via origami) proved more efficient[9]. The other option for construction of such structures originates from the natural forms of DNA.

Interestingly, majority of the aforementioned structures rely on Watson-Crick pairing and thus require cumbersome procedures for fabrication of the constituent structures, which is necessary for the assembly of complex structures[17], which may be one of the reasons for rather limited growth of the field. Moreover, due to the negative surface charge of the plasma membrane bare DNA molecule - either single stranded (ss DNA) - or double- stranded (dsDNA) - or its derivative structure, which is also negatively charged, compromises transport across the membrane. On the other hand, coupling with nanoparticles has been reported to impact increased efficiency of transfection of DNA[18].

In order to increase the theranostic potential of nanostructures based on DNA, conjugation of the probe is of vital importance. An optical probe–especially a

photoluminescence based one-incorporated in the nanostructure would confer an external handle in monitoring the entry of the vehicle in target tissues and in addition, release of the drug into the cellular environment. An important candidate in this regard could be the luminescent atomic clusters of gold. This becomes even more relevant when the recent surge in DNA based synthesis of noble metal atomic clusters is considered[19]. Significant photoluminescence quantum yield, large Stokes-shifted emission, high photostability, substantial two-photon excitation cross-section and biocompatibility make Au nanocluster an important candidate for theranostic applications. In an ideal scenario, the DNA, Au clusters and the drug ought to form composite nanostructures, which would be sufficiently stable to provide long circulation lifetime and deliver the drug at the target atleast passively through enhanced permeation and retention (EPR) effect.

2.2 Outline of the research work

1. The development of a novel composite nanoparticle having plasmid DNA as the basic platform with luminescent Au nanoclusters and anticancer drug cisplatin as the constituents for theranostic application is been established. While cisplatin has been used herein as a model drug for its anti-cell proliferative activity against model cancer cells, the luminescent Au nanoclusters have been used for simultaneous imaging of the cells.

2. The use of natural form of pDNA helped avoid the lengthy process of fabrication of a drug carrier based on conventional DNA origami or similar technique. Also, this is first time a natural form of DNA is being transformed into a drug carrier being embedded with luminescent Au nanoclusters.

3. The use of natural form of dsDNA as the basic building platform for the composite nanoparticle renders it bio-compatible.

4. Importantly, the use of cisplatin in conjunction with the dsDNA provided a perfect opportunity for forming spherically shaped nanoparticle. The shape and size of the nanoparticles were established using various analytical techniques such as transmission electron microscopy, field emission electron microscopy, atomic force microscopy and dynamic light scattering based particle size analysis.

5. That the size of the particles was about 100 nm (as measured using microscopy) and hydrodynamic size of 280 nm would make them eminently suitable for anti-cancer drug delivery using the principle of enhanced permeation and retention (EPR) effect.

6. The observation of pH dependence in the release of the drug (cisplatin) of *in vitro* from the carrier provides an added opportunity for drug delivery.

7. The anti-cell proliferative activity of the synthesized composite nanoparticle was tested using HeLa (human cervical carcinoma) cells. The enhanced cytotoxicity of the composite nanoparticle enumerated the efficient transport of the cisplatin to the cells. The delivery of the composite nanoparticle to the cells *in vitro* was probed using confocal microscopy.

8. It was further observed that composite nanoparticle raised the intra-cellular ROS level as has been established by cytometry based assay (FACS based DCFHDA assay). The increased ROS level translated into amplified expression of the caspase-3 enzyme, which is known to lead to apoptosis. Thus, caspase -3

assay was performed and it established increased number of caspase positive cells in case of composite nanoparticle as compared to the controls.

9. Furthermore, cell cycle analysis and the FESEM images also evidenced that composite nanoparticle led to apoptosis mediated cell death.

10. Overall, the current work demonstrated efficiency of the synthesized composite nanoparticle being made of ds DNA, highly luminescent Au nanoclusters and cisplatin. The composite nanoparticle thus synthesized served the dual function of drug delivery plus release and imaging. The ds DNA being the primary structural constituent of the nanoparticle would make them facile delivery vehicle for model cancer theranostics.

2.3 Experimental section

2.3.1 *Chemicals:* $HAuCl_4$ (Au, 17 wt % in dilute HCl; 99.99%), mercapto propionic acid (MPA), cis-diamineplatinum (II) dichloride (cisplatin) were obtained from Sigma-Aldrich and used as received. Milli-Q grade water (>18 MΩ cm^{-1}, Millipore) was used in all experiments.

2.3.2 *Characterization of nano composite:* UV-vis spectra were measured by PerkinElmer Lambda 25 spectrophotometer. Fluorescence spectra were measured by using a spectrophotometer (Fluorolog −3, Horiba Jobin Edison, NY, USA).

2.3.3 *Transmission electron microscopy (TEM):* Sample was diluted to optimum level and then 7 μL of it was drop-cast over a TEM grid, allowed to dry for overnight and was then analyzed by a JEM 2100; Jeol machine.

2.3.4 *Field emission scanning electron microscopy (FESEM):* Treated cellular samples were trypsinized and were resuspended in 1 ml phosphate buffer saline

(PBS). Cells were fixed with chilled 70 % ethanol from which 7 µL was drop-cast on a clean and autoclaved cover slip, which was allowed to air-dry. Samples were coated by gold before being analyzed by FESEM (Sigma, Zeiss).

2.3.5 *Atomic force microscopy (AFM):* For composite nanoparticles sample was diluted to optimum level and then 7 µL of it was drop-cast over a cover slip, which was allowed to dry for overnight. Then the sample was analyzed with AFM 5500 series, Agilent.

2.3.6 *Synthesis of cisplatin loaded composite nanoparticles:* Different ratios of concentration of the cisplatin and DNA were incubated with as- synthesized DNA-Au NCs in the dark for 1 h followed by centrifugation at 10,000 rpm for 5 min. The supernatant was discarded to remove the free cisplatin and redispersed in PBS followed by recording of emission at 580 nm. The binding of cisplatin with DNA-Au NCs resulted in loss in emission intensity of the clusters, which was probed by fluorescence spectroscopy. Then a ratio of cisplatin/base pair 0.55 was chosen for further experiments, which provided sufficient luminescence for cellular bioimaging.

2.3.7 *Loading efficiency:* The loading efficiency of the composite NPs were calculated with following formula:

$$\textbf{Loading efficency} = \frac{\textbf{Total cisplatin} - \textbf{Cisplatin in supernatant}}{\textbf{Total cisplatin}}$$

Cisplatin concentration was measure by UV spectrometer at 210 nm.

2.3.8 *Confocal, Z stacking and Epi-fluorescence Microscopy:* HeLa cells were grown on a cover slip (which was already placed inside a cell culture plate) for 12 h in DMEM medium in the presence of 5% CO_2 at 37 ^{o}C. After that the cells were subjected to the composite nanoparticle treatment (with concentration half of

their IC_{50} and was added directly in the medium) and were incubated for 3 h in DMEM medium in the presence of 5% CO_2 at 37 ^oC. The medium was then discarded and the plate was washed with PBS twice and the cells while in PBS were fixed with 0.1 % formaldehyde and then analyzed by microscope (LSM 880, Zeiss).

2.3.9 *Release study:* Cisplatin concentration is measured by taking its absorbance at 210 nm by UV-vis spectroscopy. For release studies the respective samples after the premediated period of time in buffers (both pH 7 and pH 4.5) were centrifuged at 15000 rpm and the supernatant was collected and checked for the amount of cisplatin released into the medium at that particular time interval. The percentage of cisplatin released with the respect to concentration of cisplatin released at 0h.

2.3.10 *Cell viability assay by MTT:* For both HeLa and HEK 293 cells 5×10^3 cells/well were seeded in 96-well microplate and were allowed to grow for 12 h in DMEM medium in the presence of 5% CO_2 at 37 ^oC. After that the cells were subjected to various concentrations of the DNA-Au- NC, cisplatin and DNA-Au-NC-cisplatin (composite nanoparticles) for 48 h. Then 7.0 µL of MTT [3-(4,5-dimethylthiazol-2-yl)-2,5-diphenyltetrazolium bromide] was added to each well of the microplate and kept for 2 h in 5% CO_2 at 37 ^oC for the formation of formazan. After 2 h of incubation, the medium was removed and 60 µL of DMSO was added to each well for the development of purple color due to the formation of formazan, the absorbance of which at 550 nm was taken as a measure of cell viability.

2.3.11 *Caspase 3 assay:* HeLa cells were seeded at 1×10^5 cells/well in a six-well plate and were allowed to grow for 12 h in DMEM medium in the presence of

5% CO_2 at 37 ^oC. Then the cells were treated with the DNA-Au-NC, cisplatin, and DNA-Au-NC-cisplatin (composite nanoparticles) at their IC_{50} values for 48 h. Then cells were trypsinized and were further fixed with 0.1% formaldehyde in PBS for 15 min at room temperature. After recollecting cells by centrifuging them at 650 rcf for 5 min and at 4 ^oC they were re-suspended in PBS with 0.5 % Tween 20 (membrane permeabilization solution) and centrifuged immediately at 650 rcf for 7 min. Then the cells were washed twice with PBS and were re-suspended in PBS. Finally, cells were treated with PE conjugated Rabbit Anti-Active-Caspase-3 (Catalog no. 550821, BD Biosciences) for 30 min in the dark at 37 ^oC and then the samples were analyzed by flow cytometer using Cell Quest pro in FL 2 H (red emission) fluorescence channel for 15000 cells for each sample.

2.3.12 *Cell cycle analysis:* HeLa cells were seeded at 1 × 10^5 cells/well and were allowed to grow for 12 h in DMEM medium in the presence of 5% CO_2 at 37 ^oC. Then the cells were treated with the DNA-Au-NC, cisplatin, and DNA-Au NC- cisplatin (composite nanoparticles) at their IC_{50} values for 48 h. Then cells were trypsinized and were recollected by centrifuging them at 650 rcf for 5 min at 4 ^oC. Cells were then fixed with 1 mL 70 % chilled ethanol by adding it drop by drop while vortexing it and then were kept at -20 ^oC for 1 h. Cells were then centrifuged at 650 rcf for 5 min at 4 ^oC; supernatant was discarded and the pellet was resuspended in 1 mL PBS. Cells were then subjected to RNase (100 µg/ mL) treatment and were incubated at 55 ^oC for 1 h. Then propidium iodide (40 µg/ mL) was added with 0.01% Triton X-100 into the cells and samples were analyzed by flow cytometer using Cell Quest pro in FL 2 A (red emission) fluorescence channel for 15000 cells for each sample.

2.3.13 *Reactive oxygen species (ROS) generation measurement:* HeLa cells were seeded at 1 × 10^5 cells/well and were allowed to grow for 12 h in DMEM medium in the presence of 5% CO_2 at 37 ºC. Then the cells were treated with the DNA-Au-NC, cisplatin, and DNA-Au NC-cisplatin (composite nanoparticles) at their IC_{50} values for 3 h. Then cells were trypsinized and were recollected by centrifuging them at 650 rcf for 5 min at 4 ºC. The cells were then re-suspended in 1 mL fresh DMEM with 5.0 µL of 1.0 mM of DCFH-DA being added to it and incubated for 10 min at 37 °C. After incubation, the samples were analyzed for the fluorescence of DCF by flow cytometer using Cell Quest pro in FL1 H (green emission) fluorescence channel for 15 000 cells for each sample. Results were analyzed with WinList 3DTM software (Variety Software House).

2.3.14 *Quantum yield measurement:* Quantum yield (QY) of DNA-Au-NC was measured by established protocol and taking quinine sulfated in 0.10 M H_2SO_4 solution as the standard. Equation used for calculation is

$$Q_{DNA\,NC} = Q_{Ref}\,\frac{m_{DNA\,NC}}{m_{Ref}}\,\frac{n_{DNA\,NC^2}}{n_{Ref^2}}$$

Here Ref stands for standard, Q is quantum yield, m stands for the slope of the plot of integrated fluorescence intensity vs. absorbance and n is for the refractive index (solvent in both cases is water). We used the same solution for UV-vis and fluorescence measurements.

2.3.15 *Statistical analysis:* Statistical studies on MTT data and cell cycle data have been performed with one-way ANOVA test.

2.4 Results and discussion

Experimentally, the Au nanoclusters of size 1.38 ± 0.54 nm (**Figure 2.1 a, b**) were synthesized in the presence of plasmid DNA extracted from *Escherichia Coli*. Briefly, an aqueous mixture of plasmid DNA, $HAuCl_4$ and mercaptopropionic acid (MPA) were subjected to a thermal cycle. The product so obtained was then brought to room temperature. The UV-Vis spectrum of the product medium consisted of an absorption in the region of 260 nm (**Figure 2.2 a**), which corresponds to absorption by the DNA molecule. However, there was no peak in the visible region thus discounting the possibility of formation of surface plasmon resonance active Au nanoparticles in the reaction medium. On the other hand, the medium – when excited by 320 nm light – exhibited an emission peak at 580 nm (**Figure 2.2 b**), which indicated the formation of Au nanoclusters. Owing of their size, which is comparable to fermi wavelength of

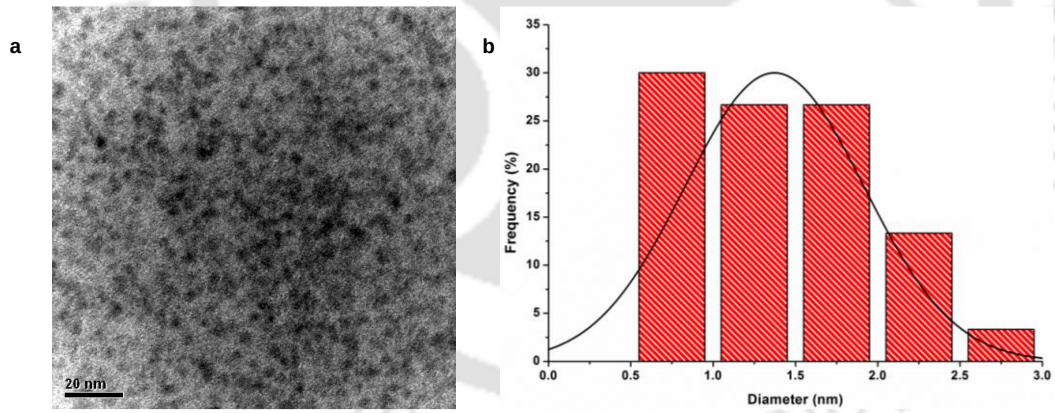

Figure 2.1: a) *TEM micrograph of DNA gold nanocluster (DNA Au NC)* ***b)*** *Size distribution of the synthesized gold nanoclusters (DNA Au NCs) embedded in DNA. The average size of the particle was calculated to be 1.38 ± 0.54 nm in the TEM analysis.*

electron, nanocluster displays a discretization of its energy levels with high luminescence quantum yield[20]. The notion was further corroborated by AFM study

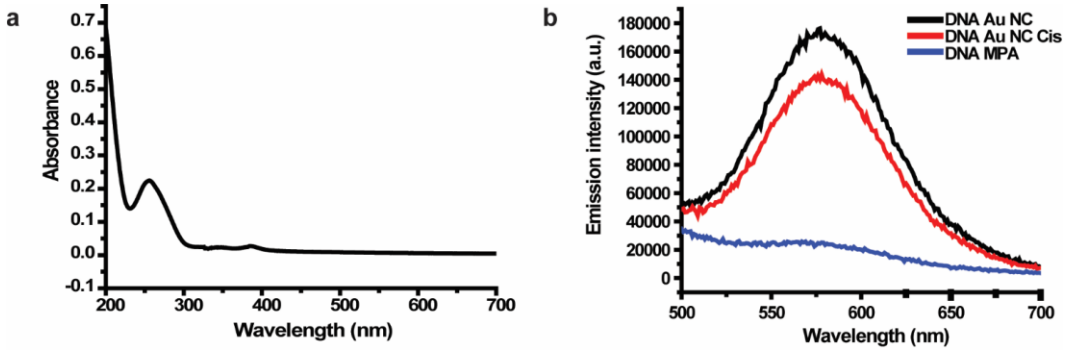

Figure 2.2: a) *UV-vis absorption spectrum of the synthesized composite nanoparticle marking the absence of characteristic SPR peak of gold. The peak at 260 can be attributed to the absorption by DNA.* ***b)*** *Luminescence emission of the DNA- gold nanocluster (DNA Au NC), that when interacted with cisplatin, and only DNA - MPA mixture.*

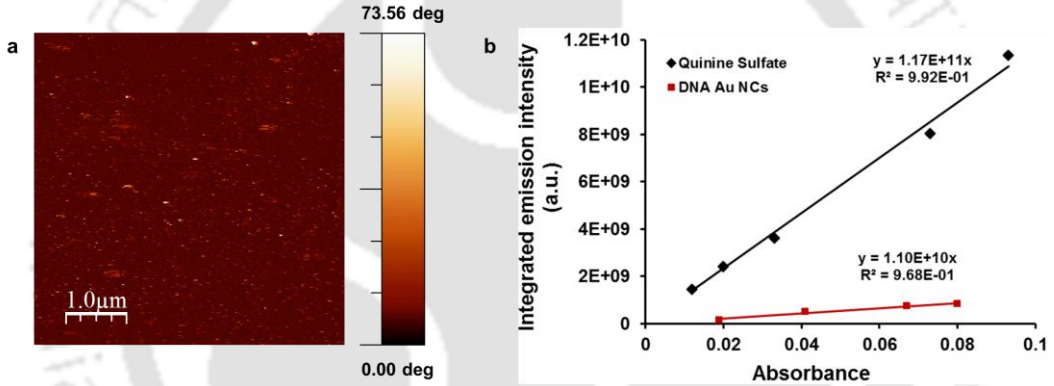

Figure 2.3: a) *AFM images of the DNA Au NCs* ***b)*** *Integrated fluorescence intensity vs absorbance plot of DNA Au NCs and quinine sulphate. Quinine sulphate was used here as a standard to determine the quantum yield of the synthesized DNA-Au-NC (which was found to be 5.01%).*

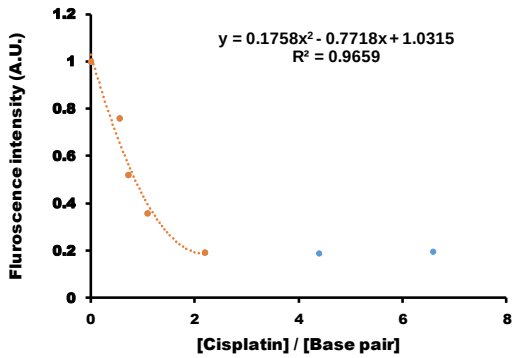

Figure 2.4: *Gradual loss in fluorescence of DNA Au NCs with increasing concentration of cisplatin. The plot was fitted with a second order polynomial relationship between fluorescence intensity and [cisplatin]/ [base pair].*

(**Figure 2.3 a**). Besides, DNA based fluorescent gold nanoclusters are established in the literature[21]. The quantum yield of emission was measured to be 5% (**Figure 2.3 b**), with the emission of quinine sulfate being taken as the reference.

Interestingly, when the so-synthesized Au nanoclusters in DNA were incubated with varying concentration of cisplatin in the dark for 1 h, it resulted in the loss of luminescence of the clusters. This indicated interaction between cisplatin and the cluster embedded DNA. The luminescence intensity decreased monotonically with the concentration of cisplatin. The variation of intensity with [cisplatin]/ [base pair] followed a second order polynomial relationship (**Figure 2.4**). For the further experiments, a ratio of [cisplatin]/ [base pair] 0.55 was chosen as it yielded product with sufficient luminescence required for imaging. Transmission electron microscopy (TEM) investigation of cisplatin treated DNA containing Au nanoclusters revealed the formation of spherical nanoparticles with an average diameter of 90 ± 9 nm (**Figure 2.5 a**); the corresponding size distribution is given in the **Figure 2.5 b**. The uniformity in particle size and shape indicated the robustness of the structure based on the interaction between the cluster containing DNA and cisplatin. High resolution TEM images [**Figure 2.5 a inset**] indicated the presence of smaller particles (of sizes less than 2 nm) in each of the bigger particles, which could well be the Au nanoclusters.

That the composite nanoparticles were nearly spherical was further confirmed by atomic force microscopy (AFM) (**Figure 2.6 a, b**). AFM images also revealed the formation of particles with average size 106 ± 39 nm (**Figure 2.6 c**). The small difference in the particle sized measured by AFM and TEM could be due to compactness of the particles when under vacuum (in TEM) as opposed to ambient condition evaporated arrays of particles on two-dimensional glass slide (for AFM

measurement). The spherical shape was further confirmed with FESEM study (**Figure 2.6 d**).

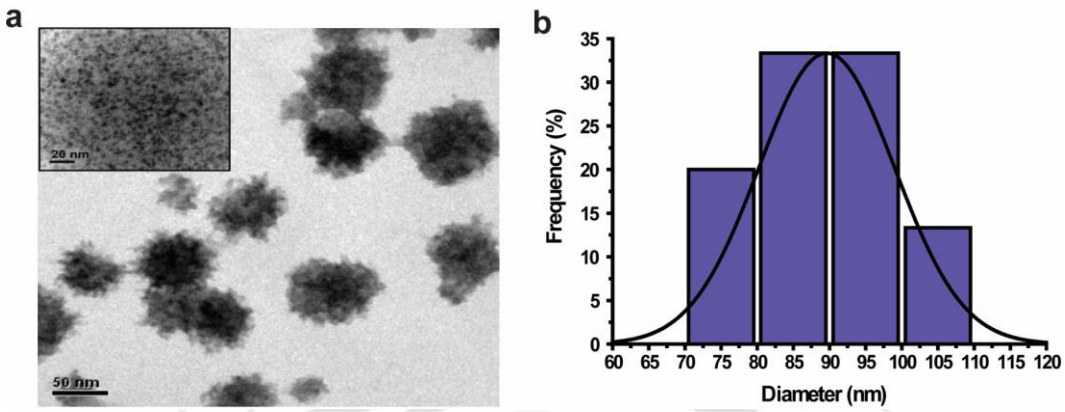

Figure 2.5: a) *TEM image of the composite nanoparticle, with a magnified image (inset) showing the presence of Au NCs.* ***b)*** *Composite NPs size distribution based on TEM image.*

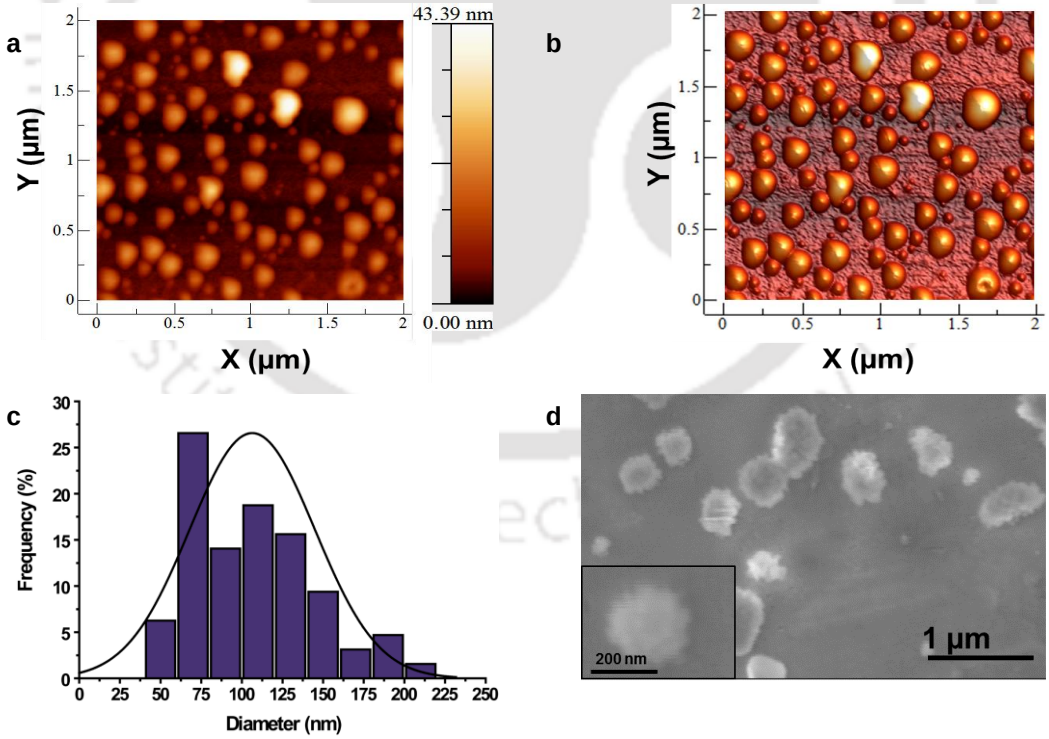

Figure 2.6: a) *AFM image of the composite NPs and its* ***b)*** *3D view.* ***c)*** *Composite NPs size distribution based on AFM images* ***d)*** *FESEM image of the composite NP.*

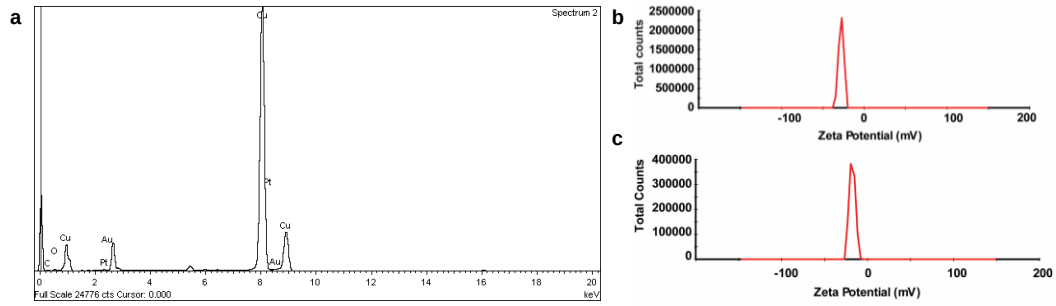

Figure 2.7: a) *Energy dispersive X-ray (EDX) spectrum of the synthesized composite NPs showed the presence of both gold and platinum and it meant the presence of DNA Au NCs and cisplatin both in the synthesized composite NPs.* ***b)*** *Zeta potential distribution graph of the Au nanoclusters (DNA Au NCs) c) Zeta potential distribution graph of the composite nanoparticles.*

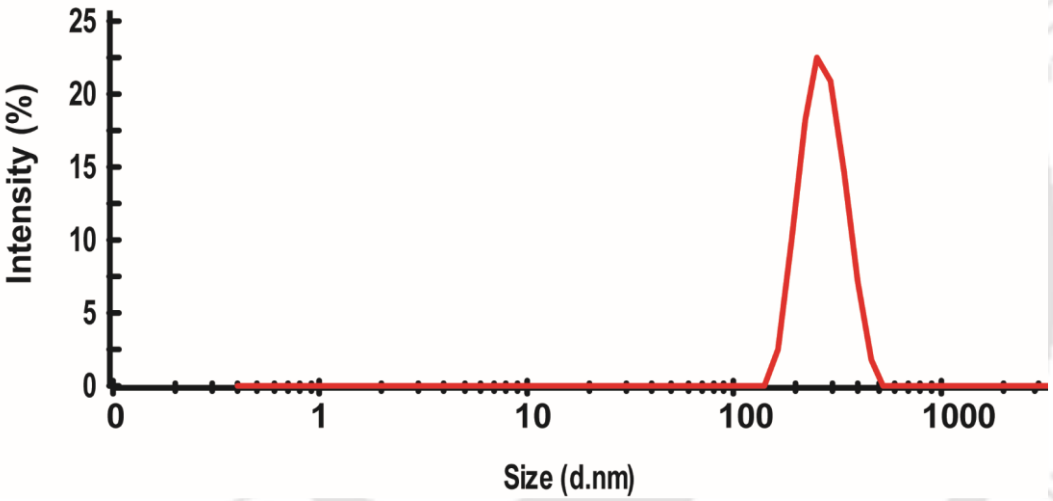

Figure 2.8: *Hydrodynamic size distribution of the composite NPs. The average hydrodynamic diameter of the composite NPs was 280 nm.*

The presence of Au and Pt in the composite was confirmed from energy dispersive X-ray (EDX) spectrum, which was recorded along with the TEM analysis of the same sample **Figure 2.7 a**. The interaction of cisplatin with the DNA containing nanoclusters and formation of the composite nanoparticle were further confirmed by the zeta potential measurements. While DNA with the clusters exhibited a value of -27.8 mV (**Figure 2.7 b**), the same upon addition with cisplatin resulted in a value of -17.7 mV (**Figure 2.7 c**). Further, the hydrodynamic diameter of the composite

nanoparticles was measured to be 280 nm (**Figure 2.8**). The above results imply that the cisplatin not only was bound with the purine (A and G) bases (as is known from the literature)[22] but also possibly interacted with the nanoclusters present in the DNA, which might have assisted in the formation of the spherical nanoparticle. Apparently, the drug molecule here played both structural and functional roles as it assisted in the formation of nano-structures while at the same time would serve the purpose of anticancer activity. Further, the above size suggests that the cisplatin containing luminescent nanoparticles could be ideal carriers for the delivery of the drug to leaky cancer tissues through EPR effect [23]. The loading efficiency of the composite NP was found to be 86 ± 4 % when the ratio of [cisplatin]/ [base pair] viz. 0.55. Further experiments were carried out with this ratio of [cisplatin]/ [base pair].

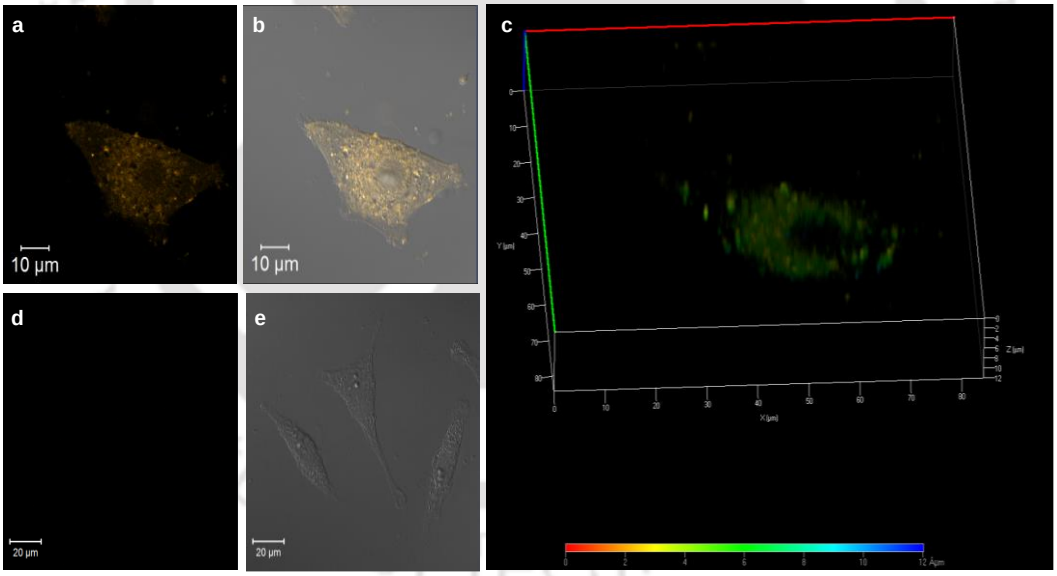

Figure 2.9: *Fluorescence images of HeLa cell treated with the composite nanoparticle.* ***a)*** *Fluorescence image of the HeLa cell showing characteristic yellow emission of the DNA Au NC and* ***b)*** *merged image (with bright field and fluorescence images merged together) of the same cell.* ***c)*** *A 12 µm z-stack projection of the treated cell showing the uptake of the composite nanoparticles; here the scale depicted shows the distance of the entities from the cove slip.* ***d)*** *Fluorescence image of the control cells showing no fluorescence and* ***e)*** *merged image (with bright field and fluorescence images merged together) of the control cells.*

Fluorescence microscopy was performed to assess the imaging potential of the composite nanoparticle. HeLa cells were incubated for 3 h with the composite nanoparticle and they were then probed by fluorescence microscopy. The cells exhibited bright yellow fluorescence due to Au NCs (**Figure 2.9 a, b**). The results indicated that the composite nanoparticles were readily taken up by the cells. The uptake of the composite nanoparticles was further established by z-stacking (**Figure 2.9 c**), where the green fluorescence indicated the up-taken composite nanoparticle. However, the control cells lacked any fluorescence (**Figure 2.9 d, e**). The ready uptake of the composite nanoparticles can be attributed to its compact nature and size, rendering it capable of penetrating through the cellular membrane without the use of any transfecting agent [24].

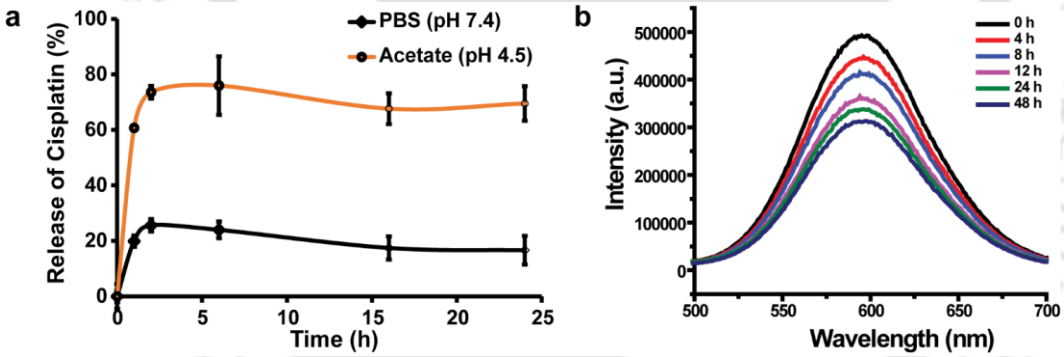

Figure 2.10: a) *Release profile of cisplatin from the composite NPs in PBS (pH 7.4) and acetate buffer (pH 4.5).* ***b)*** *Emission of the composite NPs in PBS at 0 h, 4 h, 8 h, 12 h, 24 h and 48 h. the negligible loss of fluorescence after 48 h establishes the stability of the composite NP at physiological pH.*

In vitro release of cisplatin from the composite nanoparticles was evaluated at both acidic condition and at physiological pH. The composite exhibited a spurt in cisplatin release in 2 h (**Figure 2.10 a**), when added to acetate buffer (pH 4.5). About 76% of the encapsulated drug was released by that time and no significant increase could be observed thereafter. On the other hand, a release of 26% by 2 h in phosphate

buffer (pH 7.4), emulating the physiological pH condition (**Figure 2.10 a**), was observed. The observations demonstrated a pH sensitive release of the drug from the composite. The pH dependence of the release profile ensures that majority of the drug is released at acidic pH only and reduce the random drug spillage at physiological pH. Now if the composite NPs are delivered in vivo, required pH for drug release can be primarily reached when the composite NPs are inside the cells (perhaps the lysosomal compartment)[14]. It also ensures that if not taken up the by cells, the release of the cisplatin preferably would occur at tumor microenvironment, where pH can dip down to 5.8[23], thus avoiding killing normal cells. As the cisplatin has already been reported to be stable at low pH[25] so any structural change that may lead to loss of functionality can't be anticipated. The release can be attributed to the unwinding of the plasmid DNA itself at low pH and disassembling of the whole composite. Stability of the composite NPs was checked in the PBS (**Figure 2.10 b**). Fluorescence intensity of the as synthesized composite NPs was substantially retained even after 48 h in PBS which implies that the composite NPs is quite stable and suitable for cellular uptakes. The observed loss in fluorescence is in compliance with the release data, which also suggested that some amount of the composite NP would be destabilized and released the drug in the PBS.

That the luminescent composite nanoparticle delivered the drug cisplatin to the cancer cells was further tested by 3- (4, 5-dimethylthiazol-2-yl)-2, 5-diphenyltetrazolium bromide (MTT) assay (a cell viability assay). The cell viability was thus measured following treatment of the HeLa cells for 48 h, with free cisplatin, nanocluster containing DNA and the composite nanoparticle (consisting of DNA, Au nanoclusters and cisplatin) at various concentrations. The results as shown in **Figure 2.11 a**, indicated that that DNA with the nanocluster was non-cytotoxic, while cisplatin

and the composite nanoparticle led to the killing of cells conspicuously. Importantly, IC_{50} value of the only drug was found to be 6.57 µg/ mL, whereas the same for the drug encapsulated in the composite nanoparticle was measured to be 3.8 µg/ mL. MTT was also performed on the HEK 293 cells to check the effect of the composite NPs on normal cells. Here also the composite NPs displayed an improved cytotoxicity than the drug itself. The IC_{50} value for the composite NPs was 3.8 µg/mL compared to 4.4 µg/mL with only drug (**Figure 2.11 b**). This lowering of drug IC_{50} concentration when encapsulated in the composite nanoparticle is important for its potential *in vivo* applications. Further, that the DNA containing Au NCs were found to be non-cytotoxic is valuable for the use of the composite as a drug delivery vehicle.

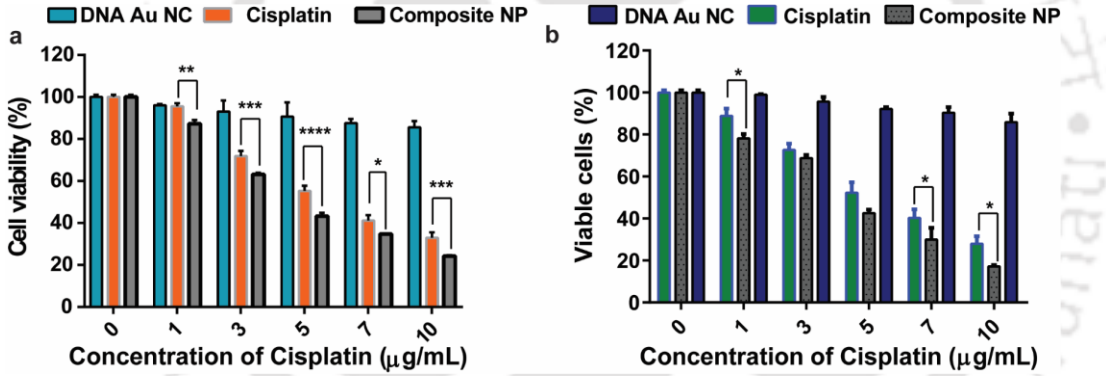

Figure 2.11: *MTT assay on* ***a)*** *HeLa (cancer cells)* ***b)*** *HEK (Non-Cancer cells) results. The values are represented as mean ± SD of results from three individual experiments. Statistical test was carried out to find out the statistical significance for each concentration between cisplatin and composite NPs. The statistical significance is denoted by ★ ($p < 0.05$), ★★ ($p < 0.005$), and ★★★ ($p < 0.001$)*

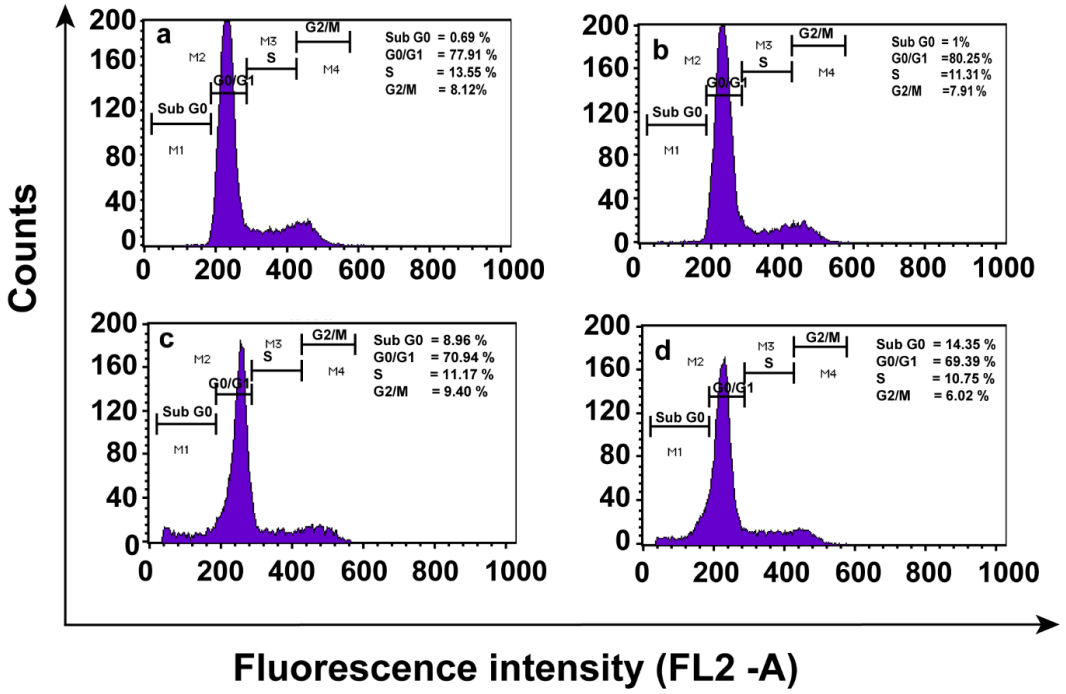

Figure 2.12: *Cell cycle analysis with propidium iodide (PI) staining* ***(a-d)****. The results correspond to* ***a)*** *control,* ***b)*** *DNA-Au-NC,* ***c)*** *cisplatin and* ***d)*** *composite nanoparticle treated cells. The results confirmed the evolved cytotoxicity of the composite nanoparticle over free cisplatin.*

Cisplatin is a conventional anti-cancer drug; it is known to cause DNA damage, which finally leads to apoptosis-mediated cell death[20]. To probe the mechanism of cell death induced by the current composite nanoparticle, flow cytometry based cell cycle analysis was performed. For this, cells were incubated with the composite nanoparticle for the aforementioned period at the IC_{50} dose and then were checked for the cell cycle analysis by using propidium iodide staining method. Results (**Figure 2.12**) demonstrated that all the stages of cell cycle remained almost unaltered except sub-G0 population, which corresponds to apoptotic cells. It was also found that the control (**Figure 2.12 a**) and Au nanocluster containing DNA (only) treated cells showed a feeble 1% sub-G_0 population (**Figure 2.12 b**). Whereas, the cells treated with free drug (only cisplatin) had 8.96% (**Figure 2.12 c**) of sub-G0 apoptotic population HeLa cells treated with the composite nanoparticle had sub-G0 apoptotic population of 14.35% of

the (**Figure 2.12 d**) which is significantly higher than that obtained using the free drug nanoparticles. The results are summarized in **Figure 2.13 a** bar graph and in **Figure 2.13 b**.

a

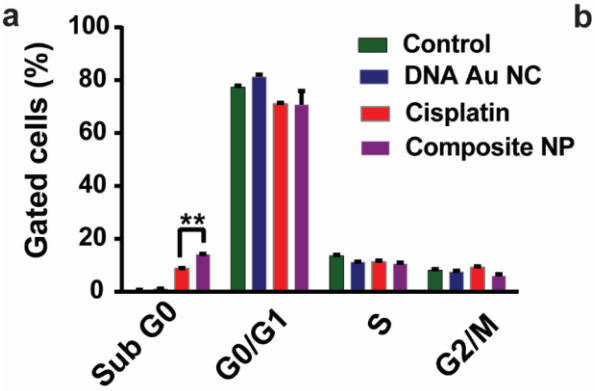

b

Treated with	Sub G0 (%)
Control	1
DNA Au NC	1
Cisplatin	8.96
Composite NP	14.35

Figure 2.13: a) *Summary of the cell cycle study stating the statistically significant improved cytotoxicity of the composite nanoparticle over the free drug. The statistical significance is denoted by ★ ($p < 0.05$), ★★ ($p < 0.005$), and ★★★ ($p < 0.001$).* ***b)*** *Summary of the cell cycle.*

Overall, the above results reaffirmed that the composite nanoparticle delivered the drug (cisplatin) to the cancer cells efficiently, which eventually led to apoptotic cell death. The aforementioned observations were validated by the FESEM imaging of the treated cells. The results as shown in (**Figure 2.14 a**) clearly indicated lack of any anomaly on the control cells; however, the formation of the apoptotic bodies and membrane blebbing were observed in treated cells (**Figure 2.14 b**), which are the key indicators of the apoptosis. Thus the results provided sufficient evidence for the composite nanoparticle mediated delivery of cisplatin and consequent induction of apoptosis with high efficiency at a lower dose of the drug.

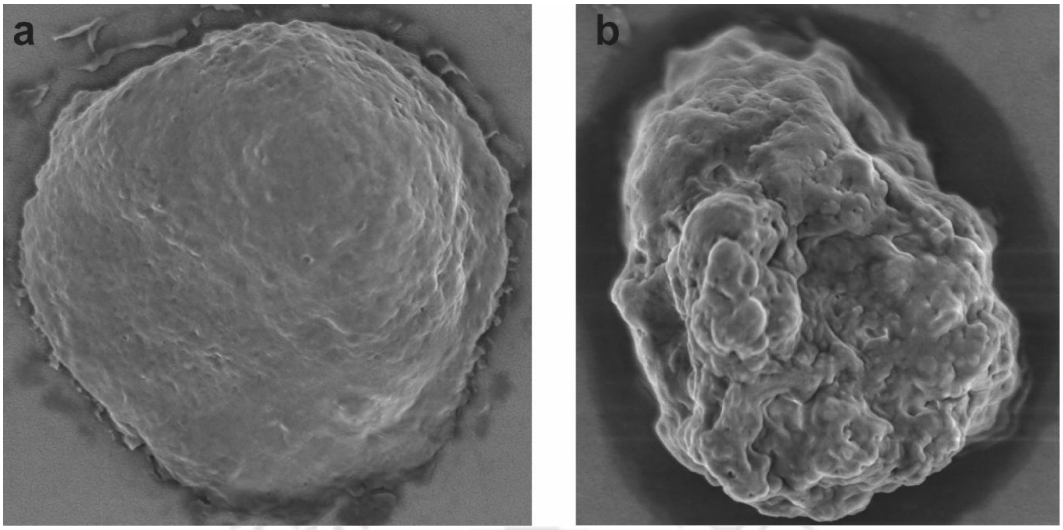

Figure 2.14: *FESEM images of the **a)** control and **b)** treated cells, where the treated cells showed the presence of apoptotic bodies, whereas the control cells lacked it.*

It is important to mention here that further experiments suggested that enhanced Caspase 3 formation, which is an essential indicator of apoptosis, was induced in the composite nanoparticle treated cells. Cells were treated with the drug and composite nanoparticle at its IC_{50} value and then they were checked for the Caspase 3 level using flow cytometry analysis. Whereas, a low level caspase 3 expression was found in the control cells (**Figure 2.15 a**) and cells treated with the DNA Au NC (**Figure 2.15 b**), Cells treated with the composite nanoparticle showed the highest quantum of the Caspase 3 (**Figure 2.15 d**), which was followed by the free drug (**Figure 2.15 c**).

Recent studies indicate the generation of mitochondrial reactive oxygen species (ROS) when the cells are treated with cisplatin[26]. In the current context, the treated cells displayed a high level of ROS generation at IC_{50} value with the composite nanoparticle and the same with a lower value in case of the free drug (**Figure 2.16**). Enhanced level of the ROS generation with composite nanoparticle highlights the possibility of better transport and delivery of the drug (in the form of the composite nanoparticles) as the

prime reason for the augmented cytoxicity of the composite nanoparticle vis-à-vis the free drug.

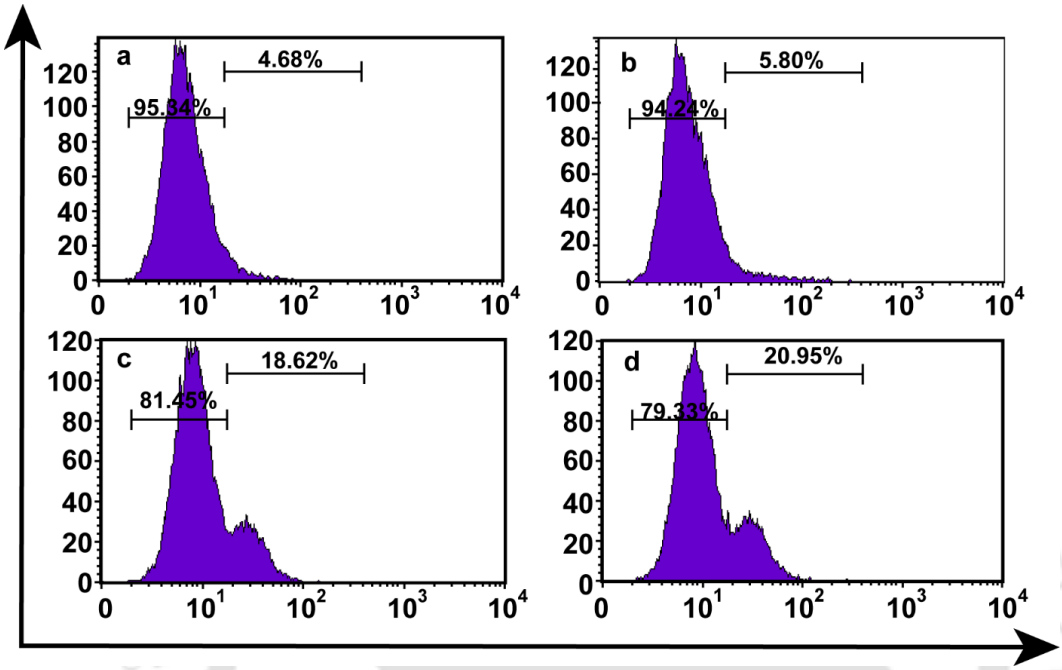

Figure 2.15: *Caspase study involving* ***a)*** *control cells and those treated with* ***b)*** *DNA - Au NC;* ***c)*** *cisplatin;* ***d)*** *composite nanoparticle. The results showed higher quanta of caspase positive cells in case of composite nanoparticle as compared to free cisplatin treated cells.*

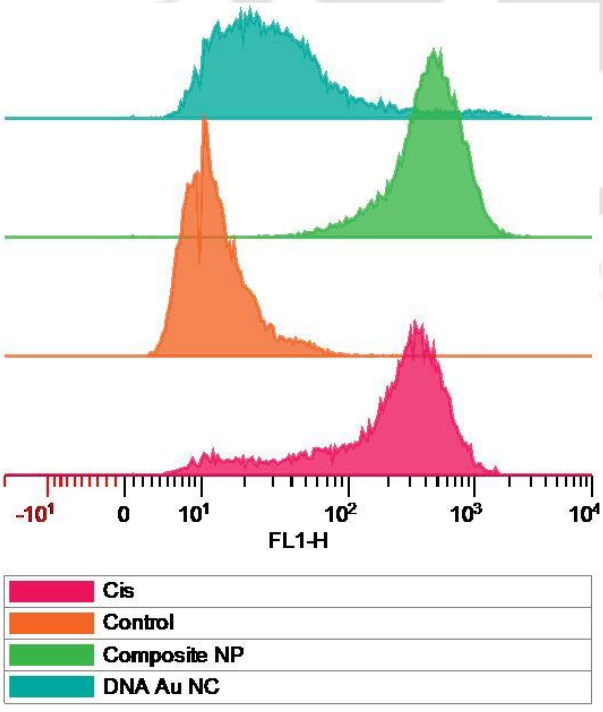

Figure 2.16: *ROS profile with the prominent shift observed in case of composite nanoparticle and cisplatin in comparison to the control cells.*

2.5 Conclusions

In essence, a novel DNA –Au-nanocluster- cisplatin composite nanoparticle have been developed that serves the dual purpose of cellular imaging and drug delivery. The composite nanoparticle showed augmented cellular cytotoxicity in comparison to free drug and provided an option for pH triggered release. Simultaneously, the composite also proved to be a possible imaging agent. With the DNA as the basic platform - in conjunction with Au NCs, the composite is biocompatible. The sizes and shapes of the nanoparticles, the ease of their formation and efficient incorporation and delivery of the drug cisplatin to cancer cells provide a new platform for drug delivery using natural form of DNA as the primary vehicular component, which has a high potential for clinical translation.

2.6 References

(1) Kelkar, S. S.; Reineke, T. M. Theranostics: Combining Imaging and Therapy. *Bioconjug. Chem.* **2011**, *22* (10), 1879–1903.

(2) Kamaly, N.; Xiao, Z.; Valencia, P. M.; Radovic-Moreno, A. F.; Farokhzad, O. C. Targeted Polymeric Therapeutic Nanoparticles: Design, Development and Clinical Translation. *Chem. Soc. Rev.* **2012**, *41* (7), 2971–3010.

(3) Guthi, J. S.; Yang, S.-G.; Huang, G.; Li, S.; Khemtong, C.; Kessinger, C. W.; Peyton, M.; Minna, J. D.; Brown, Kathlynn C. and Gao, J. NIH Public Access. *Mol Pharm.* **2010**, *7* (1), 32–40.

(4) Yoo, J.-W.; Irvine, D. J.; Discher, D. E.; Mitragotri, S. Bio-Inspired, Bioengineered and Biomimetic Drug Delivery Carriers. *Nat. Rev. Drug Discov.* **2011**, *10* (7), 521–535.

(5) Cole, J. T.; Holland, N. B. Multifunctional Nanoparticles for Use in Theranostic Applications. *Drug Deliv. Transl. Res.* **2015**, *5* (3), 295–309.

(6) Mura, S.; Nicolas, J.; Couvreur, P. Stimuli-Responsive Nanocarriers for Drug Delivery. *Nat. Mater.* **2013**, *12* (11), 991–1003.

(7) Felice, B.; Prabhakaran, M. P.; Rodríguez, A. P.; Ramakrishna, S. Drug Delivery Vehicles on a Nano-Engineering Perspective. *Mater. Sci. Eng. C* **2014**, *41*, 178–195.

(8) Xie, J.; Chen, K.; Huang, J.; Lee, S.; Wang, J.; Gao, J.; Li, X.; Chen, X. PET/NIRF/MRI Triple Functional Iron Oxide Nanoparticles. *Biomaterials* **2010**, *31* (11), 3016–3022.

(9) Jiang, Q.; Song, C.; Nangreave, J.; Liu, X.; Lin, L.; Qiu, D.; Wang, Z. G.; Zou, G.; Liang, X.; Yan, H.; et al. DNA Origami as a Carrier for Circumvention of Drug Resistance. *J. Am. Chem. Soc.* **2012**, *134* (32), 13396–13403.

(10) Pei, H.; Zuo, X.; Zhu, D.; Huang, Q.; Fan, C. Functional DNA Nanostructures for Theranostic Applications. *Acc. Chem. Res.* **2014**, *47* (2), 550–559.

(11) Schüller, V. J.; Heidegger, S.; Sandholzer, N.; Nickels, P. C.; Suhartha, N. A.; Endres, S.; Bourquin, C.; Liedl, T. Cellular Immunostimulation by CpG Sequence-Coated DNA Origami Structures. *ACS Nano* **2011**, *5* (12), 9696–9702.

(12) Mikkilä, J.; Eskelinen, Antti-Pekka Niemelä, E. H.; Linko, V.; Frilander, M. J.; Törmä, P.; Kostiainen, M. A. Virus-Encapsulated DNA Origami Nanostructures for Cellular Delivery. *Nano Lett.* **2014**, *14*, 2196–2200.

(13) Mei, Q.; Wei, X.; Su, F.; Liu, Y.; Youngbull, C.; Johnson, R.; Lindsay, S.; Yan,

H.; Meldrum, D. Stability of DNA Origami Nanoarrays in Cell Lysate. *Nano Lett.* **2011**, *11* (4), 1477–1482.

(14) Chang, M.; Yang, C.; Huang, D. Supporting Information Aptamer-Conjugated DNA Icosahedral Nanoparticles as a Carrier of Doxorubicin for Cancer Therapy. *ACS Nano* **2011**, *5* (8), 1–10.

(15) Lee, H.; Lytton-Jean, A. K. R.; Chen, Y.; Love, K. T.; Park, A. I.; Karagiannis, E. D.; Sehgal, A.; Querbes, W.; Zurenko, C. S.; Jayaraman, M.; et al. Molecularly Self-Assembled Nucleic Acid Nanoparticles for Targeted in Vivo siRNA Delivery. *Nat. Nanotechnol.* **2012**, *7* (June), 389–393.

(16) Ko, S. H.; Liu, H.; Chen, Y.; Mao, C. DNA Nanotubes as Combinatorial Vehicles for Cellular Delivery. *Biomacromolecules* **2008**, *9* (11), 3039–3043.

(17) Zhu, G.; Hu, R.; Zhao, Z.; Chen, Z.; Zhang, X.; Tan, W. Noncanonical Self-Assembly of Multifunctional DNA Nanoflowers for Biomedical Applications. *J. Am. Chem. Soc.* **2013**, *135* (44), 16438–16445.

(18) Ding, Y.; Jiang, Z.; Saha, K.; Kim, C. S.; Kim, S. T.; Landis, R. F.; Rotello, V. M. Gold Nanoparticles for Nucleic Acid Delivery. *Mol. Ther.* **2014**, *22* (6), 1075–1083.

(19) Yuan, Z.; Chen, Y.-C.; Li, H.-W.; Chang, H.-T. Fluorescent Silver Nanoclusters Stabilized by DNA Scaffolds. *Chem. Commun. (Camb).* **2014**, *50* (69), 9800–9815.

(20) Zheng, J.; Nicovich, P. R.; Dickson, R. M. Highly Fluorescent Noble Metal Quantum Dots. *Annu. Rev. Phys. Chem.* **2008**, *22* (5), 4109.

(21) Chen, L. Y.; Wang, C. W.; Yuan, Z.; Chang, H. T. Fluorescent Gold Nanoclusters: Recent Advances in Sensing and Imaging. *Anal. Chem.* **2015**, *87* (1), 216–229.

(22) Siddik, Z. H. Cisplatin: Mode of Cytotoxic Action and Molecular Basis of Resistance. *Oncogene* **2003**, *22* (47), 7265–7279.

(23) Torchilin, V. Tumor Delivery of Macromolecular Drugs Based on the EPR Effect. *Adv. Drug Deliv. Rev.* **2011**, *63* (3), 131–135.

(24) Giljohann, D. A.; Seferos, D. S.; Patel, P. C.; Millstone, J. E.; Rosi, N. L.; Mirkin, C. A. Oligonucleotide Loading Determines Cellular Uptake of DNA-Modified Gold Nanoparticles. *Nano Lett.* **2007**, *7* (12), 3818–3821.

(25) Karbownik, A.; Szaełk, E.; Urjasz, H.; Gełęboka, A.; Mierzwa, E.; Grzesḱowiak, E. The Physical and Chemical Stability of Cisplatin (Teva) in Concentrate and Diluted in Sodium Chloride 0.9%. *Wspolczesna Onkol.* **2012**, *16* (5), 435–439.

(26) Marullo, R.; Werner, E.; Degtyareva, N.; Moore, B.; Altavilla, G.; Ramalingam, S. S.; Doetsch, P. W. Cisplatin Induces a Mitochondrial-Ros Response That Contributes to Cytotoxicity Depending on Mitochondrial Redox Status and Bioenergetic Functions. *PLoS One* **2013**, *8* (11), 1–15.

CHAPTER 3

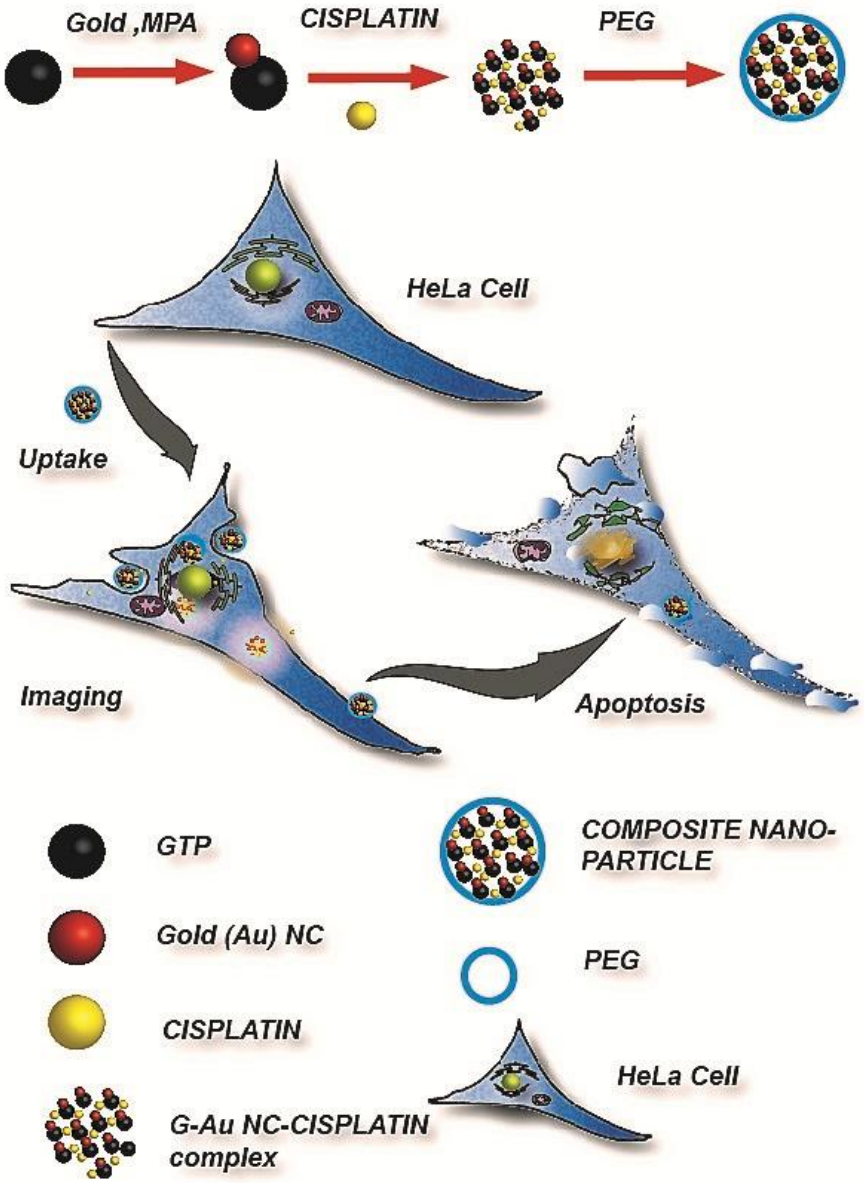

dGTP Templated Luminescent Gold Nanocluster Based Composite Nanoparticles for Cancer Theranostics

B. Chatterjee, A Ghosal, A. Chattopadhyay and S. S. Ghosh, 2018. ACS Biomater. Sci. Eng. 4, 3, 1005-1012. Reproduced by permission of The American chemical Society, Copyright ACS 2018.

ABSTRACT

dGTP templated facile synthesis of luminescent gold nanoclusters (Au NCs) in presence of cisplatin following PEG coating developed spherical composite NPs. The composite NPs delivered cisplatin efficiently into HeLa cells to induce apoptosis mediated cell death and simultaneously bio-imaged the cellular uptake.

dGTP Templated Luminescent Gold Nanocluster Based Composite Nanoparticles for Cancer Theranostics

3.1 Introduction

In the burgeoning field of theranostics, development of smart nanomaterials with concurrent therapeutic and diagnostic functions in a single platform is a great challenge. While the diagnostic moiety can be a fluorophore or a contrasting agent that differentiates the affected cells from the healthy ones, the therapeutic moiety can be small chemicals, drug molecules[1], siRNA[2], peptide or protein[3]. The theranostic agents employ a synergistic approach to reduce uneven biodistribution and their consequent repercussions, if both the functions are performed by separate entities and administered in separate doses. A myriad of nanomaterials has been developed to suit these requisites. The physical properties of these particles are often tailored in terms of shape, size, surface chemistry, optical, magnetic and electronic properties to confirm to a particular requirement, as their physical properties profoundly control their functional aspects[4]. Among them many owing to their design, respond to cues like pH, temperature and magnetic field for specific and controlled payload delivery, reducing the spillage to circumvent associated side effects[5]. Drug carrying capacity of several nanoparticles and imaging capabilities have been well documented[6]. Several inorganic nanoparticles like magnetic nanoparticles, gold nanoparticles, carbon nanotubes, quantum dots act as therapeutic or photothermal agents, and FRET or MRI based materials yield promising results[7]. However, these nanomaterials also have limitations owing to cytoxicity, production costs, enhanced oxidative stress and aberrant activation of cellular complement

system[8]. On the other hand, polymeric nanoparticles like liposomes, dendrimers, and drug polymer conjugates have superior biocompatibility and less inherent cytoxicity. Additionally, they offer an impressive platform for delivering hydrophobic payloads and formulations like doxorubicin liposomes and cytarabine/ daunorubicin liposomes, have already reached clinical trials[9]. However, organic polymers also lack the inherent cellular imaging capability[8] and they need conjugations with imaging moieties for bioimaging. In this context, nanoclusters offer a better biocompatibility as opposed to quantum dots (QDs) and possess enhanced photostability than the organic dyes[10]. Further, the gold nanoclusters in particular have superior biocompatibility, oxidation stability, non-cytotoxicity, and stable fluorescence when compared to silver nanoclusters[11]. Gold nanoclusters (Au NCs) are synthesized on biomolecules like protein, peptides and polynucleotide and subsequently employed for cellular imaging, drug delivery, and measurement of certain substances[12]. However, till date there is no report on unmodified dNTP (deoxy nucleoside triphosphate)-based cluster synthesis. Once synthesized, owing to their inherent biocompatibility, they can readily be used on theranostic platforms. Furthermore, these nucleotides have specific interactions, which then can be exploited for targeting purposes ranging from drug delivery to a plethora of quantitative or qualitative *in vitro* or *in vivo* assays. For instance, these dNTP-based nanoclusters can then act as a carrier for certain DNA intercalating drugs that specifically rely on their interaction with the nucleotides to intercalate within DNA.

Polyethylene glycol (PEG) is known to reduce NP aggregation by augmenting steric distance between two particles and increasing the

hydrophilicity[13]. Moreover, PEG reduces the earmarking of the NPs by opsonin protein and curbs their removal from the circulation by reticuloendothelial system, thus providing them an improved $t_{1/2}$[14]. PEG also acts as functionalization platform for nanoparticles; for instance, targeting moieties attached to it facilitate enhanced and efficient delivery of the NPs into the cells[15]. The imaging property of a theranostic agent is pivotal in discharging its function as it confirms the delivery of the therapeutic payload to the desired site and enables monitoring of the particle movement.

3.2 Outline of the research work

- A facile and quick synthesis method of luminescent gold nanoclusters (Au NCs) on a dNTP (dGTP, in this study) having a quantum yield and photostability suitable for bioimaging applications has been established, making it a potential imaging agent in any theranostic platform.
- Synthesis is facile and reproducible. It takes only 5 min to synthesize luminescent Au NCs and is sans any contamination of SPR active agents.
- The Au NCs were physically characterized with various analytical instruments.
- The established interaction of guanine and cisplatin, have been exploited to form a composite NPs, which were further coated with PEG to yield spherical theranostic NPs. It involves simple and established interaction and is devoid of any intense or consuming step.
- The use of dGTP as a template for the synthesis of gold nanoclusters and its involvement in genesis of composite NPs render the theranostic NPs inherently biocompatible. PEG coating further augments the biocompatibility and imparts

stealth nature on the composite NP, enhancing its potential for clinical translation.

- While the drug component of the composite NPs (cisplatin) exerts the cytotoxic effect, the Au NCs are responsible for biological imaging.

- The physical properties of the composite NPs further accentuate their stealth capabilities and enhance their tumor uptake rate. Charge of the composite NPs reduces their RES and liver uptake rate, and enhances the tumoral uptake rate, which is further complemented by the size of the composite NPs falling in EPR regime.

- Sustained drug release pattern exhibited by the composite NPs offers an added advantage.

- The cytotoxicity of the composite NPs was evaluated with HeLa (human cervical carcinoma) cells. The pronounced cytotoxicity of the composite NPs can be attributed to efficient delivery of the drug to the cells, which is further bolstered by z stacking and confocal microscopy of the composite NPs treated cells. Confocal microscopy of the treated cells also establishes the imaging potential of the composite NPs.

- The composite NPs instigate an enhanced intracellular ROS production, as evidenced by cytometry based DCFHDA assay. This enhanced intracellular ROS level further induces cellular apoptosis, as seen in cytometry based annexin V/PI dual staining assay.

- The competiveness of the composite NPs in inducing apoptosis and carrying out cellular death is further evidenced in cell cycle analysis and FESEM images.

- Overall, the work demonstrates the efficiency of the synthesized dGTP based luminescent Au NCs for their application as an imaging agent in theranostic platforms. We also demonstrate the efficiency of the synthesized composite NP consisting of dGTP, luminescent Au NCs and cisplatin in delivering the drug to cells, their sustained release and imaging capability, broadly as a theranostic agent for cancer treatment.

3.3 Experimental section

3.3.1 *Chemicals:* $HAuCl_4$ (Au, 17 wt % in dilute HCl; 99.99%), mercapto propionic acid (MPA), cis-diamineplatinum (II) dichloride (cisplatin) were obtained from Sigma-Aldrich and used as received, dGTP were procured from Promega, Madison, WI USA (Ref. u1238) and was diluted to desired concentration in autoclaved Mili-Q water, Milli-Q grade water (>18 MΩ cm^{-1}, Millipore) was used in all experiments.

3.3.2 *Synthesis of gold nanoclusters:* 0.05 mM dGTP, 0.52 mM $HAuCl_4$ and 1.92 mM MPA in PBS were briefly heated and then immediately cooled at -20 ^{0}C for 2-3 min, which resulted in the formation of fluorescent gold nanoclusters. However, cooling the solution till it freezes improves the luminescence.

3.3.3 *Synthesis of the composite NPs:* Cisplatin and Au NCs were mixed in a premediated ratio and were incubated at 37 ^{0}C for 4 h. Thereafter, 2 µL of PEG was added to the mixture and subjected to sonication on ice for a

period of 20 min at amplitude of 25 %. This resultant mixture was then kept overnight at shaking condition in dark at 37 ^{0}C. After this, the mixture was centrifuged at 15000 rpm for 20 min. and pellet was re-suspended in a fresh medium.

3.3.4 *Physical Characterization:* UV-vis spectra were measured with PerkinElmer Lambda 25 spectrophotometer. Fluorescence spectra, photostability and quantum yield were measured with Fluorolog-3, Horiba Jobin Edison, NY, USA. Zeta measurements were performed with Malvern Zetasizer. XPS analysis was done with Auger Electron Spectroscopy (AES) Module, Model/Supplier: PHI 5000 Versa Prob II, FEI Inc. Referencing of binding energy was done with C 1s at 284.5 eV.

3.3.5 *Quantum yield measurement:* Quantum yield (QY) of NCs was measured by an established protocol with quinine sulphate (0.10 M in H_2SO_4) solution as the standard. The following equation was used for calculation:

$$Q_{DNA\ NC} = Q_{Ref} \frac{m_{DNA\ NC}}{m_{Ref}} \frac{n_{DNA\ NC}{}^2}{n_{Ref}{}^2}$$

Here Ref stands for standard, Q is quantum yield, m stands for the slope of the plot of integrated fluorescence intensity vs. absorbance and n is for the refractive index (solvent in both cases is water). We used the same solution for UV-vis and fluorescence measurements.

3.3.6 *Zeta measurements:* Each sample was optimally diluted and then zeta potential was measured with Malvern Nano-ZS90.

3.3.7 *MALDI-TOF:* Sample was mixed in 1:1 ratio with 10 mg/ml α-cyano-4-hydroxycinnamic acid (CHCA) matrix, spotted on a MALDI plate, and was analysed with MALDI-TOF (Bruker).

3.3.8 *Fluorescence life time:* Sample was properly diluted and characterized by Picosecond Time-resolved cum Steady State Luminescence Spectrometer, Make: Eddinburg Instruments, Model: FSP920 with a 308 nm LED source.

3.3.9 *Transmission Electron Microscopy (TEM):* Sample was diluted to optimum level and then 7 µL of it was drop-cast over a TEM grid and then allowed to dry overnight. Thereafter studied with JEM 2100; Jeol machine.

3.3.10 *Field emission scanning electron microscopy (FESEM):* Treated cellular samples were trypsinized and were resuspended in 1 ml phosphate buffer saline (PBS). Cells were fixed with chilled 70 % ethanol. 7 µL of the fixed cell suspension was drop-casted on a clean and autoclaved cover slip, and left to air-dry. The samples were double coated with gold before being studied with FESEM (Sigma, Zeiss).

3.3.11 *Atomic force microscopy (AFM):* Composite nanoparticle was diluted optimally and 7 µL of this solution was then drop casted on a cover slip and air dried. The sample was then studied with AFM 5500 series, Agilent.

3.3.12 *Loading efficiency:* The loading efficiency of the composite NPs were calculated using the following formula:

$$\textbf{Loading efficiency} = \frac{\textbf{Total Cisplatin} - \textbf{Cisplatin in supernatant}}{\textbf{Total Cisplatin}}$$

Cisplatin concentration was measured by UV-vis spectrometer at 210 nm.

3.3.13 *Release profile:* Composite NPs were suspended in PBS for different periods of time and after each interval solution was centrifuged and the % of cisplatin released in supernatant was measured with reference to concentration of cisplatin in supernatant at 0 h.

3.3.14 *Confocal microscopy and Z stacking:* For qualitative analysis of cellular uptake of composite NPs, and bioimaging of HeLa cells confocal microscopy (LSM 880, Zeiss) was performed. In this pursuit, HeLa cells were treated with composite NPs for 4 h and observed under the microscope, on excitation with 355 nm laser. For experiments in 4 ^{o}C, cells were pre-incubated at 4 ^{o}C for 20 min. prior to treatment with composite NPs and then were incubated at 4 ^{o}C for further 4 h.

3.3.15 *Mammalian cell culture:* Human cervical cancer cell line (HeLa) was procured from National Centre for Cell Sciences, Pune, India. Cells were maintained in Dulbecco's Modified Eagle's Medium (DMEM) in a 5% carbon dioxide incubator under humid conditions at 37 ^{0}C. DMEM was supplemented with 10% FBS, 100 units/ ml Penicillin, and 100 µg/ ml Streptomycin.

3.3.16 *Cell viability assay by MTT:* In order to conduct cell viability assay, HeLa cells were seeded in a 96-well plate at a density of 7000 cells per well and allowed to attach for 8 h. Thereafter, cells were incubated with NCs, NC-Cis, and composite NPs for 48 h, before MTT assay was done. For this

purpose, MTT (3-(4,5-dimethylthiazol-2-yl)-2,5 diphenyltetrazolium bromide), which is converted to purple formazan by live cells, was added to each well. After solubilizing the formazan crystals in dimethyl sulfoxide, absorbance was determined at 550 nm in a Multiplate Reader (Tecan), with background subtraction at 655 nm. Percentage of viable cells was measured by the formula:

$$\%\ \boldsymbol{of\ cell\ viability} = \frac{(\boldsymbol{A_{550} - A_{655}})\ \boldsymbol{sample}}{(\boldsymbol{A_{550} - A_{655}})\ \boldsymbol{control}} \times \mathbf{100}$$

Here A_{550} denotes absorbance at 550 nm and A_{655} connotes absorbance (background) at 655 nm.

3.3.17 *Cell cycle analysis:* To determine cell cycle arrest of treated cells, if any, flow cytometry based analysis was done with FACS Calibur, BD Biosciences, USA. With this intent, cells were seeded at a density of 1x 10^5 cells per well in a six well plate and treated for 48 h as before. Then cells were harvested by trypsinization and fixed with 70% ethanol at -20 ^{0}C overnight. Thereafter, cells were incubated with 0.2 mg/ ml RNaseA (Amresco) and 10 µg/ ml of propidium iodide (PI), before acquiring in FL2 channel in FACS Calibur.

3.3.18 *Annexin V-FITC/PI:* To detect early and late apoptotic cells, Annexin V-FITC/PI assay was performed. Treatment was done as described before, at the end of which, the assay was performed following manufacturer's protocol. Flow cytometric analysis was done to detect FITC stained cells in the FL1 channel and PI stained cells in the FL2 channel.

3.3.19 *Reactive oxygen species (ROS) generation measurement:* For the purpose of ROS detection in treated HeLa cells, treatment was done for 4 h. Next, the untreated and treated cells were harvested and incubated with 10 µM dichlorofluorescin diacetate (DCFDA) for 30 min, at the end of which flow cytometry based acquisition and analysis was done in FL1 channel.

3.3.20 *Acridine orange (AO)/ Ethidium bromide dual staining:* AO/ EB double staining was performed to detect apoptotic populations in treated HeLa cells. It should be mentioned here that AO is a membrane permeable dye that stains both viable as well as damaged cells, while EB is a membrane impermeable dye that exclusively stains the DNA of membrane compromised/dead cells. Therefore, AO stained cells appear green, EB stained cells (cells devoid of cytoplasm) appear red, and dual stained cells possess green cytoplasm and yellow-orange nuclei. For this purpose, cells were seeded in 96-well plate and treatment was done as mentioned previously. Thereafter, media was replaced with PBS containing 2 µg/ ml AO and 10 µg/ ml and incubated for 5 min, after which images were acquired in epi-fluorescence microscope.

3.4 Results and discussion

Briefly, a mixture of $HAuCl_4$, guanosine 5′-triphosphate (GTP), and mercapto propionic acid (MPA) was heated at 95 ^{0}C for 5 min, and immediately cooled at -20 ^{0}C for 4 min[16]. This yields a clear solution and its UV-vis spectrum was devoid of any peaks in the SPR active region (**Figure 3.1**). This discounts the possibility of any SPR active component i.e. gold nanoparticle, generation during the synthesis. The solution when excited at 330 nm generates bright

orange fluorescence with emission maximum at 590 nm (**Figure 3.2**). This generation of fluorescent entity insinuated the formation of luminescent gold nanoclusters, a notion which was further corroborated with TEM study.

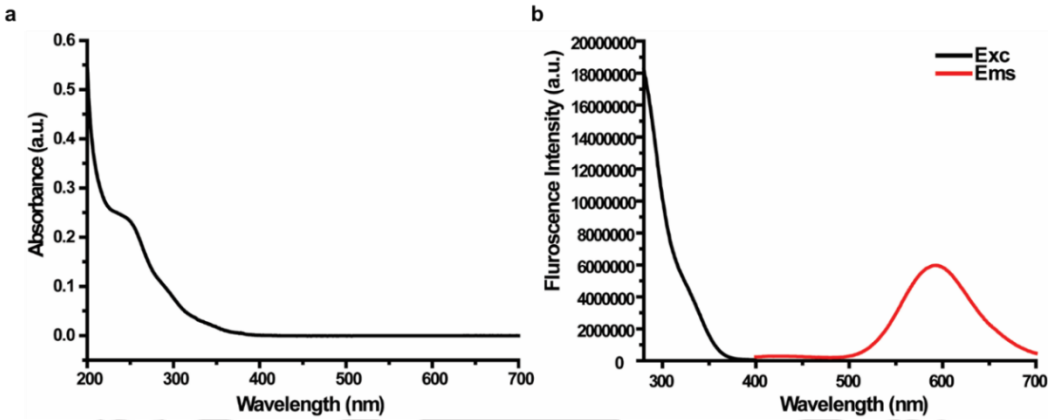

Figure 3.1: a) *UV-vis absorption spectrum of the NCs displaying lack of any SPR peak (400-700 nm). The peak at 270 nm is dues to dGTP and the hump at 330 nm mark the absorption peak of the NCs.* ***b)*** *Excitation and emission spectrum of the NCs marking the 330 nm as the excitation maximum and 590 as an emission maximum.*

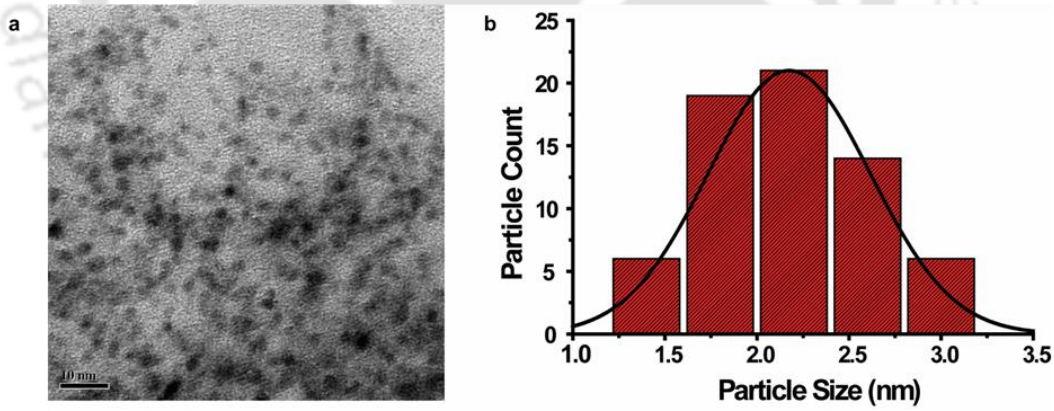

Figure 3.2: a) *TEM image of the dGTP-templated luminescent Au NCs (scale here is 10 nm).* ***b)*** *The average size of the particle was calculated to be 2.05±0.43 nm in the TEM analysis.*

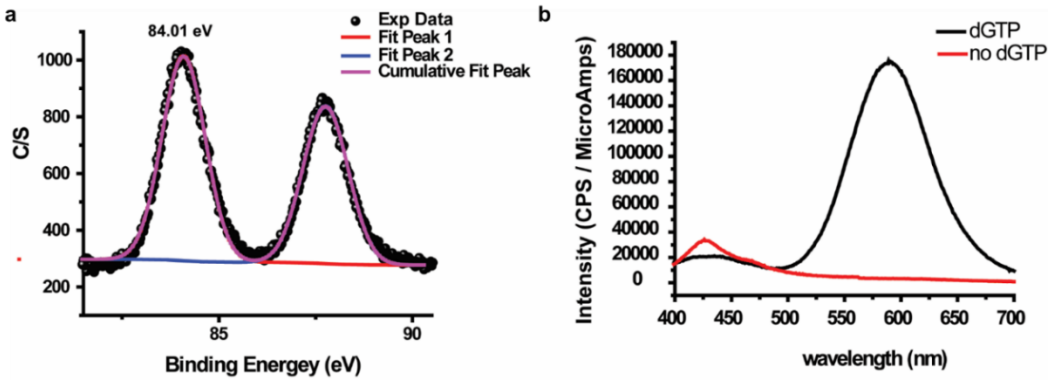

Figure 3.3: a) *XPS spectrum of the NCs displaying the peak at 84.01 eV marking the presence of gold in Au (0) state.* ***b)*** *Templating activity of the dGTP, in the absence of the template the generated fluorescence is not stable and is comparatively very low.*

TEM images (**Figure 3.2 a**) of the solution depicted the presence of ultra-small gold nanoclusters with an average size of 2.05±0.43 nm (**Figure 3.2 b**). Final confirmation regarding the formation of gold nanoclusters comes from the XPS study. It is already reported in the literature that the XPS peaks for Au 4f 7/2 lies between Au (0) state (84 eV) and Au (1) thiolate complex[17]. XPS study of the solution reveals a peak at 84.01 eV (**Figure 3.3 a**), which suggests the Au (0) oxidation state of gold thus, also confirming the formation of the gold nanoclusters[18,19].

It was interesting to note that sans dGTP, with the protocol did not generate any stable fluorescent entity, underlying the importance of the templating activity of the dGTP (**Figure 3.3 b**). The thus synthesised NCs presented an impressive photostability and suffered only 0.28% of loss in fluorescence per min. against 1.27% loss accrued by rhodamine G (**Figure 3.4 a**). NCs also had a quantum yield of 2.16% with quinine sulphate taken as standard (**Figure 3.4 b**). Time-resolved photoluminescence measurements revealed the presence of a single component having a lifetime of 0.53 ns and was

in compliance with the existing literature[11] (**Figure 3.5 a**). MALDI-TOF spectra recorded two prominent peaks, one at 4826.9 Da, corresponding to the species

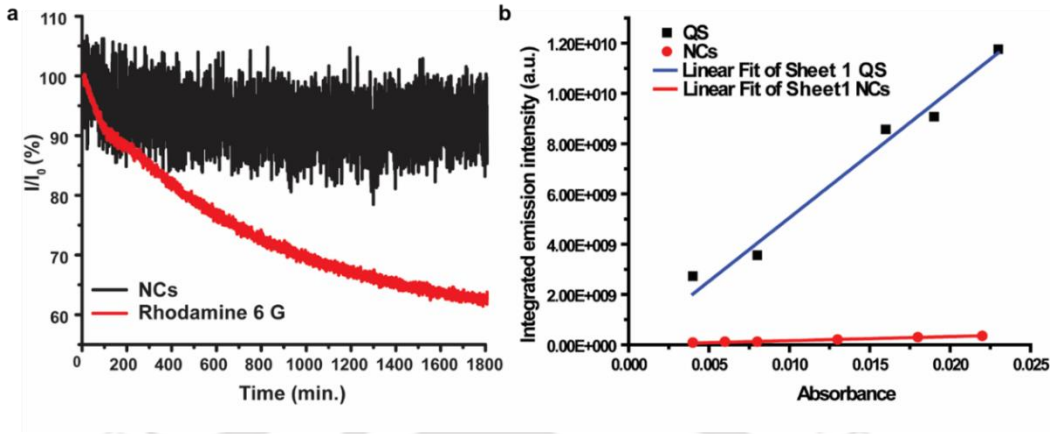

Figure 3.4: a) *Photostability of the NCs was better than Rhodamine 6G.* ***b)*** *Integrated fluorescence intensity vs absorbance plot of NCs and quinine sulphate. Quinine sulphate was used here as a standard and quantum yield of NCs was 2.16%.*

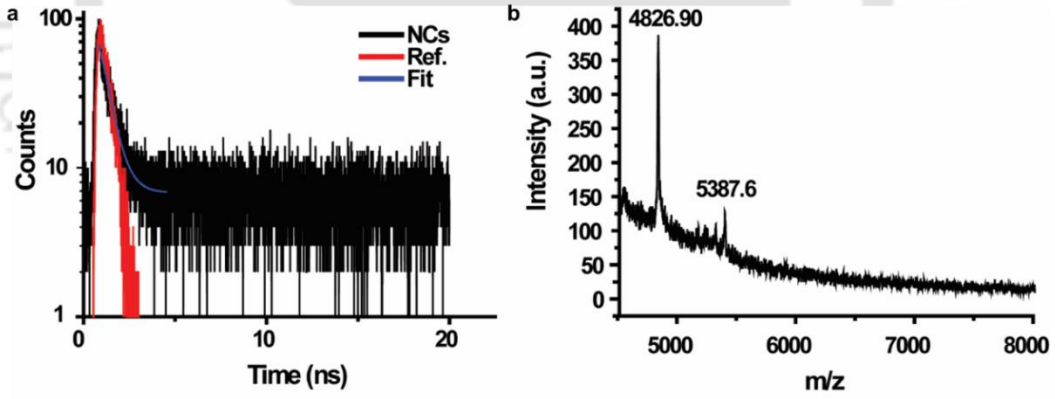

Figure 3.5: a) *The decay profile of the Au NCs.* ***b)*** *MALDI TOF spectrum of the Au NCs displaying two peaks at 4826.9 and 5387.6 corresponding to* $[Au_{18}\ MPA_{12} + Na+ -2H^{+}]^{2-}$ *and* $[Au_{18}\ MPA_{12} +dGTP+ 3Na^{+} -8H^{+}]^{8-}$ *, respectively.*

$[Au_{18}\ MPA_{12} + Na^{+} -2H^{+}]^{2-}$ and another at 5387.6 Da corresponding to $[Au_{18}\ MPA_{12} +dGTP+ 3Na^{+} -8H^{+}]^{8-}$ (**Figure 3.5 b**). Presence of Au_{18} corroborated with the emission profile of the NCs and thus further supported the formation of luminescent NCs. Existing literature insinuates a face fused bi

octahedral Au_9 kernel structure for thiol stabilised Au_{18} clusters where two Au_6 octahedra are fused together by sharing a common Au_3 face[20].

As the affinity and mode of interaction of cisplatin for the purines, guanosine in particular, has already been proven [21], cisplatin and GTP were mixed accordingly, in the ratio of 1:2. This mixture was further incubated at 37 ^{0}C for 4 h, yielding roughly spherical nanoparticles (**Figure 3.6**). Thereafter, 2 µL of PEG was added to the mixture and subjected to sonication on ice for a period of 20 min at amplitude of 25 %. This resultant mixture was then kept overnight at shaking condition in dark at 37 ^{0}C. This ensued the formation of spherical nanoparticles with a diameter of 145±22 nm as revealed by TEM images (**Figure 3.7 a, b**). Formation of these spherical nanoparticles can be attributed to a robust interaction between the individual components, that is, GTP templated Au NCs, cisplatin, and PEG (This insinuates towards a robust interaction between the individual components, that is, dGTP templated Au NCs, cisplatin, and PEG resulting in the formation of spherical nanoparticles). The interaction between the individual components was further illustrated by the

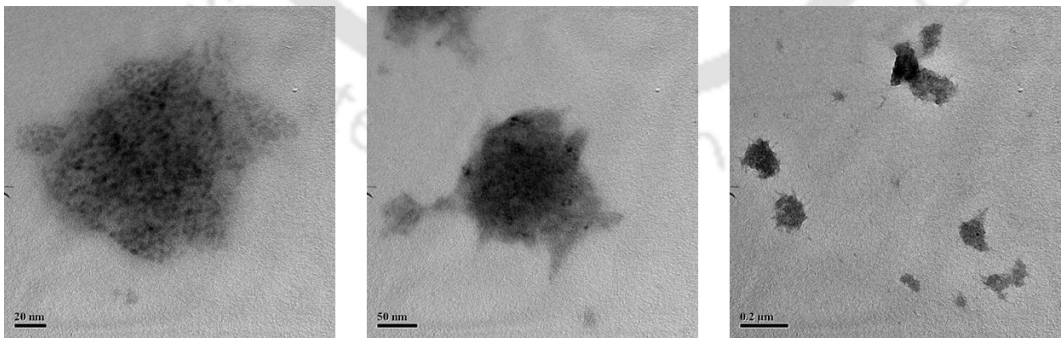

Figure 3.6: *TEM images of the NC-Cisplatin conjugates, depicting a roughly spherical morphology.*

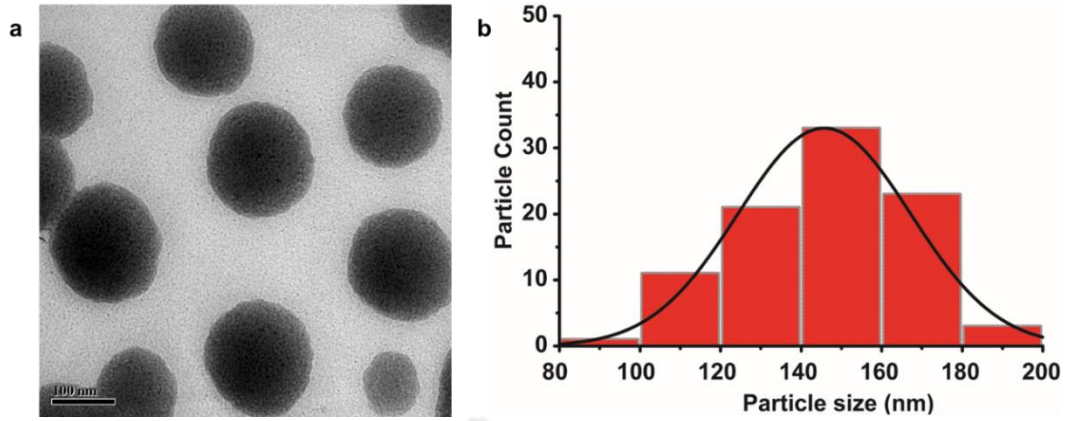

Figure 3.7: a) *TEM image of the composite NPs (scale here is 100 nm)* ***b)*** *Size distribution of the composite NPs as revealed in TEM study. The average size of the composite NPs is 145 ± 22 nm.*

variation in zeta potentials with the successive interaction between the components. While only NCs displayed a zeta potential of -26.3 mV (**Figure 3.8 a**), it changed to -14.1 mV (**Figure 3.8 b**) then it further changed to -1.7 mV (**Figure 3.8 c**) with the addition of PEG. It is interesting to mention here that the slightly negative charge of the composite nanoparticles may marginally reduce the cellular uptake rate, but it could reduce RES and liver uptake, with enhanced the tumour uptake rate[22].

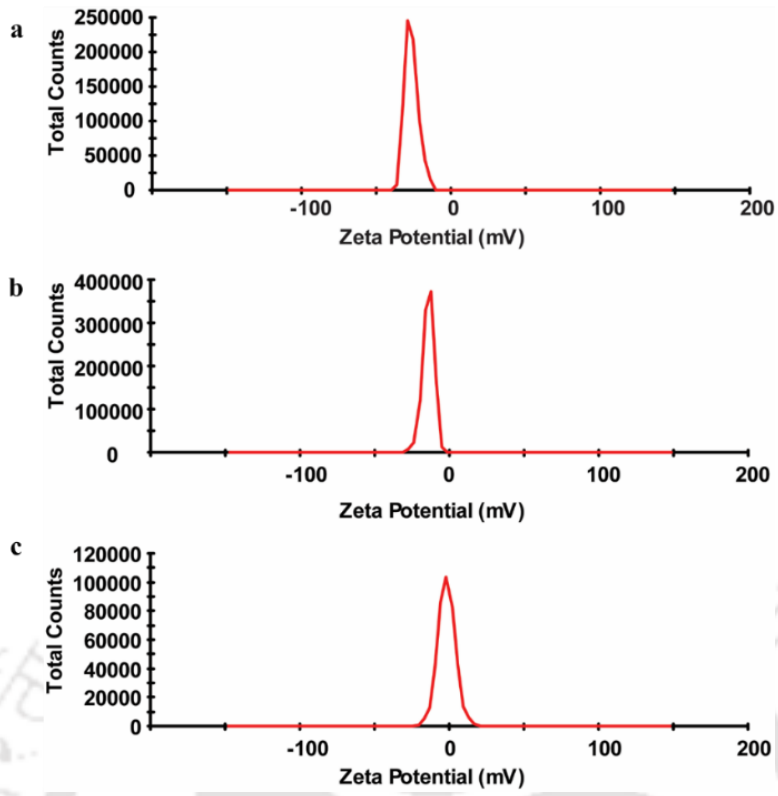

Figure 3.8: *Zeta potential of the* ***a)*** *NCs was -26.3 mV* ***b)*** *NCs-Cisplatin conjugate was -14.1 mV and* ***c)*** *composite NPs was -1.7 mV. The successive change in charge marks the successive interaction between the components.*

TEM study also supported the inclusion of all the components in the composite nanoparticles. Careful examination of the TEM images revealed the film of PEG coating on the composite nanoparticles, and small dark spots in the composite nanoparticles attributed to the nanoclusters. EDX study further approved the observation, as it revealed the presence of both gold and platinum in the composite NPs (**Figure 3.9**). It is important to mention here that although the mixture of only drug and NCs resulted in the formation of small roughly spherical NPs, with the addition of PEG, the geometry of the NPs became more defined and stable, as seen in the TEM images.

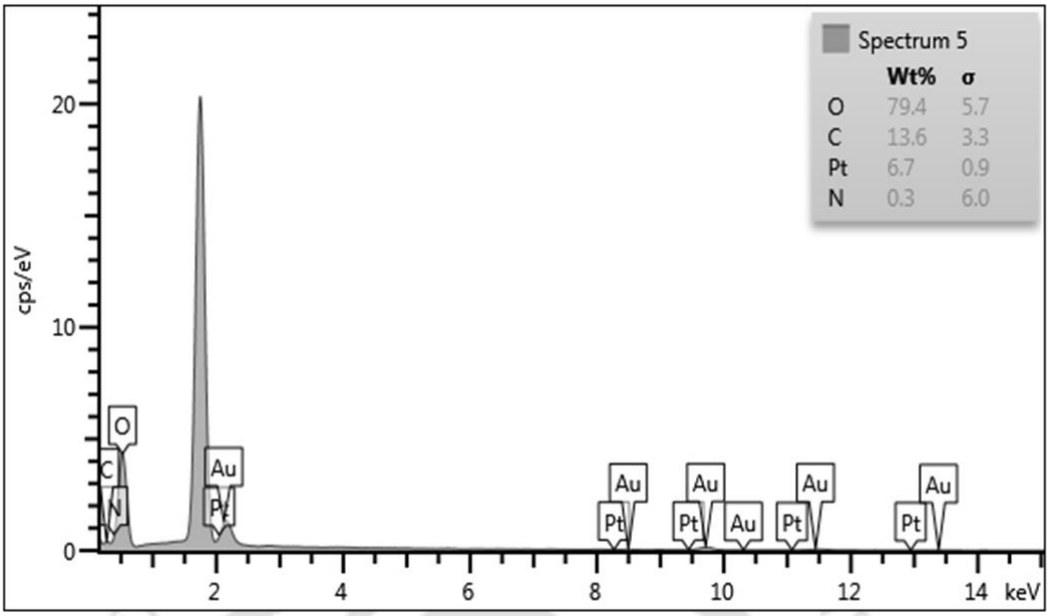

Figure 3.9: *Energy dispersive X-ray (EDX) spectrum of the composite NPs confirms the inclusion of both gold and platinum composite NPs.*

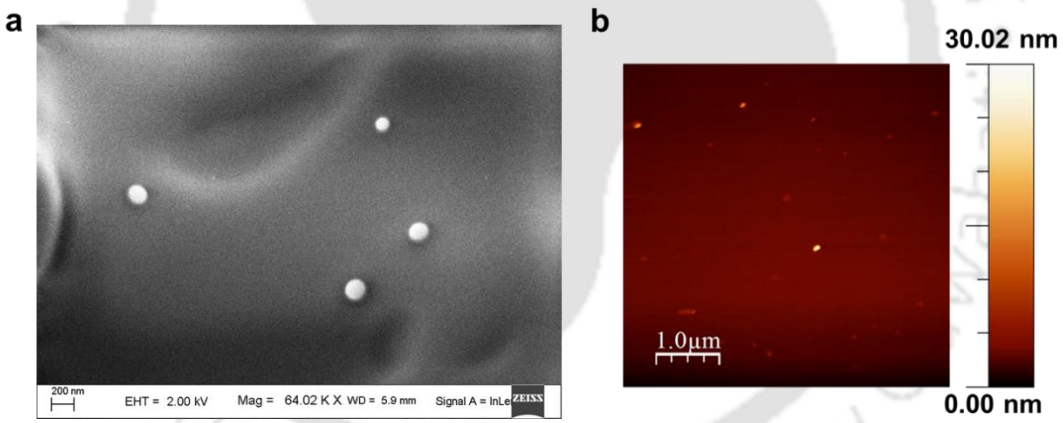

Figure 3.10: a) *FESEM studies corroborate with AFM and TEM studies in supporting the spherical nature of the composite NPs.* ***b)*** *AFM images of the composite NPs displaying spherical morphology and homogenous size distribution (scale here is 1 µm).*

These findings corroborated the FESEM (**Figure 3.10 a**) and AFM studies (**Figure 3.10 b**), as both confirmed the spherical nature of the NPs. The above results also suggested that owing to their size, the composite NPs, even in

absence of any targeting moiety, could exploit the EPR to deliver the drugs into leaky cancer tissues efficiently[23].

The loading efficiency of the composite NPs was determined using UV-vis absorbance spectroscopy and was found to be 40 %. The calculation of loading efficiency has been provided in the experimental section. Confocal microscopy was performed to establish the cellular uptake and imaging capability of the composite NPs. HeLa cells were incubated with the composite NPs for 4 h at 37 ^{0}C and then were examined with confocal microscopy. In contrast to the control cells (**Figure 3.11 a, b**) the composite NPs treated cells exhibited a bright yellow fluorescence. This fluorescence can be attributed to the embedded Au NCs, verifying the uptake of the NPs and its imaging competence (**Figure 3.11 c, d**). The uptake was further verified by Z-stacking of the acquired image, as it clearly indicated that the source of fluorescence, the Au NCs, was inside the cells (**Figure 3.11 e**). The size of the nanoparticles insinuated an endocytosis-mediated cellular uptake, which was partially supported by confocal studies of cellular uptake of the composite NPs at 4 ^{o}C. At this temperature, cells lose their plasma membrane fluidity and any kind of cellular traffic gets remarkably blocked[24]. Cells kept at 4 ^{o}C displayed no fluorescence from inside the cells during confocal imaging and Z stacking studies, suggesting to a reduced uptake of the composite NPs at 4 ^{o}C (**Figure 3.12**). The size of the nanoparticles insinuated an endocytosis-mediated cellular uptake; however, the detailed uptake mechanism needs further investigation. This swift and facile uptake of the NPs can be attributed to the compact nature of NPs, their size, and slightly positive charge, all of which can facilitate their uptake[4].

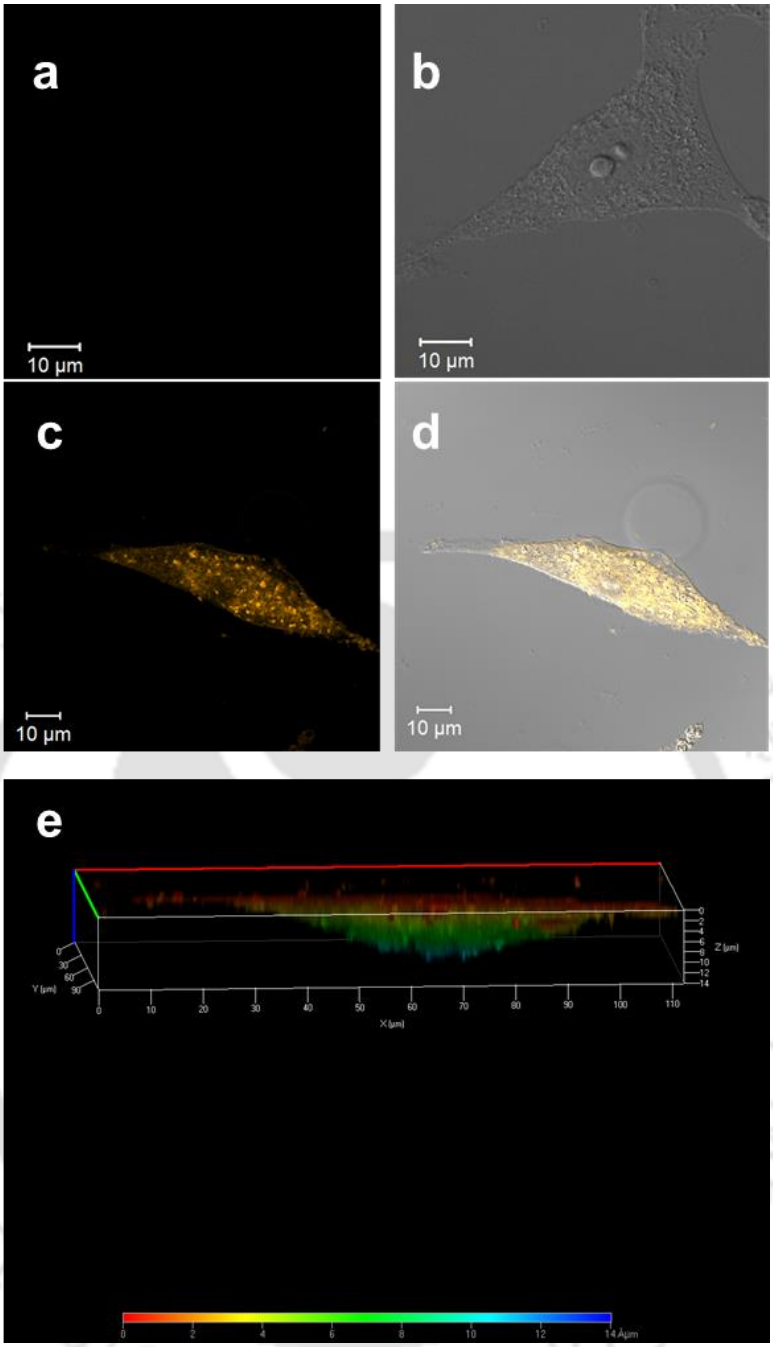

Figure 3.11: *Cellular uptake and cytotoxicity: Confocal image of the control Hela cells displaying no fluorescence, both in* ***a)*** *and* ***b)*** *representing the fluorescent and the merged image, respectively. The composite NP- treated HeLa cells displayed a bright yellow luminescence confirming the cellular uptake of the composite NPs, both in* ***c)*** *and* ***d)*** *representing the fluorescent and merged image respectively.* ***e)*** *Confocal 3D projection of 14 µm Z-stack of the same cell (NP treated cell), verifying the uptake of the composite NPs in the cells. Here the false colours depict the distance from coverslip to slide (0-14 µm), with red denoting species closest to coverslip (top of cells) and blue being bordering the slide (bottom of cells, outside the cellular surface). The cell however displays a green fluorescence which came from the*

uptaken composite NPs, as green particle represents species that are equidistant from slide and coverslip, hence, inside the cell.

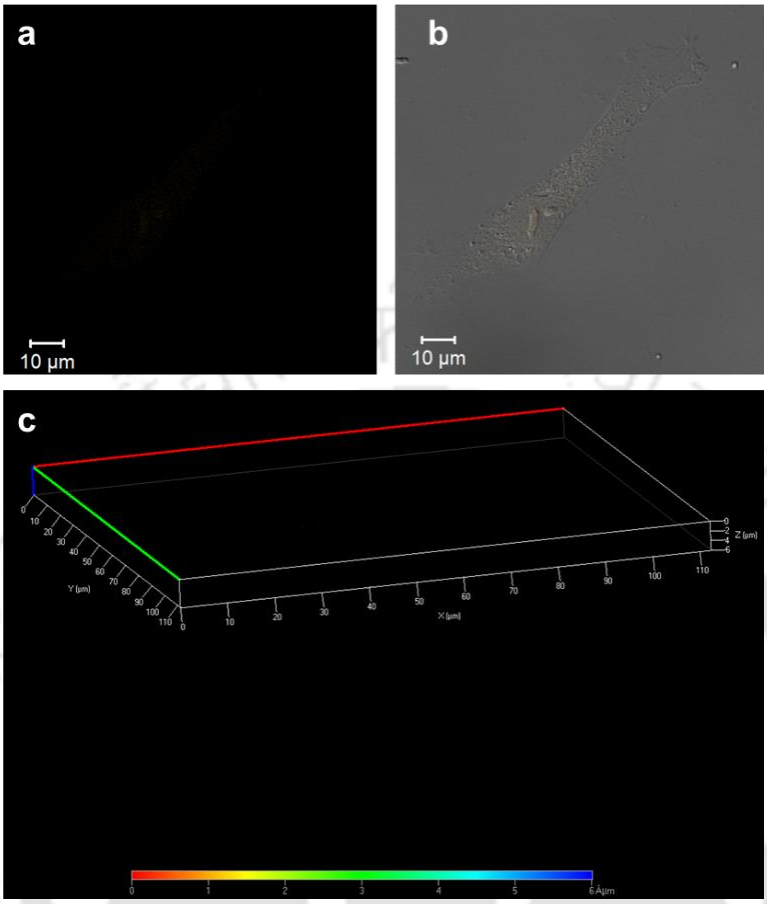

Figure 3.12: *Confocal imaging of HeLa cells treated with the composite NPs for 4 h at 4 °C* ***a)*** *fluorescent image of the cells displaying no fluorescence* ***b)*** *merged image of the treated HeLa cells displaying no fluorescence* ***c)*** *confocal 3D projection of 6 µm Z-stack (same cell), displaying no fluorescence from inside the cells.*

The release profile of cisplatin from the composite NPs was evaluated at physiological pH (7.4). The composite NPs exhibited a sustained release of cisplatin at physiological pH (7.4) at 37 ^{0}C after 24 h. However, the composite NPs displayed an initial burst of cisplatin release, which resulted in the release of 12 % of cisplatin into the medium in the first 2 h. The release continued until 6 h, releasing 40% of the cisplatin content. Thereafter a sustained release of cisplatin

followed until 60 h decimating 66% of the cisplatin in the medium (**Figure 3.13 a**).

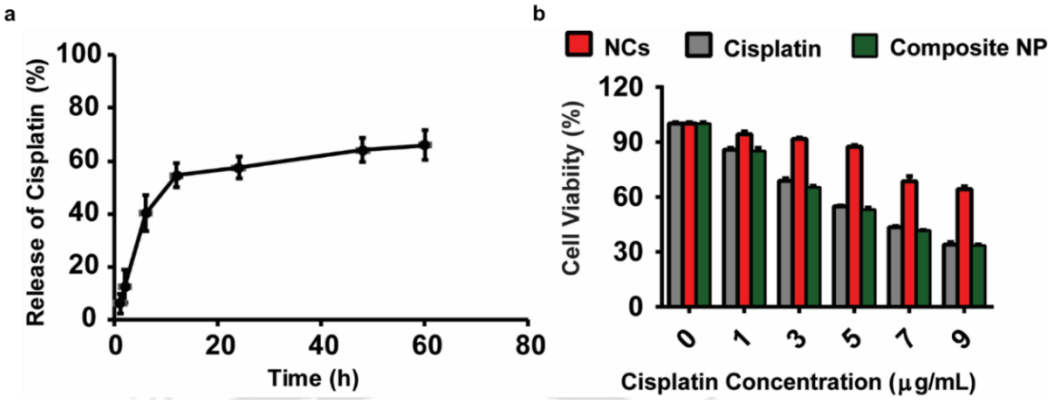

Figure 3.13: *Release and Cellular toxicity assays.* ***a)*** *Release profile of the drug from the composite NPs displaying initial outburst until 6 h and sustained release until 60 h.* ***b)*** *MTT assay of the composite NPs showing higher cytotoxicity than NCs.*

To evaluate the drug delivery aptitude and cytotoxicity of the composite NPs, we conducted 3- (4, 5-dimethylthiazol-2-yl)-2, 5-diphenyltetrazolium bromide (MTT) assay (a cell viability assay). The cells were treated for 48 h with composite NPs, free drug, and NCs. The results illustrated the low cytotoxicity of the NCs itself and similar cytotoxicity of the composite NPs and the free drug. The IC_{50} value for the composite NP-treated cells was 4.4 µg/ ml and the free drug was at 4.5 µg/ ml (**Figure 3.13 b**). Similar cytotoxicity profile of the composite NPs and the free drug can be attributed to the PEG coating. This ensured slow but sustained drug release from the composite NPs, thus limiting the amount of available cisplatin to act at an early hour. However, the PEG coating provides a stealth nature and opens the prospect of further functionalization of the composite NPs depending on the necessities. The MTT results also established the stability of the drug in the composite NPs, as it evidently retained its functionality (cytotoxicity). Further vindication of the

notion that these NPs delivered the drug successfully came from the cell cycle analysis. The cells were treated for 48 h with the free drug and the composite NPs at their respective IC_{50} concentrations, and then were subjected to flow cytometry analysis following propidium iodide staining. The results presented a similar profile for both the free drug and the composite NPs, charting 6.46 % and 6.66 % sub-G_0/G_1 population, respectively, which are considerably higher than the 0.63 % and 1.3 % of the control and the only NC-treated cells, respectively (**Figure 3.14 a**). The observations corroborated the results obtained in the MTT assay and supported the notion of successful delivery of the drug followed by cell death.

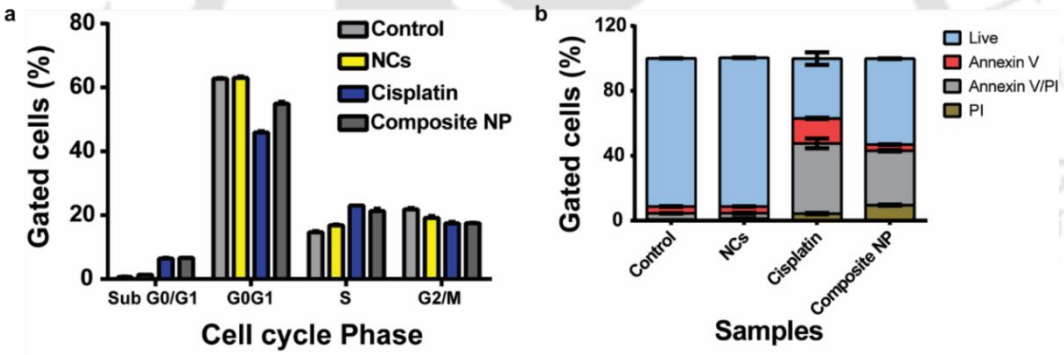

Figure 3.14: a) *Cell cycle analysis with PI, displayed higher cellular death with composite NPs than NCs.* ***b)*** *Annexin V/PI dual staining study indicates an apoptosis mediated death is induced by composite NPs and the cytoxicity of the composite NPs is higher than NCs.*

Cisplatin is a conventional anticancer drug, which is known to induce apoptosis by causing DNA damage [25]. To understand the mechanism of cell death in the current context, we treated the cells with cisplatin, NCs, and the composite NPs for 48 h. After treatment, cells were stained with FITC labelled Annexin V and counter-stained with PI, and finally subjected to flow cytometry analysis. It is relevant to mention here that the inception of the apoptosis is

marked by flipping of the cell membrane, exposing the attached phosphatidylserine to the external environment, which can then bind to FITC labelled Annexin V[26]. On the other hand, only the compromised plasma membrane, a feature of late apoptotic or dead cells, allows the cellular influx of PI. Therefore, cells that have taken either dye or both dyes represent the apoptotic population. Cells treated with drug and the composite NPs both displayed around 38% of double stained population and against roughly 5% population in control (5.2 %) and NCs (4.9 %) (**Figure 3.14 b**). These results suggest an apoptosis mediated cell death. Interestingly, the composite NPs and

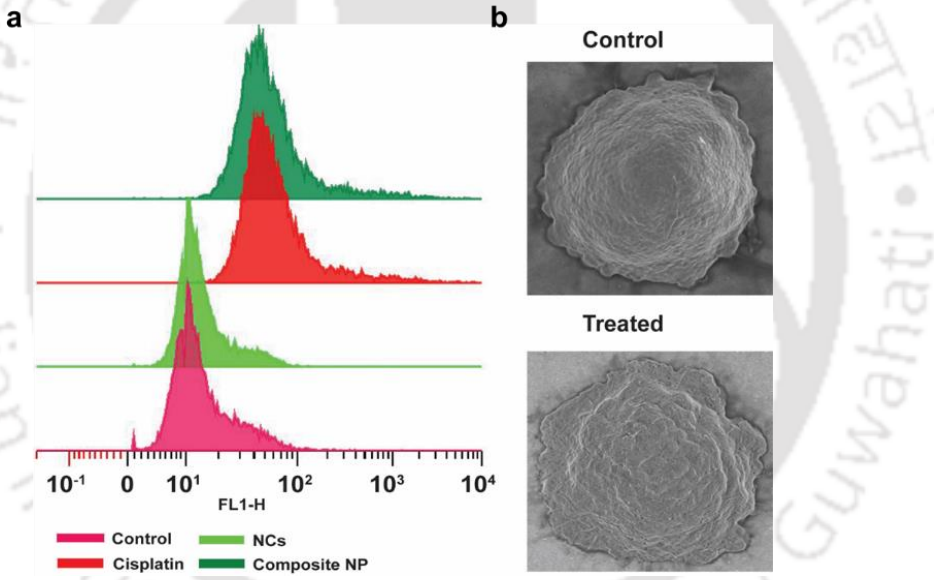

Figure 3.15: a) *ROS study indicates higher ROS generation in drug and the composite NPs treated cells than NCs treated cells.* ***b)*** *Control cells display no signs apoptosis while the composite NPs treated cells display membrane blebbing a sign of apoptosis.*

cisplatin both induced considerably higher ROS levels when compared with the NCs and control, as measured by flow cytometry (**Figure 3.15 a**). These enhanced ROS levels usually lead to mitochondria directed apoptosis [27], and cisplatin is also reported to generate ROS[28]. These experiments further indicated

an apoptotic cell death. These results were in compliance with the FESEM study, where the cellular samples treated with the composite NPs showed membrane blebbing and apoptotic bodies, while the control samples had kenspeckle absenteeism of these features (**Figure 3.15 b**). Visual corroboration of this mode of cell death was further provided by acridine orange (AO)/ ethidium bromide (EB) dual staining (**Figure 3.16**), which exhibited more population of dual stained cells (indicating apoptosis) in the composite NP-treated populations than NCs treated population.

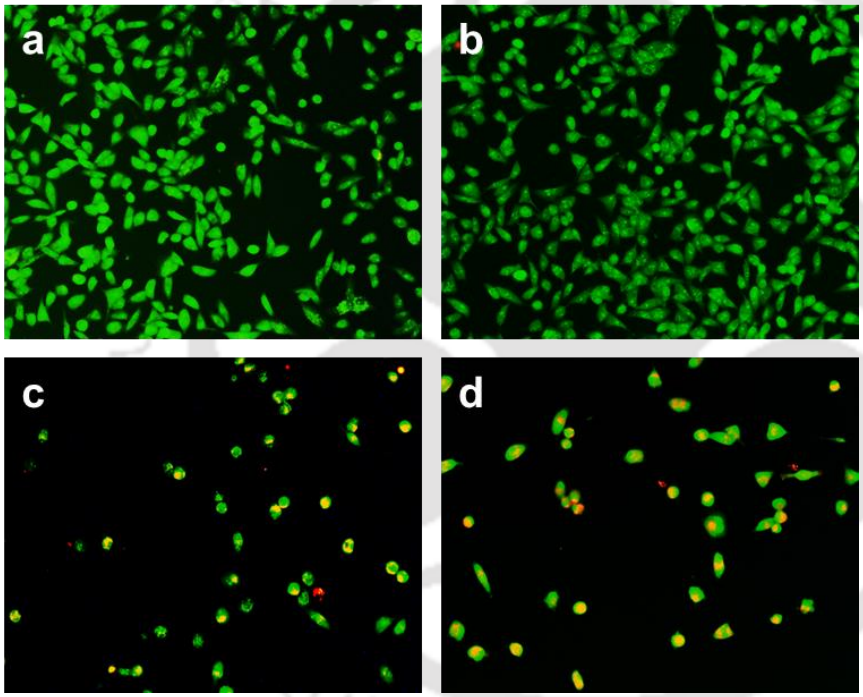

Figure 3.16: *Dual AO/EB Staining of HeLa cells after treatment with* ***a)*** *Control cells* ***b)*** *NCs* ***c)*** *Cisplatin* ***d)*** *Composite NPs. Here the red cells indicate the dead cells while the green cells indicate the live cells.*

3.5 Conclusions

In essence, luminescent Au NCs, have been synthesized where unique binding property of cisplatin with dGTP was exploited to form the roughly spherical composites. Further PEG coating provided spherical smoothness with EPR favourable sized composite NPs, exhibiting characteristic slow release of cisplatin. These biocompatible nanoclusters were employed for cellular imaging and therapy. *In vitro* cellular imaging confirmed delivery of these theranostic NPs into HeLa cells, possibly by endocytosis. This results in the consequent apoptotic cell death of the host cells. Because of these remarkable imaging properties and anti-cancer effects, this theranostic composite NP holds immense potential for its future clinical translation.

3.6 References

(1) Feng, T.; Ai, X.; An, G.; Yang, P.; Zhao, Y. Charge-Convertible Carbon Dots for Imaging-Guided Drug Delivery with Enhanced in Vivo Cancer Therapeutic Efficiency. *ACS Nano* **2016**, *10*, 4410–4420.

(2) Lee, S.-Y.; Yang, C.-Y.; Peng, C.-L.; Wei, M.-F.; Chen, K.-C.; Yao, C.-J.; Shieh, M.-J. A Theranostic Micelleplex Co-Delivering SN-38 and VEGF siRNA for Colorectal Cancer Therapy. *Biomaterials* **2016**, *86*, 92–105.

(3) Kempen, P. J.; Greasley, S.; Parker, K. A.; Campbell, J. L.; Chang, H. Y.; Jones, J. R.; Sinclair, R.; Gambhir, S. S.; Jokerst, J. V. Theranostic Mesoporous Silica Nanoparticles Biodegrade after pro-Survival Drug Delivery and Ultrasound/magnetic Resonance Imaging of Stem Cells. *Theranostics* **2015**, *5* (6), 631–642.

(4) Albanese, A.; Tang, P. S.; Chan, W. C. W. The Effect of Nanoparticle Size, Shape, and Surface Chemistry on Biological Systems. *Annu. Rev. Biomed. Eng.* **2012**, *14* (1), 1–16.

(5) Mura, S.; Nicolas, J.; Couvreur, P. Stimuli-Responsive Nanocarriers for Drug Delivery. *Nat. Mater.* **2013**, *12* (11), 991–1003.

(6) Bao, G.; Mitragotri, S.; Tong, S. Multifunctional Nanoparticles for Drug Delivery and Molecular Imaging. *Annu. Rev. Biomed. Eng.* **2013**, *15*, 253–282.

(7) Lim, E.; Kim, T.; Paik, S.; Haam, S.; Huh, Y.; Lee, K. Nanomaterials for Theranostics : Recent Advances and Future Challenges. *ACS Chem. Rev.* **2015**, *115* (1), 327–394.

(8) Naahidi, S.; Jafari, M.; Edalat, F.; Raymond, K.; Khademhosseini, A.; Chen, P. Biocompatibility of Engineered Nanoparticles for Drug Delivery. *J. Control. Release* **2013**, *166* (2), 182–194.

(9) Peng, H.; Liu, X.; Wang, G.; Li, M.; Bratlie, K. M.; Cochran, E.; Wang, Q. Polymeric Multifunctional Nanomaterials for Theranostics. *J. Mater. Chem. B* **2015**, *3* (34), 6856–6870.

(10) Luo, Z.; Zheng, K.; Xie, J. Engineering Ultrasmall Water-Soluble Gold and Silver Nanoclusters for Biomedical Applications. *ChemComm* **2014**, *50*, 5143–5155.

(11) Venkatesh, V.; Shukla, A.; Sivakumar, S.; Verma, S. Purine-Stabilized Green Fluorescent Gold Nanoclusters for Cell Nuclei Imaging Applications. *ACS Appl. Mater. Interfaces* **2014**, *6* (3), 2185–2191.

(12) Chen, L. Y.; Wang, C. W.; Yuan, Z.; Chang, H. T. Fluorescent Gold Nanoclusters: Recent Advances in Sensing and Imaging. *Anal. Chem.* **2015**, *87* (1), 216–229.

(13) Jokerst, J. V; Lobovkina, T.; Zare, R. N.; Gambhir, S. S. Nanoparticle PEGylation for Imaging and Therapy. *Nanomedicine (Lond).* **2011**, *6* (4), 715–728.

(14) Pelaz, B.; Maffre, P.; Hartmann, R.; Gallego, M.; Fuente, J. M. De; Nienhaus, G. U.; Parak, W. J.; Rivera-ferna, S. Surface Functionalization of Nanoparticles with Polyethylene Glycol : E Ff Ects on Protein Adsorption and Cellular Uptake. *ACS Nano* **2015**, *9* (7), 6996–7008.

(15) Dhar, S.; Gu, F. X.; Langer, R.; Farokhzad, O. C.; Lippard, S. J. Targeted Delivery of Cisplatin to Prostate Cancer Cells by Aptamer Functionalized Pt(IV) Prodrug-PLGA-PEG Nanoparticles. *Proc. Natl. Acad. Sci. U. S. A.* **2008**, *105* (45), 17356–17361.

(16) Chatterjee, B.; Sahoo, A. K.; Ghosh, S. S.; Chattopadhyay, A. Interactive Luminescent Gold Nanocluster Embedded dsDNA and Cisplatin as Model Nanoparticles for Cancer Theranostics. *RSC Adv.* **2016**, *6* (114), 113053–113057.

(17) Kawasaki, H.; Hamaguchi, K.; Osaka, I.; Arakawa, R. Ph-Dependent Synthesis of Pepsin-Mediated Gold Nanoclusters with Blue Green and Red Fluorescent Emission. *Adv. Funct. Mater.* **2011**, *21* (18), 3508–3515.

(18) Govindaraju, S.; Ankireddy, S. R.; Viswanath, B.; Kim, J.; Yun, K. Fluorescent Gold Nanoclusters for Selective Detection of Dopamine in Cerebrospinal Fluid.

Sci. Rep. **2017**, *7*, 40298.

(19) Xie, J.; Zheng, Y.; Ying, J. Y. Protein-Directed Synthesis of Highly Fluorescent Gold Nanoclusters. *J. Am. Chem. Soc.* **2009**, *131* (3), 888–889.

(20) Das, A.; Liu, C.; Byun, H. Y.; Nobusada, K.; Zhao, S.; Rosi, N.; Jin, R. Structure Determination of [Au18(SR)14]. *Angew. Chemie - Int. Ed.* **2015**, *54* (10), 3140–3144.

(21) Baik, M. H.; Friesner, R. A.; Lippard, S. J. Theoretical Study of Cisplatin Binding to Purine Bases: Why Does Cisplatin Prefer Guanine over Adenine? *J. Am. Chem. Soc.* **2003**, *125* (46), 14082–14092.

(22) Xiao, K.; Li, Y.; Luo, J.; Lee, J. S.; Xiao, W.; Gonik, A. M.; Agarwal, R. G.; Lam, K. S. The Effect of Surface Charge on in Vivo Biodistribution of PEG-Oligocholic Acid Based Micellar Nanoparticles. *Biomaterials* **2011**, *32* (13), 3435–3446.

(23) Torchilin, V. Tumor Delivery of Macromolecular Drugs Based on the EPR Effect. *Adv. Drug Deliv. Rev.* **2011**, *63* (3), 131–135.

(24) Luo, Y. C.; Teng, Z.; Wang, T. T. Y.; Wang, Q. Cellular Uptake and Transport of Zein Nanoparticles: Effects of Sodium Caseinate. *J. Agric. Food Chem.* **2013**, *61* (31), 7621–7629.

(25) Siddik, Z. H. Cisplatin: Mode of Cytotoxic Action and Molecular Basis of Resistance. *Oncogene* **2003**, *22* (47), 7265–7279.

(26) Zhang, G.; Gurtu, V.; Kain, S. R.; Yan, G. Early Detection of Apoptosis Using a Fluorescent Conjugate of Annexin V. *Biotechniques* **1997**, *23* (3), 525–531.

(27) Simon, H. U.; Haj-Yehia, A.; Levi-Schaffer, F. Role of Reactive Oxygen Species (ROS) in Apoptosis Induction. *Apoptosis* **2000**, *5* (5), 415–418.

(28) Marullo, R.; Werner, E.; Degtyareva, N.; Moore, B.; Altavilla, G.; Ramalingam, S. S.; Doetsch, P. W. Cisplatin Induces a Mitochondrial-Ros Response That Contributes to Cytotoxicity Depending on Mitochondrial Redox Status and Bioenergetic Functions. *PLoS One* **2013**, *8* (11), 1–15.

Chapter 4

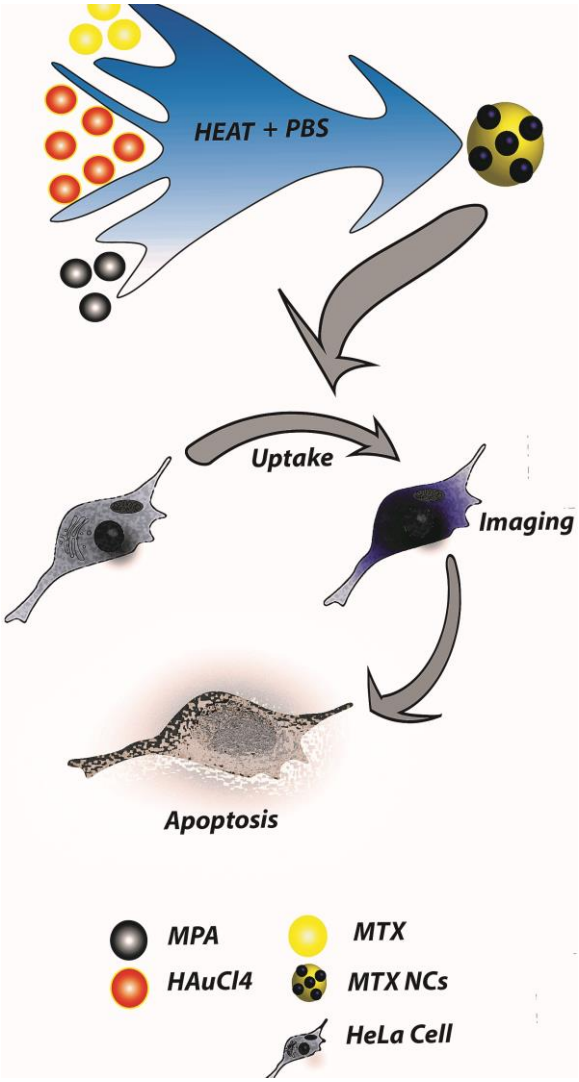

Developing single entity theranostic: Drug based fluorescent nanoclusters with augmented cytotoxicity.

Bandhan Chatterjee, Asif Raza, and Siddhartha Sankar Ghosh.

ABSTRACT

Methotrexate (MTX) templated luminescent gold nanoclusters were synthesized as a single unit nanotheranostic. These luminescent gold nanoclusters when excited display a bright blue fluorescence and have high photostability and decent quantum yield. These nanoclusters also display robust stability in both PBS and serum, which marks its potential for *in vivo* application. The nanoclusters also have an enhanced cytotoxicity over the parent drug with an IC_{50} value of 98 ng/ mL against 188 ng/ mL of the later. Thus, with additional capability of bioimaging and augmented cytotoxicity they may act as superior alternative to the parent drug.

Developing Single Entity Theranostic: Drug Based Fluorescent Nanoclusters with Augmented Cytotoxicity

4.1 Introduction

Theranostics or nanotheranostics is simply an amalgamation of a therapeutic and a diagnostics moiety into a single module[1]. It garnered widespread attention following the gradual unraveling of complexities associated with the conventional treatments and simultaneous rise of plethora of nanomaterials that provides ailment to many of these complexities [2]. Issues like uneven biodistribution, lack of specific targeting, lack of traceability to name a few, has been resolved with various nanoplatforms. For instance, various polymeric nanoparticles were tailored into drug delivery vehicles (DDVs) to deliver drug payload into the cells[3]. Things appeared even brighter with the development of various non-invasive diagnostic platforms like magnetic nanoparticles[4] or fluorescent nanomaterials (quantum dots and metal nanoclusters) [5]. These imaging moieties can be loaded along the conventional drugs into various drug delivery vehicles (DDVs) developing multicomponent theranostics, where nanoparticles can deliver the drug payload in a targeted manner with proper functionalization, which can also be monitored in real time[6,7]. Integrating various components can be sometime difficult and have to rely on certain combinations, which can interact in a stable manner, fueling the need of single component theranostics.

However, integrating two properties *viz* therapeutic and imaging potential into a single entity remains a challenge for the development of single unit theranostic agents. We have conventional drugs that are very effective in treatment, but the majority of drug does not have an inherent imaging potential. Therefore, we have to tag it with some imaging moiety to serve the purpose. However, drugs like doxorubicin are an

exception to this as they have an inherent fluorescence. This fluorescence can be utilized to confirm loading of the drug into the DDV[8] or the uptake of the theranostic into the cells or bioimaging of the cells[9] or tracking its movement through a system. However, none of these facilities are available with non-fluorescent drugs and they need a separate moiety to be loaded along with them in DDVs. One alternative to this is to make the drug itself fluorescent and then use it as a substitute to the parental drug. Now, this fluorescent drug can act as bi- functional moiety that can be administrated as single unit theranostic or can be loaded into DDVs, tailored to requisite.

Synthesizing nanoclusters on traditional drugs can be an option to make fluorescent drugs. Nanoclusters are essentially sub 2 nm sized particles that sports a strong quantum confinement effect for its free electrons, which leads to discretization of the energy levels from continuous bands generating size depending fluorescence and other molecules like properties[10]. Among the various metal nanoclusters gold nanoclusters (Au NCs) are favored more over their other counterparts.[11] Au NCs are highly fluorescent, photostable, biocompatible and have been used for bioimaging in various theranostic platforms[12]. Au NCs are also been synthesized on various templates including small organic templates, but the procedure remains tardy and arduous [13].

4.2 Outline of the research work

- A simple and quick synthesis of a luminescent gold nanoclusters using methotrexate as a template was established. These synthesized methotrexate templated gold nanoclusters (MTX NCs) at one hand were brightly fluorescent, have good quantum yield and photostability rendering it a suitable imaging moiety for various theranostic platforms. On the other hand, it displayed an

augmented cytotoxicity than the free drug. In effect, coalescing two separate functional units into a single unit.

- Special attention must be paid at the utility of these ultra-small units as traditional theranostics are very large compared to these units. As size remains an issue for the free movement of the theranostic in various models, this size must be considered as a huge advantage.

- Synthesis of the MTX NCs is facile and swift as it only takes 3 min of heating. The synthesis is artless, highly reproducible and yield nanoclusters sans any SPR active entity contamination.

- Physical characterization confirms the formation of the ultra-small gold nanoclusters. Other physical properties were established using various analytical instruments.

- The MTX NCs displayed an impressive stability both in PBS and serum, one of the prime requisite of a theranostic, instantiating the plausibility of its *in vivo* use as a theranostic.

- The cytoxicity of the MTX NCs were assessed on HeLa (human cervical carcinoma) cells using a cell viability assay. The assay established the superior cytoxicity of the MTX NCs over the free drug.

- The influx of the MTX NCs into the cellular system was measured using flow cytometry and confocal microscopy. Once inside these luminescent entities enabled confocal microscopy mediated cellular imaging of the host cells.

- It was further observed that the MTX NCs raised the intracellular ROS as confirmed by flow cytometry based DCFHDA assay, leading the cell to an apoptosis mediated cell death. This observation was further substantiated with flow cytometry based Annexin V/ PE dual staining assay.

4.3 Experimental section

4.3.1 *Chemicals:* $HAuCl_4$ (Au, 17 wt % in dilute HCl; 99.99%), mercapto propionic acid (MPA), methotrexate hydrate, chitosan (viscosity averaged molecular weight, Mv, 672 kDa, and degree of deacetylation >75%), folic acid, and sodium tripolyphosphate (TPP) were obtained from Sigma-Aldrich and used as received. Milli-Q grade water (>18 MΩ cm^{-1}, Millipore) was used in all experiments.

4.3.2 *Synthesis of MTX NCs:* 20 µL of MTX (0.45 mg/ mL), 6 µL of 10 mM of $HAuCl_4$ and 2 µL of 11 M MPA were dissolved in 150 µL of PBS (1 X) and heated at 80 ^{0}C for 3 min., this yields the clear solution of luminescent MTX NCs.

4.3.3 *Characterizations:* UV-visible spectra were measured with PerkinElmer Lambda 25 spectrophotometer. Fluorescence spectra, photostability and quantum yield were measured with Fluorolog −3, Horiba Jobin Edison, NY, USA. Zeta measurements were performed with Malvern Zetasizer. Fluorescence lifetime was measured using Picosecond Time-resolved cum Steady State Luminescence Spectrometer, Make: Eddinburg Instruments, Model: FSP920 with a 355 nm LED source. XPS analysis was done with Auger Electron Spectroscopy (AES) Module, Model/Supplier:PHI 5000 Versa Prob II,FEI Inc. Referencing of binding energy was done with C 1s at

284.5 eV. Mass spectra analysis was done with MALDI-TOF (Bruker) with 10 mg/ml α-cyano-4-hydroxycinnamic acid (CHCA) matrix. TEM analysis and EDX analysis was done with JEM 2100; Jeol machine.

4.3.4 *Cellular assays:* All cellular assay were carried out on human cervical cancer cell line (HeLa) and were procured from National Centre for Cell Sciences, Pune, India. HeLa cells were cultured in Dulbecco's Modified Eagle's Medium (DMEM) supplemented with 10% FBS, 100 units/ ml Penicillin, and 100 µg/ ml Streptomycin and were incubated at 37 ^{0}C for 12 h under humid conditions with 5% CO_2 for attachment conditions prior to any treatment.

4.3.5 *Cellular imaging and Z stacking:* HeLa cells were treated with MTX NCs, MTX and NPs for respective experiments for 4 h at 37 ^{0}C, and then were fixed with 70% chilled ethanol. Then the fixed cells were observed with confocal microscopy (LSM 880, Zeiss).

4.3.6 *Cell viability.* The MTT based cell viability was performed to assess the cytotoxicity of the drug. Initially, the HeLa cells were plated in 96-well plate at the density of 7 X 10^3 cells per well and left to attach overnight. After that, the cells were treated with the respective drugs for 48 h. At the end of the treatment period, MTT was used to assess the dose dependent decrease in the cell viability. The absorbance of the formazon generated by the live cells was taken at 570 nm subtracting the reference values taken at 650 nm. The data were acquired in Tecan 2000 pro plate reader. Cell viability percentage was calculated using this formula:

$$\%\ \boldsymbol{of\ cell\ viability} = \frac{(\boldsymbol{A_{570} - A_{650}})\ \boldsymbol{sample}}{(\boldsymbol{A_{570} - A_{650}})\ \boldsymbol{control}} \times\ \mathbf{100}$$

Here A_{570} denotes absorbance at 570 nm and A_{650} connotes absorbance (background) at 650 nm.

4.3.7 *Annexin V PI dual staining assay:* HeLa cells were treated with MTX NCs, MTX, and NPs for respective experiments for 48 h at 37 ^{0}C at respective IC_{50} concentrations. After that cells were stained with the PE Annexin V Apoptosis Detection Kit (559763) with protocol mentioned in it. The cells were then studied with flow cytometer (BD CytoFlex).

4.3.8 *ROS assay:* HeLa cells were treated with MTX NCs, MTX and NPs for respective experiments for 4 h at 37 ^{0}C and then were harvested. Cells were then incubated with 10 µM dichlorofluorescin diacetate (DCFDA) for 30 min at 37 ^{0}C and were subjected to flow cytometry (Beckman coulter CytoFlex). Results were analyzed with WinList 3D^{TM} software (Variety Software House).

4.3.9 *Statistics:* For MTT assay two way annova was performed with statistical significance depicted as ★ ($p < 0.05$), ★★ ($p < 0.01$), and ★★★ ($p < 0.001$).

4.4 Results and discussion

Experimentally, a solution of MTX, $HAuCl_4$ and mercapto propionic acid (MPA) in PBS was heated for 3 min. This resulted in clear solution sans the presence of any SPR active species, as it did not display any peaks in the SPR active region **(Figure 4.1 a)**. This solution when excited at 370 nm presented an emission maximum at 460 nm **(Figure 4.1 b)** suggesting the formation of luminescent MTX NCs.

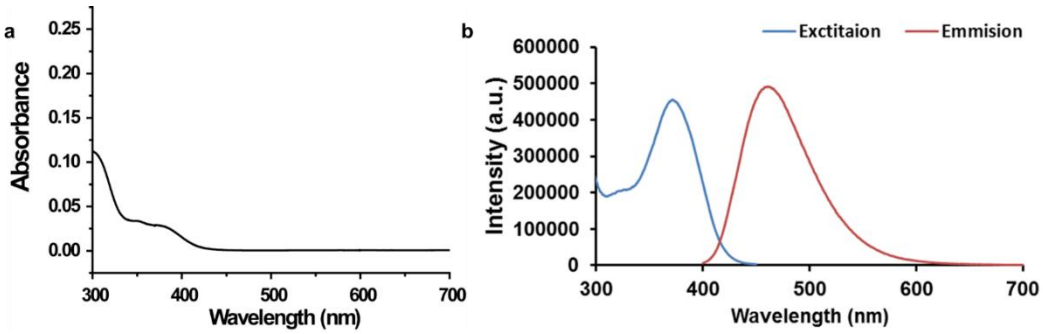

Figure 4.1: a) *UV-vis absorption of the MTX NCs displaying complete lack of any SPR peak and thus negating the formation of any SPR active component during the synthesis procedure.* ***b)*** *Excitation and emission profile of the MTX NCs.*

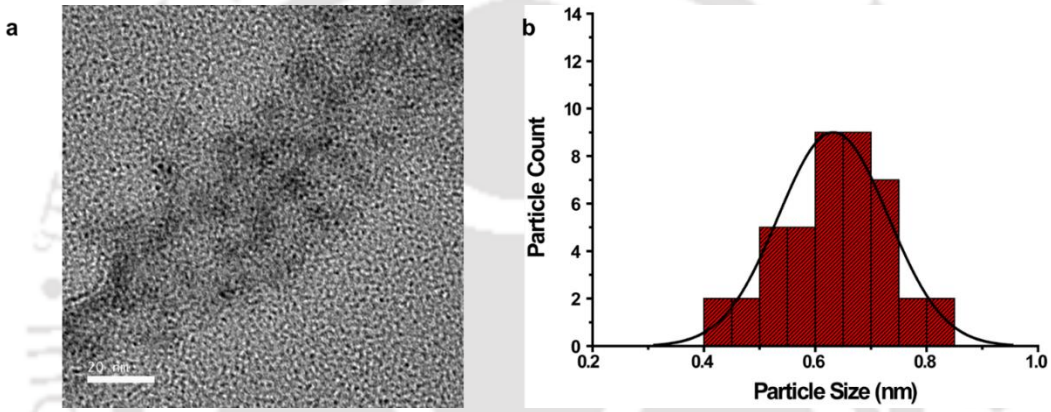

Figure 4.2: a) *TEM images of the MTX NCs* ***b)*** *Size distribution of the MTX NCs with the average size of the NCs being 0.64 ± 0.12 nm*

The formation of the MTX NCs was confirmed by TEM study, which revealed the formation of ultra-small NCs with an average size of 0.64 ± 0.12 nm **(Figure 4.2 a, b)**. An EDX study showed the presence of Au, thus confirming the MTX NCs gold composition **(Figure 4.3)**.

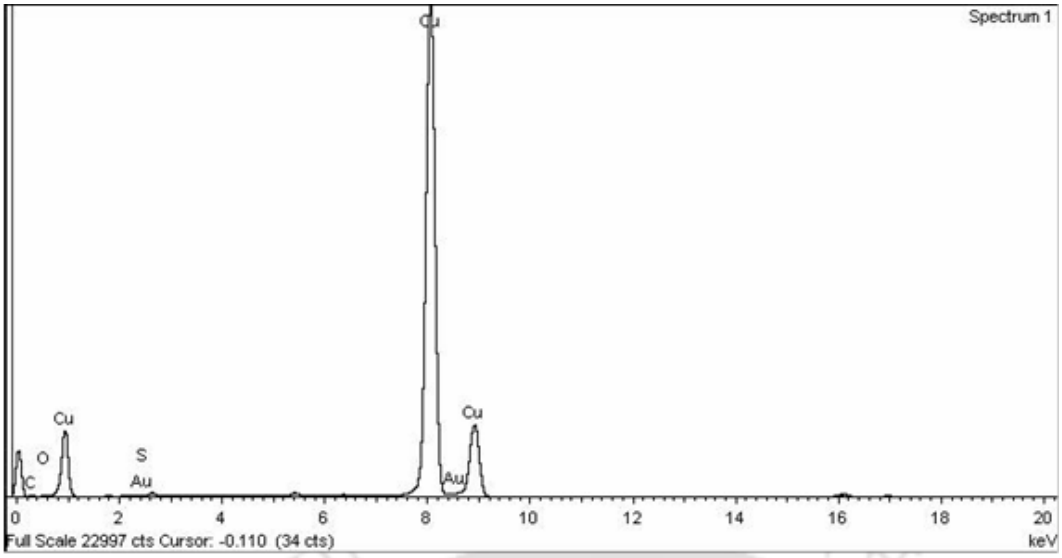

Figure 4.3: *EDX spectra of the MTX NCs, here the peaks of Au confirm the presence of gold in the NCs solution.*

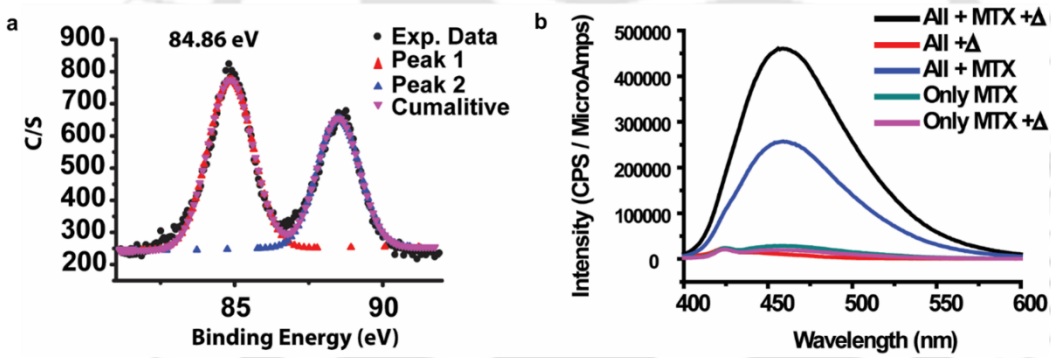

Figure 4.4: *XPS spectra of the MTX NCs* ***a)*** *confirming the presence of Au in Au (0) state* ***b)*** *Emission spectra displays that only MTX has a very little inherent fluorescence compared to the NCs and losses some of it if heated. It establishes the importance of the MTX as a template, because without MTX it didn't generate any fluorescence. It also establishes the importance of the brief heating required for the complete reduction of gold.*

The formation of luminescent MTX NCs and its oxidation state was further confirmed by XPS study. It is already reported that the peak position for Au 4f $_{7/2}$ lies between Au (0) state (84 eV) and Au (1) thiolate complex (86 eV)[14]. The XPS analysis revealed an Au 4f $_{7/2}$ peak at 84.8 eV **(Figure 4.4 a)**, which confirms the Au (0)

oxidation state for the Au entities in the synthesized solution. The enhanced binding energy obtained for the MTX NCs can be attributed to their smaller size as binding energy increases with decreasing size[15]. The presence of gold in Au (0) oxidation state further confirms the formation of the MTX NCs. It would be prudent here to mention the importance of templating activity of MTX as sans MTX the procedure did not generate any luminescent MTX NCs **(Figure 4.4 b)**. The interaction between MTX and gold nanoclusters is possibly of non-covalent nature. It is also interesting to note that although mere mixing of the components generates fluorescent entities, but a brief heating augmented the fluorescent intensity greatly **(Figure 4.4 b)**. This highlights the importance of brief heating for the efficient synthesis of the MTX NCs.

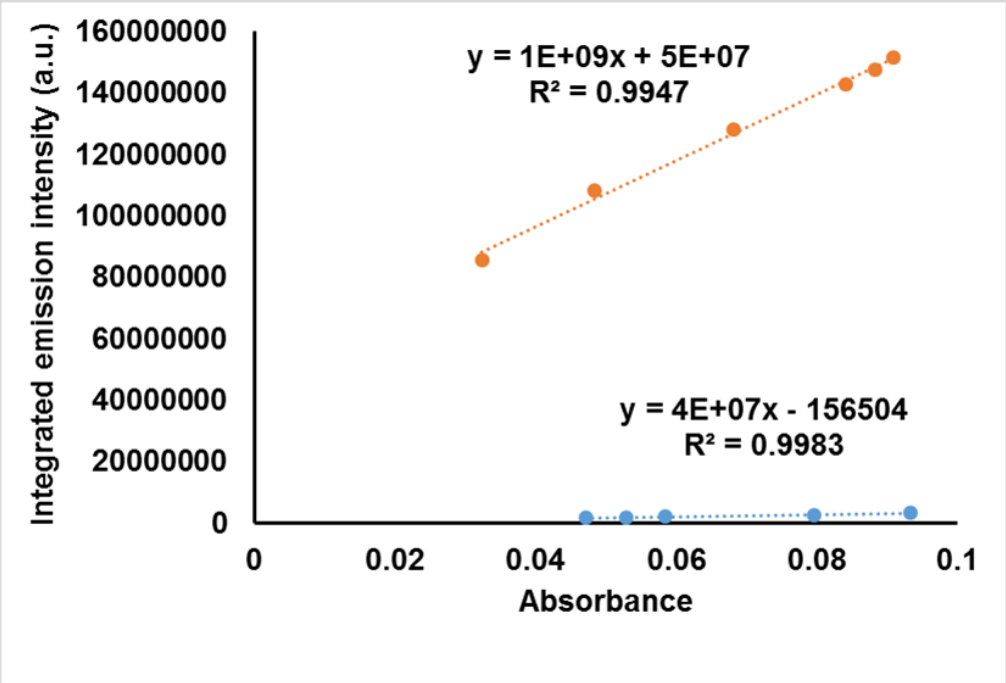

Figure 4.5: *Quantum yield of the MTX NCs was recorded 2.16 % with quinine sulphate used as reference.*

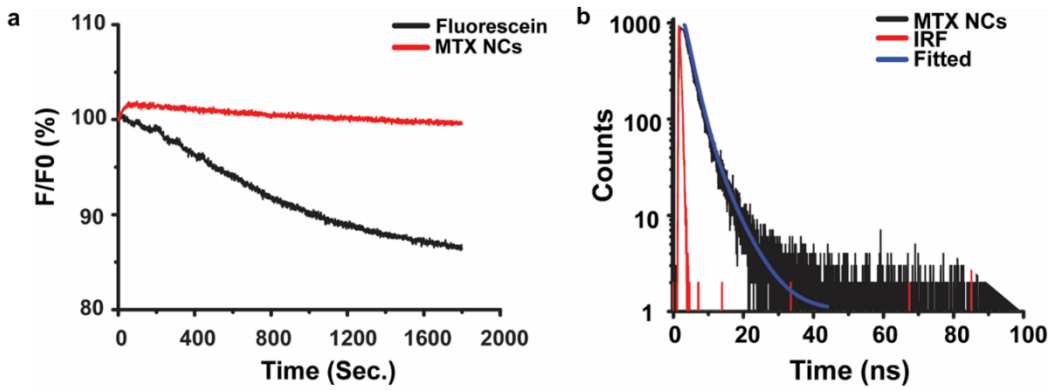

Figure 4.6: a) *Photostability of the MTX NCs when compared with fluorescein. While fluorescein suffered 1.02 % loss in fluorescence per min., MTX template Au NCs suffered only 0.16 % loss in fluorescence per min.* ***b)*** *Fluorescence decay profile of the MTX NCs.*

The synthesized MTX NCs revealed a quantum yield of 2.16 % when measured with quinine sulfate as reference **(Figure 4.5)**. The MTX NCs also exhibited a robust photostability when compared with organic dye fluorescein and suffered only 0.16 % loss in fluorescence per min. against 1.02 % loss accrued by fluorescein **(Figure 4.6 a)**. Time-resolved photoluminescence measurements revealed the presence of two lifetime components with fluorescence lifetime of 2.21 ns and 6.73 ns and is in sync with the existing literature[16] **(Figure 4.6 b)**. The average lifetime of the MTX NCs is 5.11 ns. The MTX NCs displayed a surface zeta potential of -38.6 mV **(Figure 4.7 a)**.

MALDI TOF analysis of the fluorescent solution confirmed the presence of two dominant Au species viz. Au_8 and Au_7 **(Figure 4.7 b)**. However, presence of multiple peaks can be attributed to the high laser intensity used in MALDI TOF analysis. Observed *m/z* differences between ion peaks can largely attributed to change in Au, S and MTX unit numbers. Presence of Au_8 is in coherence with its blue fluorescence as these findings corroborates with the emission profile of the MTX NCs, as Au NCs with blue emission are reported to have an Au_8 composition [16,14].

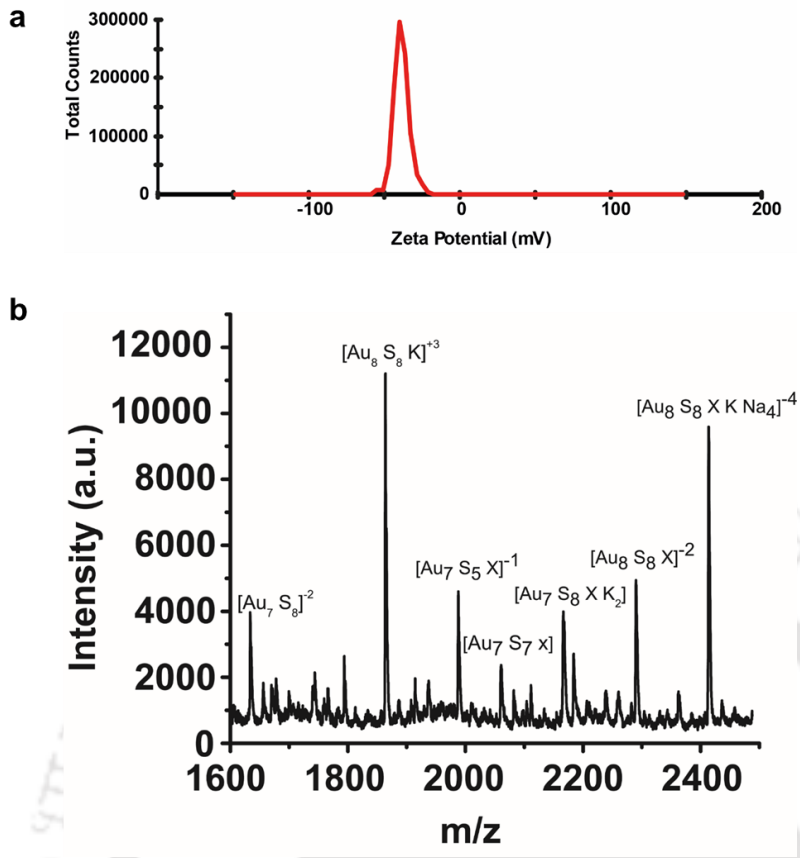

Figure 4.7: a) *Zeta potential of the MTX NCs* ***b)*** *MALDI TOF spectra of the MTX NCs solution largely establishes the presence of Au_8 as dominant species along with the Au_7 species, multiple peaks observed is due to enhanced fragmentation due to high laser energy used in MALDI TOF. Here X=454 (methotrexate). Here Sulphur is provided by the MPA and Na and K are provided by the PBS (reaction media).*

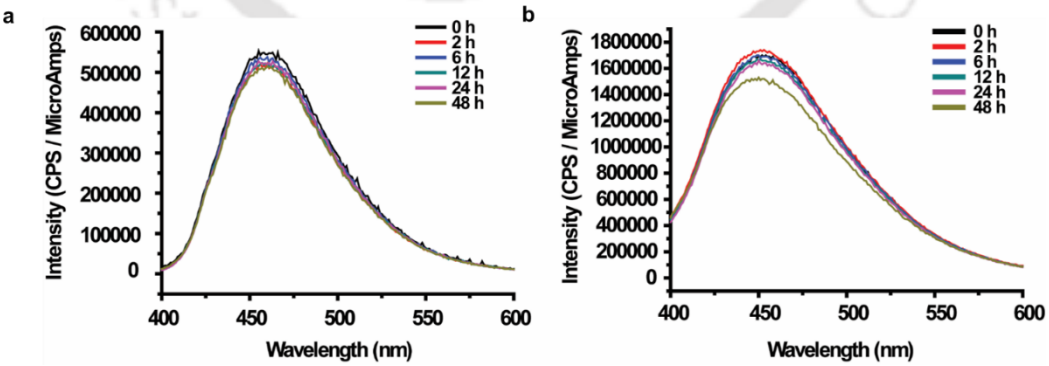

Figure 4.8: *Stability of the MTX NCs in* ***a)*** *PBS* ***b)*** *Serum. Stability of the MTX NCs was measured as a function of loss in their fluorescence with time when incubated in PBS and serum at 37 ^{0}C.*

As we intent, to use the MTX NCs as theranostics for which it has to be stable under both *in vivo* and *in vitro* conditions. For this, we measured the rate of loss of fluorescence as a parameter for MTX NCs stability. The synthesized MTX NCs were incubated with PBS (pH7.4) and with bovine serum albumin (BSA) at 37 ^{0}C to simulate its stability under physiological conditions and loss of fluorescence was periodically measured. Much to our surprise, MTX NCs suffered negligible loss of fluorescence in PBS and incurred mild loss of fluorescence in serum. This indicates the robust nature of the MTX NCs **(Figure 4.8)**.

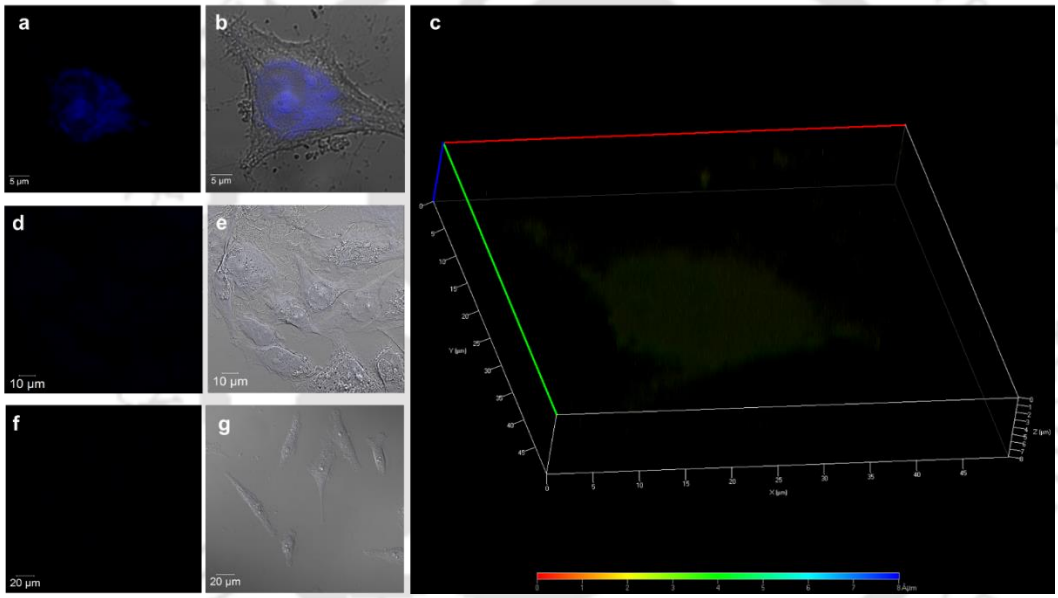

Figure 4.9: *Confocal microscopy of the HeLa cells* ***a)*** *fluorescence image of HeLa cell treated with the MTX NCs displaying the characteristic blue emission of the MTX NCs* ***b)*** *merged image (fluorescence and bright field image) of the same.* ***c)*** *A 8 µm Z stack projection of the same cells confirming the source of the fluorescence is within the cell rather than surface and thus confirming the uptake of the MTX NCs inside the cell.* ***d)*** *Fluorescence image of the cells treated with MTX displaying negligible fluorescence* ***e)*** *merged image of the same.* ***f)*** *Fluorescence image of the control cells* ***g)*** *merged image of the same.*

To evaluate the therapeutic (imaging and cytotoxicity) potential of the luminescent MTX NCs, the HeLa cells were treated with them. For that, first they have

to be taken up by the cells. To confirm the cellular uptake and to assess the imaging potential of the MTX NCs, we performed confocal microscopy. For this HeLa cells were incubated with MTX NCs and MTX for 4 h and then were studied with confocal microscopy. Cells treated with MTX NCs displayed the distinctive bright blue fluorescence of the MTX NCs **(Figure 4.9 a, b)**. Further Z stacking was performed to ascertain the source of the fluorescence was inside the cells rather than from surface of the cells **(Figure 4.9 c)**. While the cells treated with MTX displayed a negligible fluorescence **(Figure 4.9 d, e)**, the control cells displayed a kenspeckle absenteeism of any fluorescence **(Figure 4.9 f, g)**. The Z stack images also displayed a complete lack of any fluorescence from inside the cells both in MTX treated cells **(Figure 4.10 a)** and control cells **(Figure 4.10 b)** and is in corroboration with the uptake studies.

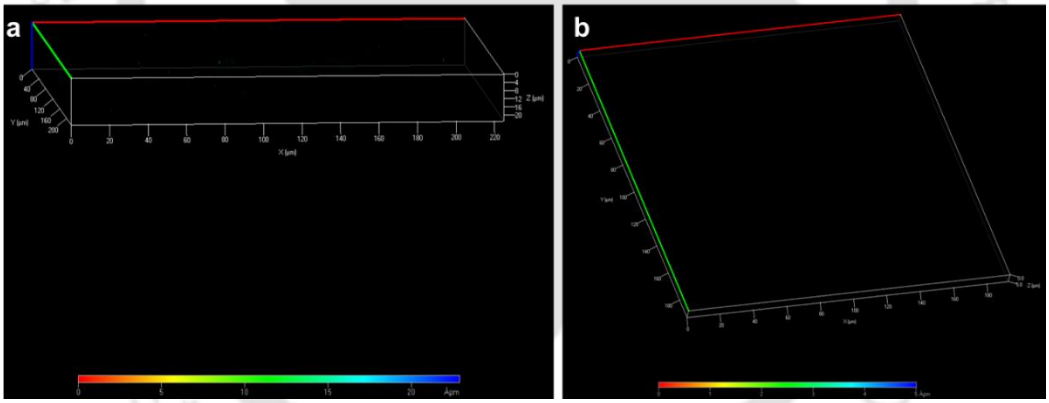

Figure 4.10: *Z stack of **a)** MTX treated cells and **b)** control cells displaying lack of any fluorescence from inside the cells.*

Next, to examine the cytotoxic potential of the MTX NCs we performed MTT (3-(4,5-Dimethylthiazol-2-Yl)-2,5-Diphenyltetrazolium Bromide) based cell viability assay on HeLa cells. HeLa Cells were incubated at 37 ^{0}C with different concentrations of MTX NCs (concentration of the MTX in MTX NCs) and MTX for 48 h. The results as shown in **Figure 4.11** propose an augmented cytotoxicity of the MTX NCs over the

template drug i.e. MTX. MTT assay presented an IC_{50} (half-maximal inhibitory concentration) value of 98 ng/ mL for MTX NCs and 188 ng/ mL for MTX. MTX NCs clearly showed an enhanced cytotoxicity against the MTX. The results also suggested that the active structure of the MTX remained intact during the synthesis procedure of MTX NCs.

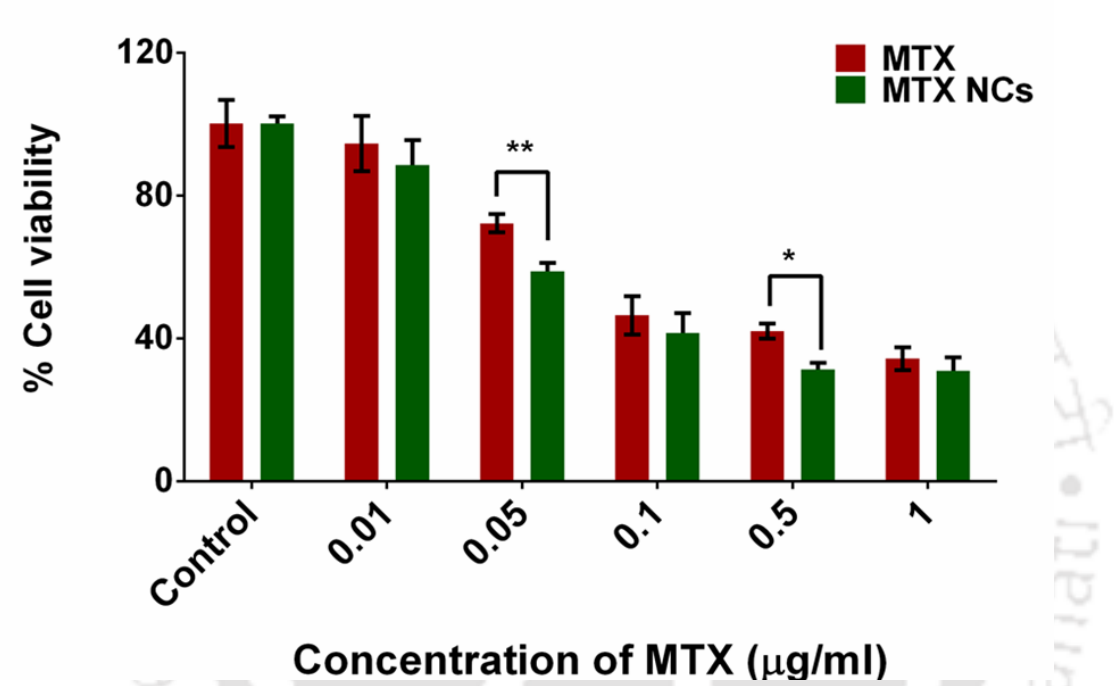

Figure 4.11: *MTT assay displaying the better cytotoxicity of the MTX NCs over the MTX. IC50 for MTX NCs and MTX is 98 ng/ mL and, 188 ng/ mL respectively. A two way annova was performed for determine the statistical significance depicted as ★ ($p < 0.05$), ★★ ($p < 0.01$), and ★★★ ($p < 0.001$).*

MTX is a well-established anticancer drug also used in treatment of other diseases like rheumatoid arthritis and other chronic inflammatory diseases[17]. MTX is primarily taken up into the cells by folate receptors, where active mode of transport dominates[18]. MTX inhibits dihydrofolate reductase (DHFR), which converts dihydrofolate into tetrahydrofolate, eventually resulting in inhibition of DNA and purine synthesis[19,20]. To ascertain the mechanism of cellular death in the present case,

PE tagged Annexin V- 7AAD dual staining assay was performed. The assay is based on the ability of Annexin V, a calcium dependent phospholipid binding protein, which preferentially binds with phosphatidylserine. It binds to the exposed phosphatidylserine due to the membrane flipping following the caspase activation, a typical feature of the early apoptosis[21]. Healthy cells however do not expose their phosphatidylserine and

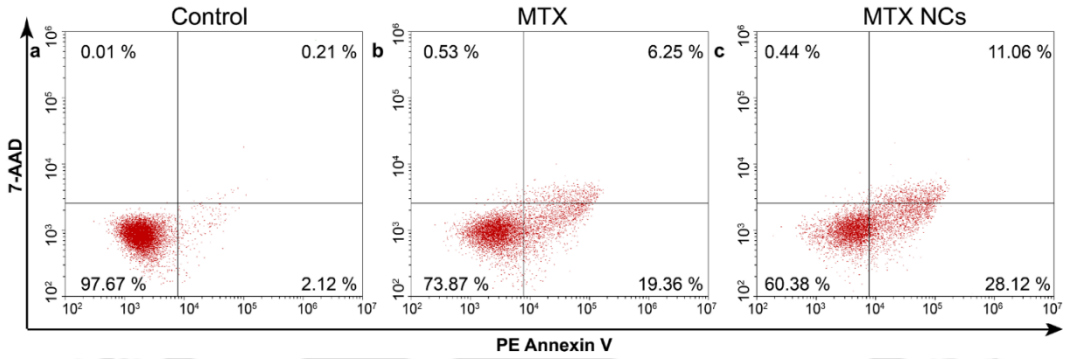

Figure 4.12: *PE Annexin V/ 7 AAD assay with* ***a)*** *control* ***b)*** *MTX* ***c)*** *MTX NCs. Here top left quadrant refers to dead population, top right quadrant refers to late apoptotic population, bottom left quadrant refers to live cells and the bottom right quadrant refers to early apoptotic population.*

remains on the cytosolic side of the plasma membrane. To further distinguish the early apoptotic cells from the membrane-compromised cells, a feature of late apoptotic and dead cells, a membrane impermeable nucleic acid binding dye was added. Here 7 AAD was used, which has a longer emission wavelength and allows better multiplexing with other fluorophores than PI[22]. So the population which was positive for both the dyes represented the apoptotic cells. Briefly, HeLa cells were treated with MTX and MTX NCs at their respective IC50 values for 48 h. After that the cells were dually stained with PE labelled Annexin V and then counterstained with 7 AAD to be subsequently analyzed with flow cytometry. While the control cells displayed only 0.20 % dual positive population (**Figure 4.12 a**), the cells treated with the MTX and MTX NCs

displayed a dual positive population of 6.25 % (**Figure 4.12 b**) and 11.25% (**Figure 4.12 c**) respectively.

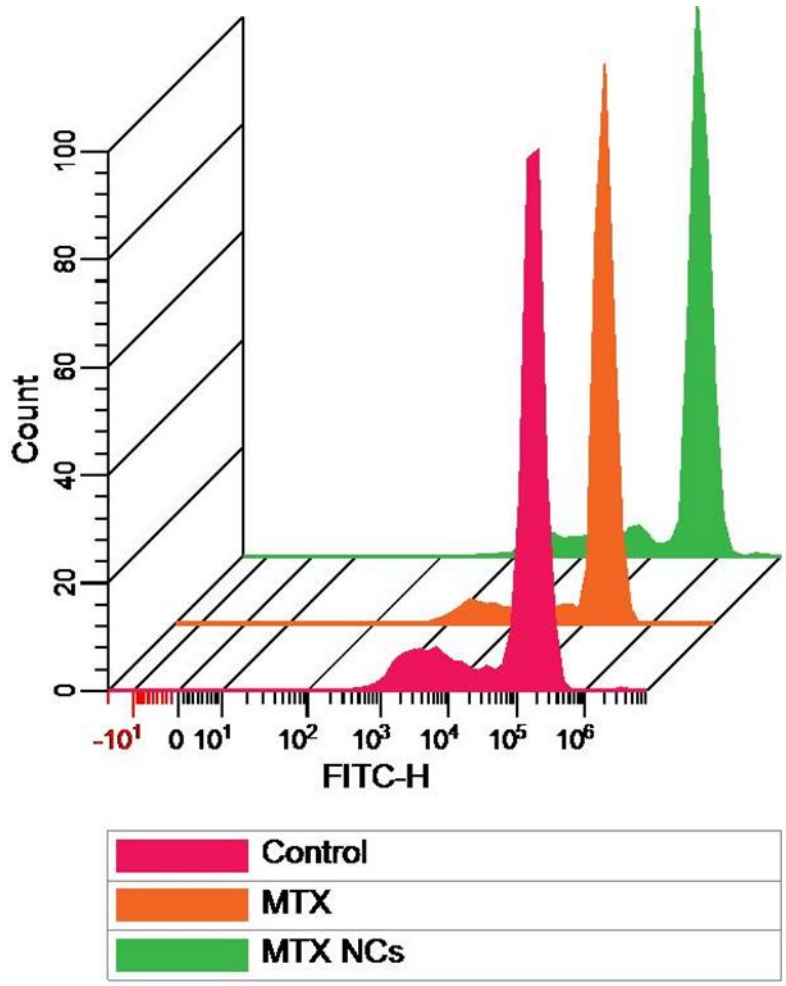

Figure 4.13: *ROS generation by MTX NCs is higher than MTX, which in turn generated more ROS than control groups.*

Additionally, MTX and MTX NCs both generated considerable amount of ROS in HeLa cells after 4 h of treatment against the control cells. However, the ROS production with MTX NCs was considerably higher than MTX **(Figure 4.13)**. Enhanced ROS level leads to mitochondrial mediated apoptosis and generation of ROS by MTX has been well documented [23].

4.5 Conclusions

In conclusion, a single unit nanotheranostic serving both the therapeutic and the imaging was developed. These MTX NCs had an augmented cytotoxicity *vis a vis* the free drug while at same time was fluorescent, so employed for cellular imaging. The MTX NCs remained stable both in serum and PBS, this can be taken as a harbinger for its potential *in vivo* application. The potential of using these MTX NCs instead of free drug in a DDV platform was also demonstrated with improved cytotoxicity and additional capabilities. The ease and simplicity of the synthesis procedure can prompt development of drug templated theranostic and thus in turn can open a new avenue in the field of nanotheranostics.

4.6 References

(1) Chen, H.; Zhang, W.; Zhu, G.; Xie, J.; Chen, X. Rethinking Cancer Nanotheranostics. *Nat. Rev. Mater.* **2017**, *2* (May), 17024.

(2) Cole, J. T.; Holland, N. B. Multifunctional Nanoparticles for Use in Theranostic Applications. *Drug Deliv. Transl. Res.* **2015**, *5* (3), 295–309.

(3) Peng, H.; Liu, X.; Wang, G.; Li, M.; Bratlie, K. M.; Cochran, E.; Wang, Q. Polymeric Multifunctional Nanomaterials for Theranostics. *J. Mater. Chem. B* **2015**, *3* (34), 6856–6870.

(4) Gobbo, O. L.; Sjaastad, K.; Radomski, M. W.; Volkov, Y.; Prina-Mello, A. Magnetic Nanoparticles in Cancer Theranostics. *Theranostics* **2015**, *5* (11), 1249–1263.

(5) Chen, L. Y.; Wang, C. W.; Yuan, Z.; Chang, H. T. Fluorescent Gold

Nanoclusters: Recent Advances in Sensing and Imaging. *Anal. Chem.* **2015**, *87* (1), 216–229.

(6) Patitsa, M.; Karathanou, K.; Kanaki, Z.; Tzioga, L.; Pippa, N.; Demetzos, C.; Verganelakis, D. A.; Cournia, Z.; Klinakis, A. Magnetic Nanoparticles Coated with Polyarabic Acid Demonstrate Enhanced Drug Delivery and Imaging Properties for Cancer Theranostic Applications. *Sci. Rep.* **2017**, *7* (1), 775.

(7) Luong, D.; Sau, S.; Kesharwani, P.; Iyer, A. K. Polyvalent Folate-Dendrimer-Coated Iron Oxide Theranostic Nanoparticles for Simultaneous Magnetic Resonance Imaging and Precise Cancer Cell Targeting. *Biomacromolecules* **2017**, *18* (4), 1197–1209.

(8) Xu, P.; Zuo, H.; Chen, B.; Wang, R.; Ahmed, A.; Hu, Y.; Ouyang, J. Doxorubicin-Loaded Platelets as a Smart Drug Delivery System: An Improved Therapy for Lymphoma. *Sci. Rep.* **2017**, *7* (January), 42632.

(9) Bagalkot, V.; Farokhzad, O. C.; Langer, R.; Jon, S. An Aptamer-Doxorubicin Physical Conjugate as a Novel Targeted Drug-Delivery Platform. *Angew. Chemie - Int. Ed.* **2006**, *45* (48), 8149–8152.

(10) Zheng, J.; Nicovich, P. R.; Dickson, R. M. Highly Fluorescent Noble Metal Quantum Dots. *Annu. Rev. Phys. Chem.* **2008**, *22* (5), 4109.

(11) Venkatesh, V.; Shukla, A.; Sivakumar, S.; Verma, S. Purine-Stabilized Green Fluorescent Gold Nanoclusters for Cell Nuclei Imaging Applications. *ACS Appl. Mater. Interfaces* **2014**, *6* (3), 2185–2191.

(12) Qu, X.; Li, Y.; Li, L.; Wang, Y.; Liang, J.; Liang, J. Fluorescent Gold

Nanoclusters: Synthesis and Recent Biological Application. *J. Nanomater.* **2015**, *2015*.

(13) Bao, Y.; Yeh, H.-C.; Zhong, C.; Ivanov, S. a.; Sharma, J. K.; Neidig, M. L.; Vu, D. M.; Shreve, A. P.; Dyer, R. B.; Werner, J. H.; et al. Formation and Stabilization of Fluorescent Gold Nanoclusters Using Small Molecules. *J. Phys. Chem. C* **2010**, *114* (38), 15879–15882.

(14) Kawasaki, H.; Hamaguchi, K.; Osaka, I.; Arakawa, R. Ph-Dependent Synthesis of Pepsin-Mediated Gold Nanoclusters with Blue Green and Red Fluorescent Emission. *Adv. Funct. Mater.* **2011**, *21* (18), 3508–3515.

(15) Tanaka, A.; Takeda, Y.; Imamura, M.; Sato, S. Dynamic Final-State Effect on the Au 4f Core-Level Photoemission of Dodecanethiolate-Passivated Au Nanoparticles on Graphite Substrates. *Phys. Rev. B* **2003**, *68* (19), 195415.

(16) Zheng, J.; Petty, J. T.; Dickson, R. M. High Quantum Yield Blue Emission from Water-Soluble Au8 Nanodots. *J. Am. Chem. Soc.* **2003**, *125* (26), 7780–7781.

(17) Huang, C. C.; Hsu, P. C.; Hung, Y. C.; Liao, Y. F.; Liu, C. C.; Hour, C. T.; Kao, M. C.; Tsay, G. J.; Hung, H. C.; Liu, G. Y. Ornithine Decarboxylase Prevents Methotrexate-Induced Apoptosis by Reducing Intracellular Reactive Oxygen Species Production. *Apoptosis* **2005**, *10* (4), 895–907.

(18) Cowan, D. S. M.; Tannock, I. F. Factors That Influence the Penetration of Methotrexate through Solid Tissue. *Int. J. Cancer* **2001**, *91* (1), 120–125.

(19) Bertino, J. R.; Göker, E.; Gorlick, R.; Li, W. W.; Banerjee, D. Resistance Mechanisms to Methotrexate in Tumors. *Stem Cells* **1996**, *14*, 5–9.

(20) Cronstein, B. N. Molecular Therapeutics: Methotrexate and Its Mechanism of Action. *Arthritis Rheum.* **1996**, *39* (12), 1951–1960.

(21) Zhang, G.; Gurtu, V.; Kain, S. R.; Yan, G. Early Detection of Apoptosis Using a Fluorescent Conjugate of Annexin V. *Biotechniques* **1997**, *23* (3), 525–531.

(22) Jiang, L.; Tixeira, R.; Caruso, S.; Atkin-Smith, G. K.; Baxter, A. A.; Paone, S.; Hulett, M. D.; Poon, I. K. H. Monitoring the Progression of Cell Death and the Disassembly of Dying Cells by Flow Cytometry. *Nat. Protoc.* **2016**, *11* (4), 655–663.

(23) Phillips, D. C.; Woollard, K. J.; Griffiths, H. R. The Anti-Inflammatory Actions of Methotrexate Are Critically Dependent upon the Production of Reactive Oxygen Species. *Br. J. Pharmacol.* **2003**, *138* (3), 501–511.

Chapter 5

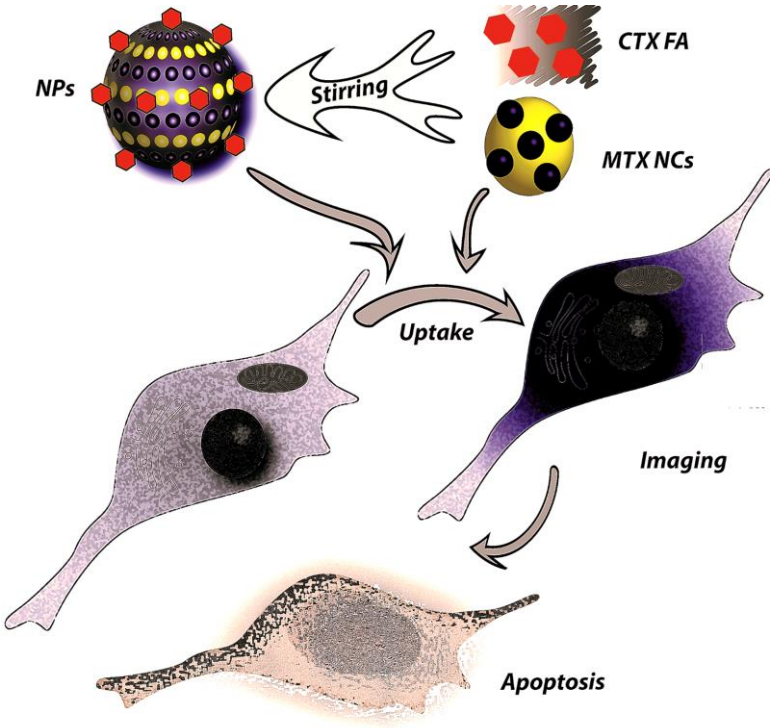

Evaluating the potential of MTX NCs to replace MTX on a Drug Delivery Platform

Bandhan Chatterjee, Asif Raza, and Siddhartha Sankar Ghosh.

ABSTRACT

Folic acid conjugated chitosan nanoparticles were developed to deliver MTX NCs into HeLa cells. The NPs were brightly fluorescent and retained the physical characteristics of the MTX NCs. The NPs were stable in both PBS and serum. The NPs displayed a decent loading profile and maintained a sustained release profile in both acetate buffer and PBS. The NPs displayed augmented cytotoxicity than the MTX NCs with concurrent cellular imaging, owing to their efficient transport. The mode of cytotoxicity remains same for the NPs as MTX NCs.

Evaluating the Potential of MTX NCs to Replace MTX on a Drug Delivery Platform

5.1 Introduction

Nanocarriers offer a platform for the shuttling of various payloads to complex destinations. These payloads need not be of a uniform composition, but can encompass payloads of different compositions[1,2]. This feature facilitates the realization of theranostics, an entity having two functional modalities, one therapeutic and other diagnostic[3]. This negates the need of separate modalities being pushed into body and complexing the therapy with differential biodistribution. Traditionally theranostics are composed of two separate entities for therapeutic and diagnostic purpose, loaded onto to nanocarrier[4]. However, there can be compatibility issue of the loaded components owing to their different physical characteristics. To resolve this, we need single entity theranostics, which may have a composite chemical composition, but essentially is a single inseparable entity, and have coalesced the constituent entities into one, while retaining their functionalities. This basically overcomes the compatibility issue. Other possible issue can be the very size of the theranostic, as favorable size regime for efficient transport is very stringent and window is quite narrow[5]. So much attention has to be paid for tuning the size of the theranostic as many of the nanocarriers suffer from a bigger size thus hampering their very uptake by the cellular system.

A small single entity theranostic with robust stability can be a suitable solution for many of the aforementioned issues. Further these nanotheranostics should be able to function independently as well as in tandem with the available nanocarrier platforms. Nanocarriers offer various advantages over direct delivery of payloads, like efficient and targeted transport, enhanced biocompatibility and retention time, half-life[6]. These

nanocarriers can often be functionalized and tailored to the needs of a particular case[7–10]. For instance, a nanocarrier can be conjugated with a targeting moiety for specific delivery; can have specific release triggers like pH thus reducing the random spillage. Nanocarriers can have myriad types of composition[11]. There are polymeric nanoparticles, dendrimers, polymeric micelles, liposomes, composite nanoparticles and metal nanoparticles, all of them having their own pros and cons[2,12].

5.2 Outline of the research work

- A simple and quick synthesis of a luminescent gold nanoclusters using methotrexate as a template was established. These synthesized methotrexate templated gold nanoclusters (MTX NCs) at one hand were brightly fluorescent, have decent quantum yield and photostability rendering it a suitable imaging moiety for various theranostic platforms and on the other hand, it displayed an augmented cytotoxicity than the free drug. In effect coalescing two separate functional units into a single unit.

- Chitosan was conjugated with folic acid using a reported protocol. The conjugation was verified with FTIR.

- MTX NCs were loaded on to a chitosan folic acid nanoparticle to form a theranostic NP. The NPs were roughly spherical with an average size of 69 ± 11 nm.

- NPs were then thoroughly characterized with various analytical techniques, like fluorescence spectroscopy and electron microscopy. The NPs retained the fluorescent properties of the MTX NCs.

- The NPs displayed a decent loading profile. The release pattern was evaluated both in PBS and acetate buffer medium simulating the endosomal as well as physiological conditions.

- The NPs displayed a robust stability, measured in terms of loss in fluorescence, both in serum as well as in PBS, one of the prime requisite of a theranostic, instantiating the plausibility of its *in vivo* use as a theranostic.

- The anti-proliferation propensity of the NPs was assessed on HeLa cells. The cell viability assays marked the astonishing cytotoxicity over both the free drug as well as the MTX NCs, which can be attributed to the efficient shuttling aptitude of the NPs.

- The uptake of the NPs into the cellular system was measured with flow cytometry and confocal microscopy. Once inside the cells, these luminescent entities facilitated confocal microscopy assisted cellular imaging of the host cells.

- The mode of cytotoxicity as determined with flow cytometry mediated, DCFHDA based ROS study and Annexin V/ PE dual staining assay, remained similar with MTX NCs, but produced an enhanced effect. This further attests the amenability of the MTX NCs to be used on a nanocarrier platform.

5.3 Experimental section

5.3.1 *Chemicals:* $HAuCl_4$ (Au, 17 wt % in dilute HCl; 99.99%), mercapto propionic acid (MPA), methotrexate hydrate, chitosan (viscosity averaged molecular weight, Mv, 672 kDa, and degree of deacetylation >75%), folic acid, and sodium tripolyphosphate (TPP) were obtained from Sigma-Aldrich

and used as received. Milli-Q grade water (>18 MΩ cm^{-1}, Millipore) was used in all experiments.

5.3.2 *Synthesis of MTX NCs:* 20 µL of MTX (0.45 mg/ mL), 6 µL of 10 mM of $HAuCl_4$ and 2 µL of 11 M MPA were dissolved in 150 µL of PBS (1 X) and heated at 80 ^{0}C for 3 min., which yields the clear solution of luminescent MTX NCs.

5.3.3 *Chitosan Folic acid conjugation:* Folic acid was first activated with EDC in 20 mL of anhydrous DMSO (molar ratio of Folic acid and EDC was 1:1), conjugation was confirmed with FTIR (PerkinElmer) study of the lyophilized sample.

5.3.4 *Formation of NPs:* MTX NCs were added to the CTX FA acid solution and was stirred for 10 min. Then STPP was added to the solution with constant stirring for 10 min. After that the solution was centrifuged and the pellet was resuspended in media for cellular experiments and in Milli-Q for physical experiments.

5.3.5 *Characterizations:* UV measurements were measured with PerkinElmer Lambda 25 spectrophotometer. Fluorescence spectra were measured with Fluorolog −3, Horiba Jobin Edison, NY, USA. Zeta measurements were performed with Malvern Zetasizer. TEM analysis and EDX analysis was done with JEM 2100; Jeol machine.

5.3.6 *Loading of MTX NCs:* loading was measured using the following formula:

$$\textbf{\textit{Loading efficiency}} = \frac{\textbf{\textit{Total MTX}} - \textbf{\textit{MTX in supernatant}}}{\textbf{\textit{Total MTX}}}$$

The concentration of MTX was measured by its UV-vis absorbance at 310 nm.

5.3.7 *Release:* For this, NPs were incubated in acetate buffer (pH 4.5) and PBS (pH 7.4) at 37 ^{0}C. Samples were periodically removed and centrifuged at 10000 rpm for 15 min. and concentration of the released MTX was measured in the supernatant using U.V. absorption at 310 nm.

5.3.8 *Cellular assays:* All cellular assay were carried out on Human cervical cancer cell line (HeLa) and were procured from National Centre for Cell Sciences, Pune, India. HeLa cells were cultured in Dulbecco's Modified Eagle's Medium (DMEM) supplemented with 10% FBS, 100 units/ ml Penicillin, and 100 µg/ ml Streptomycin and were incubated at 37 ^{0}C for 12 h under humid conditions with 5% CO_2 for attachment conditions prior to any treatment.

5.3.9 *Cellular Uptake:* HeLa cells were treated with MTX and NPs for respective experiments for 4 h at 37 ^{0}C.

5.3.10 *Cellular imaging and Z stacking:* HeLa cells were treated with MTX and NPs for respective experiments for 4 h at 37 ^{0}C, and then were fixed with 70% chilled ethanol. Then the fixed cells were observed with confocal microscopy (LSM 880, Zeiss).

5.3.11 *Cell viability:* The MTT based cell viability was performed to assess the cytotoxicity of the drug. Initially, the Hela cells were plated in 96-well plate at the density of 7 X 10^3 cells per well and left to attach overnight. After that, the cells were treated with the respective drugs for 48 h. At the end of the treatment period, MTT was used to assess the dose dependent decrease in the cell viability. The absorbance of the formazon generated by the live cells was taken at 570 nm subtracting the reference values taken at 650 nm.

The data were acquired in Tecan 2000 pro plate reader. Cell viability percentage was calculated using this formula:

$$\%\ \boldsymbol{of\ cell\ viability} = \frac{(\boldsymbol{A_{570} - A_{650}})\ \boldsymbol{sample}}{(\boldsymbol{A_{570} - A_{650}})\ \boldsymbol{control}} \times \mathbf{100}$$

Here A_{570} denotes absorbance at 570 nm and A_{650} connotes absorbance (background) at 650 nm.

5.3.12 *ROS assay:* HeLa cells were treated with MTX NCs, MTX and NPs for respective experiments for 4 h at 37 ^{0}C and then were harvested. Cells were then incubated with 10 µM dichlorofluorescin diacetate (DCFDA) for 30 min at 37 ^{0}C and were subjected to flow cytometry (Beckman coulter CytoFlex).

5.3.13 *Statistics:* For MTT assay two way annova was performed with statistical significance depicted as ★ ($p < 0.05$), ★★ ($p < 0.01$), and ★★★ ($p < 0.001$).

5.4 Results and discussion

In the present work, the potential of the MTX NCs as a superior alternative to parent drug is evaluated on a nanocarrier platform. For this, folic acid functionalized chitosan was chosen, as chitosan is biodegradable, biocompatible and is widely used in various DDVs[13] and Folic acid renders the NPs a targeted DDV[13]. Folic acid receptors are expressed on almost all cells but are hyper expressed on cancer cells [14]. Folic acid receptor expression also varies with cancer types, for instance cervical cancer cells (HeLa) have higher expression of folate receptors in comparison to lung adenocarcinoma (A549 cells)[15], so this varied level of expression can and has been

utilized in various delivery platforms for targeted delivery of payloads[16]. Folic acid was conjugated with chitosan by the formation of an amide bond between them using EDC as a coupling agent. The bond formation was confirmed with FTIR study where the peaks at 1635 **cm^{-1}** and 1572 **cm^{-1} (Figure 5.1)** correspond to Vs of amide 1 (-C=O-) and Vs of amide 2 (N-H) respectively.[17,18]

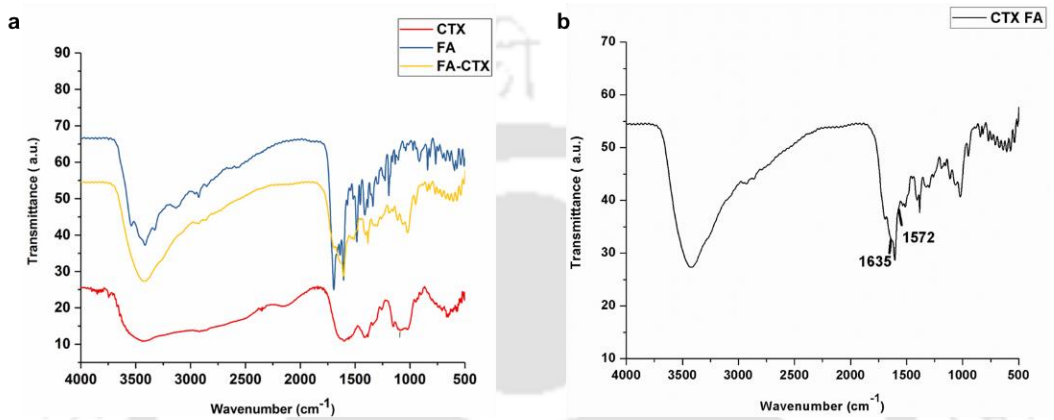

Figure 5.1: a) *FTIR spectra of chitosan (CTX), Folic acid (FA) and CTX FA conjugated,* ***b)*** *peaks at 1635* ***cm^{-1}*** *and 1572* ***cm^{-1}*** *corresponds to Vs of amide 1 (-C=O-) and Vs of amide 2 (N-H), respectively.*

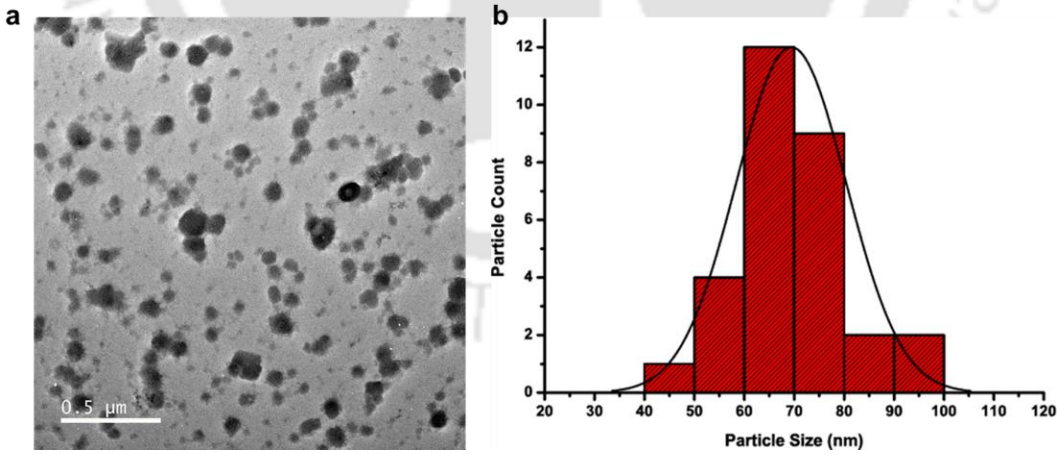

Figure 5.2: a) *TEM images of the NPs displaying their spherical size* ***b)*** *Size distribution of the same with average size of 69 ± 11 nm.*

Then folic acid functionalized chitosan was used to prepare MTX NCs loaded CTX FA NPs. The loading efficiency was 30%. The NPs produced were almost spherical **(Figure 5.2 a)** and had an average size of 69 ± 11 nm (one standard deviation) **(Figure 5.2 b)**. The NPs were fluorescent having the same excitation and emission maxima i.e. 370 nm and 460 nm respectively **(Figure 5.3 a, b)**, as the loaded MTX NCs thus suggesting the inclusion of the MTX NCs into the NPs. This notion was further supported by the EDX study **(Figure 5.4)**, which revealed the presence of gold into the same TEM micrographs of the NPs confirming the inclusion of the MTX NCs in the NPs. The NPs had a zeta potential of 15.5 mV **(Figure 5.5)**. The NPs largely retained its fluorescence both in PBS and serum for 48 h suggesting a

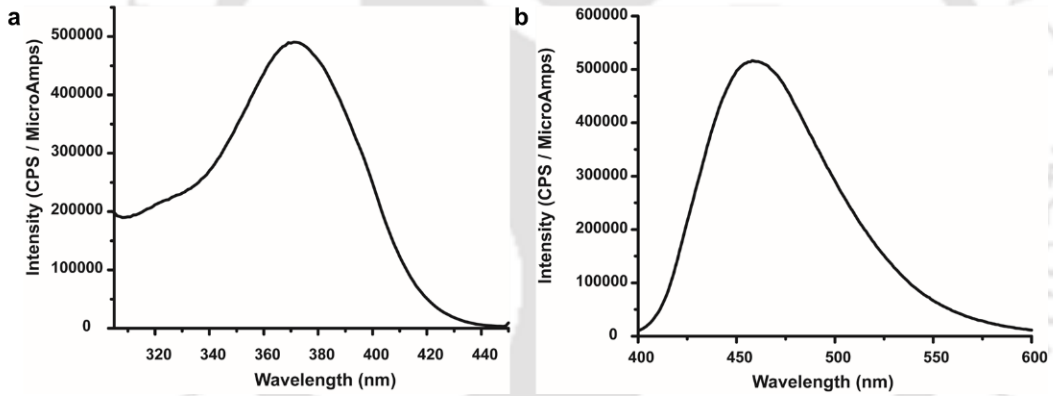

Figure 5.3: a) *Excitation and* ***b)*** *Emission profile of the NPs displaying the same respective maxima as the MTX NCs viz. 370 nm and 460 nm.*

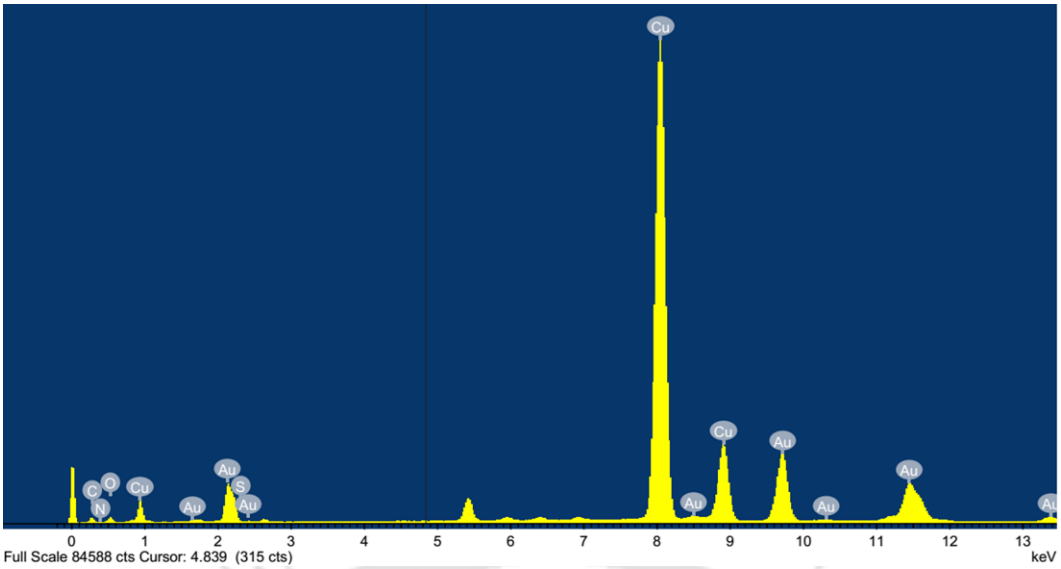

Figure 5.4: *EDX spectra of the NPs confirming the presence of the gold in it thus the presence of the MTX NCs.*

stable nature of the NPs **(Figure 5.6 a, b)**. The NPs maintained a sustained release of the MTX over time. The NPs observed an initial outburst releasing 44 % of the drug in first 6 h in acetate medium, after which a sustained release pattern was observed with 71 % of the drug being released over the period of 48 h **(Figure 5.7 a)**. The release pattern was similar in PBS mimicking the physiological pH, but the release was slower than the former. In PBS it released 29.5 % in first 6 h and 53 % over 48 h.

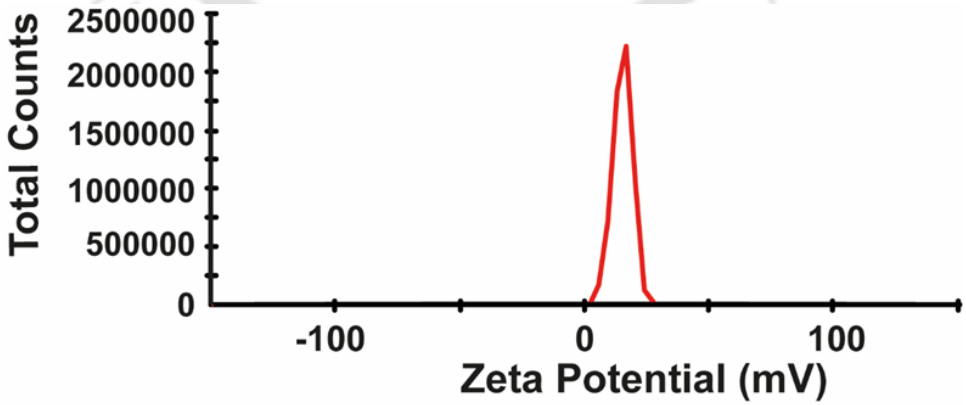

Figure 5.5: *Zeta potential of the NPs was 15.5 mV.*

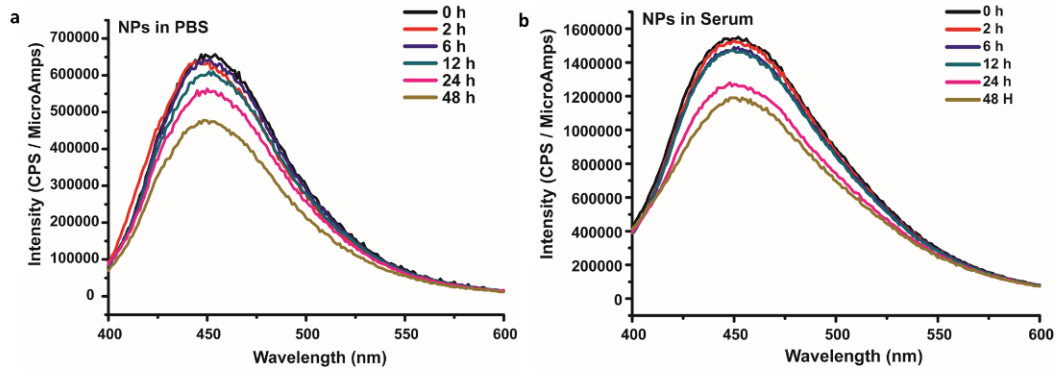

Figure 5.6: *Stability of the NPs measured as a function of the loss in fluorescence per unit h* ***a)*** *in PBS* ***b)*** *in serum.*

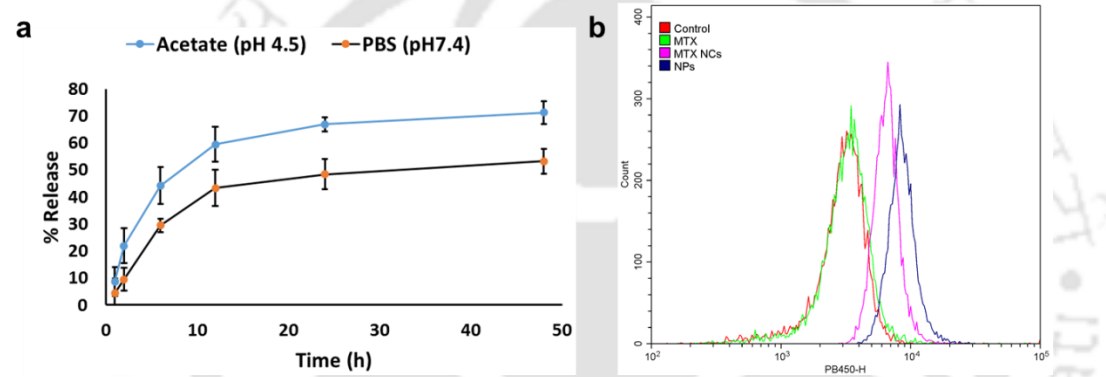

Figure 5.7: a) *Release profile of the NPs reveling the sustained release pattern both in acetate and PBS buffer, however, release was more in acetate buffer.* ***b)*** *Uptake profile of the NPs.*

HeLa cells were chosen to evaluate the therapeutic (imaging and cytotoxicity) potential of the luminescent NPs. To unfold its theranostic potential, first they have to be taken up by the cells. To confirm the cellular uptake of the NPs we treated the HeLa cells with NPs and MTX for 4 h and then cells were studied with flow cytometry **(Figure 5.7 b)**. Cells treated with NPs displayed a higher luminescence in PB 450 channel (range 427.5nm-472.5nm) as compared to control cells confirming their efficient uptake by the cells. Cells treated with MTX however presented similar fluorescence intensity to control cells, but it should be noted here that MTX has a

feeble inherent fluorescence as compared to MTX NCs. So even, if MTX was taken up by the cells due to lack of fluorescence it couldn't be ascertained by this study. Once uptake was confirmed, the imaging ability of the NPs was assessed with the confocal microscopy. Briefly, HeLa cells were treated with NPs for 4 h and were then examined under a confocal microscopy. The NPs treated cells were brightly illuminated with blue fluorescence, which can be attributed to the NPs **(Figure 5.8 a, b)**. This also suggested that the NPs were taken up by the cells, a notion further confirmed by Z stacking. The presence of green fluorescence in the Z stacking establishes the source of fluorescence was indeed from within the cells rather than the surface **(Figure 5.8 c)**. On the other hand, control cells displayed a speckle absenteeism of fluorescence **(Figure 5.8 d, e)**.

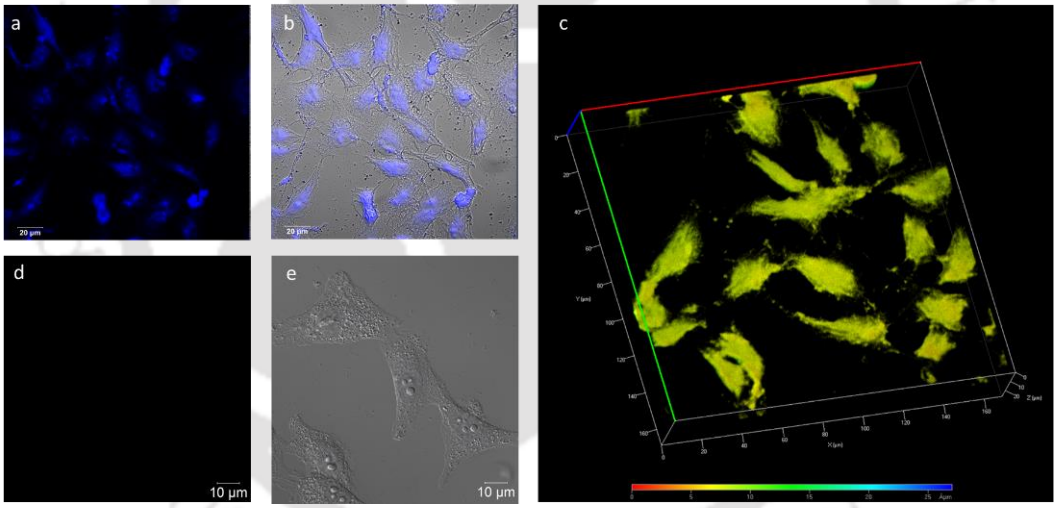

Figure 5.8: *Confocal microscopy of the HeLa cells* ***a)*** *Fluorescence image of HeLa cell treated with the NPs displaying the characteristic blue emission of the NPs.* ***b)*** *Merged image (fluorescence and bright field image) of the same* ***c)*** *an 8 µm Z stack projection of the same cells confirming the source of the fluorescence is within the cell rather than surface and thus confirming the uptake of the NPs inside the cell* ***d)*** *Fluorescence image of the control cells displaying negligible fluorescence* ***e)*** *Merged image of the same.*

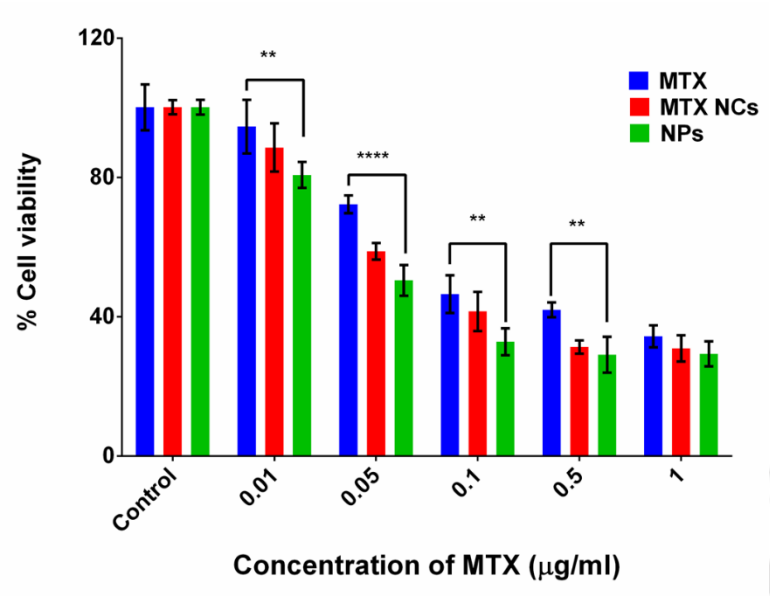

Figure 5.9: *MTT assay displaying the cell viability of HeLa cells after treatment with the NPs. A two-way ANOVA was performed for determine the statistical significance depicted as ★ ($p < 0.05$), ★★ ($p < 0.01$), and ★★★ ($p < 0.001$).*

After confirming the uptake, we assessed the therapeutic aptitude of the NPs with MTT (3-(4,5-Dimethylthiazol-2-Yl)-2,5-Diphenyltetrazolium Bromide), a cell viability assay on HeLa cells. For this HeLa cells were treated with different concentration of the NPs (different concentration of MTX in the loaded MTX NCs) for 48 h at 37 ^{0}C. The NPs displayed an IC_{50} value of 48.16 ng/ mL (**Figure 5.9**), which was better than the MTX NCs themselves. This could be explained due to the efficient transporting ability of targeted NPs and is one of the hallmarks of the targeted NPs. Further, ROS study was performed to further validate the mode of apoptosis. As MTX is already reported to generate ROS and this augmented level of ROS leads to apoptosis mediated cell death[19]. ROS study agrees with the MTT results, as the NPs generated the maximum amount of ROS followed by MTX NCs, and the finally MTX (**Figure 5.10**). NP generating higher ROS than the MTX NCs was possibly due to the better transport of the drug and is in concurrence with the MTT results. The ROS study also supported

that during loading the nature of the MTX NCs or the constituent MTX were not affected.

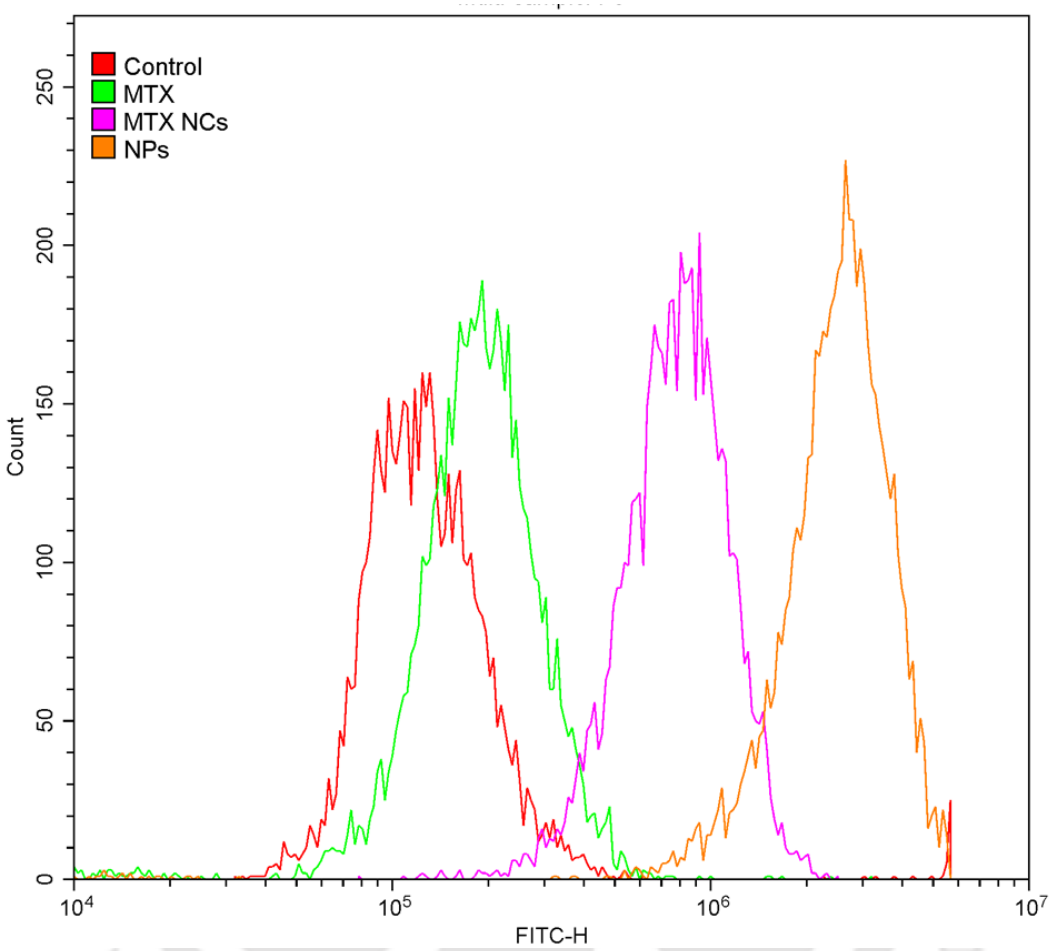

Figure 5.10: *MTX NCs loaded NPs generated the highest amount of ROS and is significantly higher than the MTX NCs themselves owing to the better transport of the MTX NCs.*

5.5 Conclusions

In essence, we have shown here the potential of the MTX NCs to replace the MTX (free drug) as a superior alternative to be used in a drug delivery platform. For this folic acid conjugated chitosan nanoparticles were made and MTX NCs were loaded on to it. The particles were readily taken up by the cells and enabled bioimaging of the host cells. The NPs inflicted higher cytotoxicity than the MTX NCs themselves owing

to the better transport. This work opens a whole new vista in the field of theranostic for administration of drugs during therapy.

5.6 References

(1) Bao, G.; Mitragotri, S.; Tong, S. Multifunctional Nanoparticles for Drug Delivery and Molecular Imaging. *Annu. Rev. Biomed. Eng.* **2013**, *15*, 253–282.

(2) Peng, H.; Liu, X.; Wang, G.; Li, M.; Bratlie, K. M.; Cochran, E.; Wang, Q. Polymeric Multifunctional Nanomaterials for Theranostics. *J. Mater. Chem. B* **2015**, *3* (34), 6856–6870.

(3) Kelkar, S. S.; Reineke, T. M. Theranostics: Combining Imaging and Therapy. *Bioconjug. Chem.* **2011**, *22* (10), 1879–1903.

(4) Huang, H.; Lovell, J. F. Advanced Functional Nanomaterials for Theranostics. *Adv. Funct. Mater.* **2017**, *27* (2).

(5) Wang, A. Z.; Langer, R.; Farokhzad, O. C. Nanoparticle Delivery of Cancer Drugs. *Annu. Rev. Med.* **2012**, *63*, 185–198.

(6) Wang, A. Z.; Langer, R.; Farokhzad, O. C. Nanoparticle Delivery of Cancer Drugs. *Annu. Rev. Med.* **2012**, *63*, 185–198.

(7) Bao, G.; Mitragotri, S.; Tong, S. Multifunctional Nanoparticles for Drug Delivery and Molecular Imaging. *Annu. Rev. Biomed. Eng.* **2013**, *15* (April), 253–282.

(8) Cole, J. T.; Holland, N. B. Multifunctional Nanoparticles for Use in Theranostic Applications. *Drug Deliv. Transl. Res.* **2015**, *5* (3), 295–309.

(9) Lee, E. S.; Gao, Z.; Kim, D.; Park, K.; Kwon, I. C.; Bae, Y. H. Super pH-Sensitive Multifunctional Polymeric Micelle for Tumor pHe Specific TAT Exposure and Multidrug Resistance. **2009**, *129* (3), 228–236.

(10) Torchilin, V. P. Multifunctional, Stimuli-Sensitive Nanoparticulate Systems for Drug Delivery. *Nat. Rev. Drug Discov.* **2014**, *13* (11), 813–827.

(11) Mura, S.; Nicolas, J.; Couvreur, P. Stimuli-Responsive Nanocarriers for Drug Delivery. *Nat. Mater.* **2013**, *12* (11), 991–1003.

(12) Yang, H. Y.; Jang, M.-S.; Gao, G. H.; Lee, J. H.; Lee, D. S. Construction of redox/pH Dual Stimuli-Responsive PEGylated Polymeric Micelles for Intracellular Doxorubicin Delivery in Liver Cancer. *Polym. Chem.* **2016**, *7* (9), 1813–1825.

(13) Blanco, E.; Shen, H.; Ferrari, M. Principles of Nanoparticle Design for Overcoming Biological Barriers to Drug Delivery. *Nat. Biotechnol.* **2015**, *33* (9), 941–951.

(14) Weitman, S. D.; Lark, R. H.; Coney, L. R.; Fort, D. W.; Frasca, V.; Zurawski, V. R.; Kamen, B. a. Distribution of the Folate Receptor GP38 in Normal and Malignant Cell Lines and Tissues Distribution of the Folate Receptor GP38 in Normal and Malignant Cell Lines and. *Cancer Res.* **1992**, *52* (12), 3396–3401.

(15) García-Díaz, M.; Nonell, S.; Villanueva, Á.; Stockert, J. C.; Cañete, M.; Casadó, A.; Mora, M.; Sagristá, M. L. Do Folate-Receptor Targeted Liposomal Photosensitizers Enhance Photodynamic Therapy Selectivity? *Biochim. Biophys. Acta - Biomembr.* **2011**, *1808* (4), 1063–1071.

(16) Doorneweerd, D. D.; Spectus, C. O. N. Discovery and Development of Folic-Acid-Based Receptor Targeting for Imaging and Therapy of Cancer and Inflammatory Diseases. *Acc. Chem. Res.* **2008**, *41* (1), 120–129.

(17) Sahoo, A. K.; Goswami, U.; Dutta, D.; Banerjee, S.; Chattopadhyay, A.; Ghosh, S. S. Silver Nanocluster Embedded Composite Nanoparticles for Targeted Prodrug Delivery in Cancer Theranostics. *ACS Biomater. Sci. Eng.* **2016**, acsbiomaterials.6b00334.

(18) Yang, S. J.; Lin, F. H.; Tsai, K. C.; Wei, M. F.; Tsai, H. M.; Wong, J. M.; Shieh, M. J. Folic Acid-Conjugated Chitosan Nanoparticles Enhanced Protoporphyrin IX Accumulation in Colorectal Cancer Cells. *Bioconjug. Chem.* **2010**, *21* (4), 679–689.

(19) Phillips, D. C.; Woollard, K. J.; Griffiths, H. R. The Anti-Inflammatory Actions of Methotrexate Are Critically Dependent upon the Production of Reactive Oxygen Species. *Br. J. Pharmacol.* **2003**, *138* (3), 501–511.

CHAPTER 6

CONCLUSIONS AND FUTURE PROSPECTS

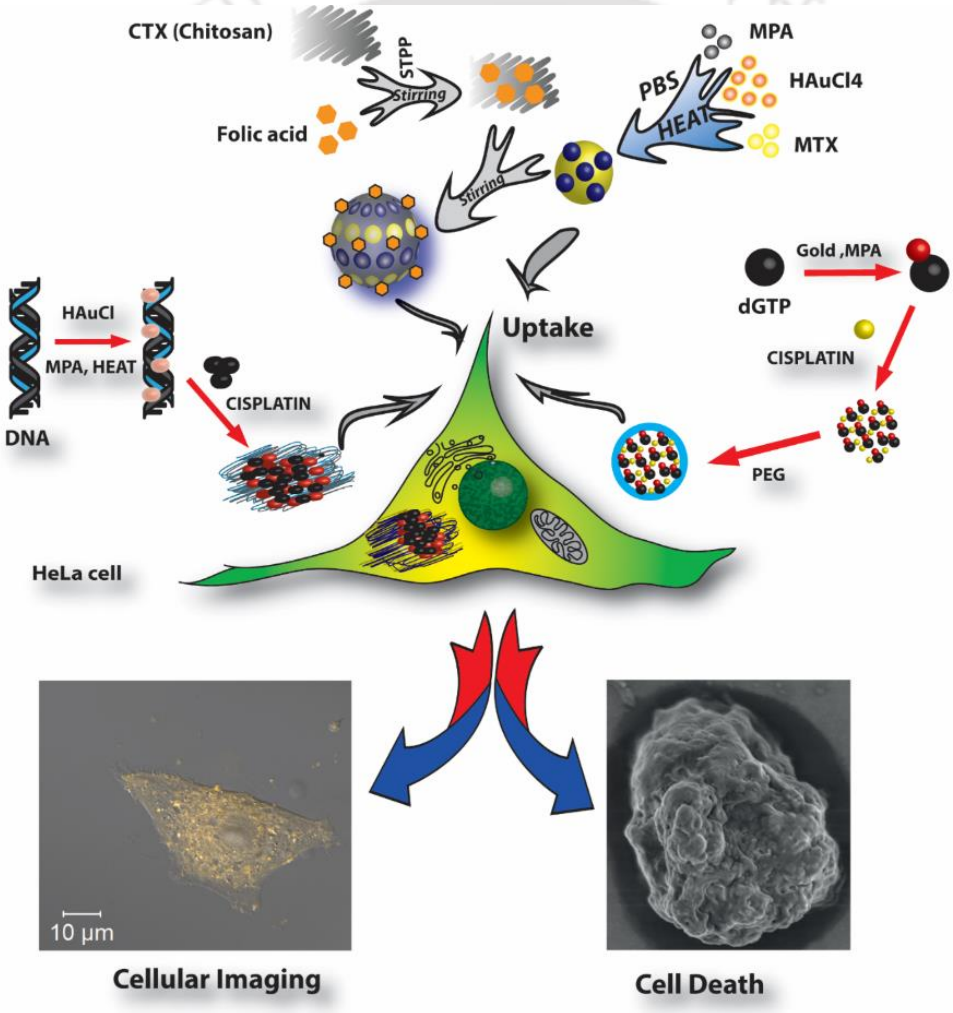

Conclusions and Future Prospects

6.1 Summary of the present study

The present dissertation's prime objective is to develop nanotheranostics that can be synthesized quickly and easily, and would not require much of technical expertise or instruments. For this purpose, gold nanoclusters stabilized on various templates was extensively studied. Initially, the templates used to stabilize the fluorescent gold nanoclusters were biomolecules, first plasmid DNA, then smaller but bio-molecular templates and finally a pharmaceutical drug. The bio-molecular nature of initial templates discounted any template borne inherent cytotoxicity and made sure that the observed cytotoxicity was only due to the drug itself.

In the first part of the dissertation, gold nanoclusters were synthesized on a circular plasmid DNA and then was reacted with the anticancer drug cisplatin to form a composite NPs. The strong affinity of the cisplatin towards the guanine nucleotide in particular was exploited to design the theranostic NPs. Like the traditional nanotheranostics, the initially developed nanotheranostics consisted of two component systems. There were luminescent gold nanoclusters for bioimaging and a drug for therapy. Due diligence was accorded to develop composite nanoparticles in which the drug and the imaging moiety were conjugated in such a manner that only these components were enough to build a nanotheranostic and the concept of loading the drug on pre-developed drug delivery vehicle was thoroughly avoided. The inter component interaction employed for the generation of nanotheranostic was based on existing literature.

On the final part of the dissertation the emphasis was placed on developing an efficient single unit ultra-small nanotheranostic that will act as a superior alternative to

the traditional drugs. These units can act in tandem and will also work in various drug delivery platforms. In this part, we synthesized gold nanoclusters on methotrexate, a traditional anticancer drug, as a template. Due to the mild and quick synthesis procedure, the resultant MTX templated gold nanoclusters not only retained the cytotoxicity of the MTX, but also exerted an enhanced anti-cell proliferative effect with additional feature of being luminescent. These units were ultra-small in size and displayed immense stability in both PBS and in serum (emulating *in vivo* conditions). The composite nanoparticles when incubated with HeLa cells were efficiently taken up facilitating the bioimaging of the cells and their consequent apoptosis mediated death. Interestingly, when these composite nanoparticles were evaluated for their amenability to replace the free drug in a drug delivery vehicle, they displayed a simple but efficient loading and release profile. When incubating with cells besides enabling the bioimaging of the host cells, they inflicted higher cytotoxicity than the free drug and individual components, because of the better transporting aptitude of a drug delivery vehicle.

6.2 Future prospects

- DNA based smart nanocarriers can be further improved making them more refined stimulus responsive nanocarriers.
- The diagnostic modalities of the gold nanoclusters can be expanded into wider application.
- Similarly, several other commercially available anticancer drugs can be tested for developing single unit theranostics.
- Assessment of potential theranostics can be persuaded for *in vivo* application.

PUBLICATIONS AND PRESENTATIONS

Publications and Presentations

Journal Publications

1. **Bandhan Chatterjee,** Amaresh Sahoo, Siddhartha Sankar Ghosh, and Arun Chattopadhyay. "*Interactive Luminescent Gold Nanocluster Embedded ds DNA and Cisplatin as Model Nanoparticle for Cancer Theranostics*" (***RSC Advances, 2016, 6, 113053–113057***).
2. **Bandhan Chatterjee,** Asif Raza and Siddhartha Sankar Ghosh, "*Methotrexate templated Gold Nanoclusters as a single unit Cancer Theranostics*" (***Nanomedicine, 2018, 13, 283-295***).
3. **Bandhan Chatterjee,** Archita Ghoshal, Siddhartha Sankar Ghosh, and Arun Chattopadhyay. *"Interactive dGTP templated Luminescent Gold Nanocluster and cisplatin PEG coated nanoparticle as novel cancer theranostic"* (***ACS Biomater. Sci. Eng. 2018, 4, 1005−1012***).

Conference Presentations

1. **Bandhan Chatterjee**, Amaresh Kumar Sahoo , Siddhartha Sankar Ghosh, and Arun Chattopadhyay, "*DNA based Theranostics: An alternative approach"*, Poster Presentation, **International Conference on Advanced Nanomaterials and Nanotechnology (ICANN 2017)**, December 18-21, 2017, Indian Institute of Technology Guwahati (IIT Guwahati), Guwahati, India.

PERMISSIONS

Permissions

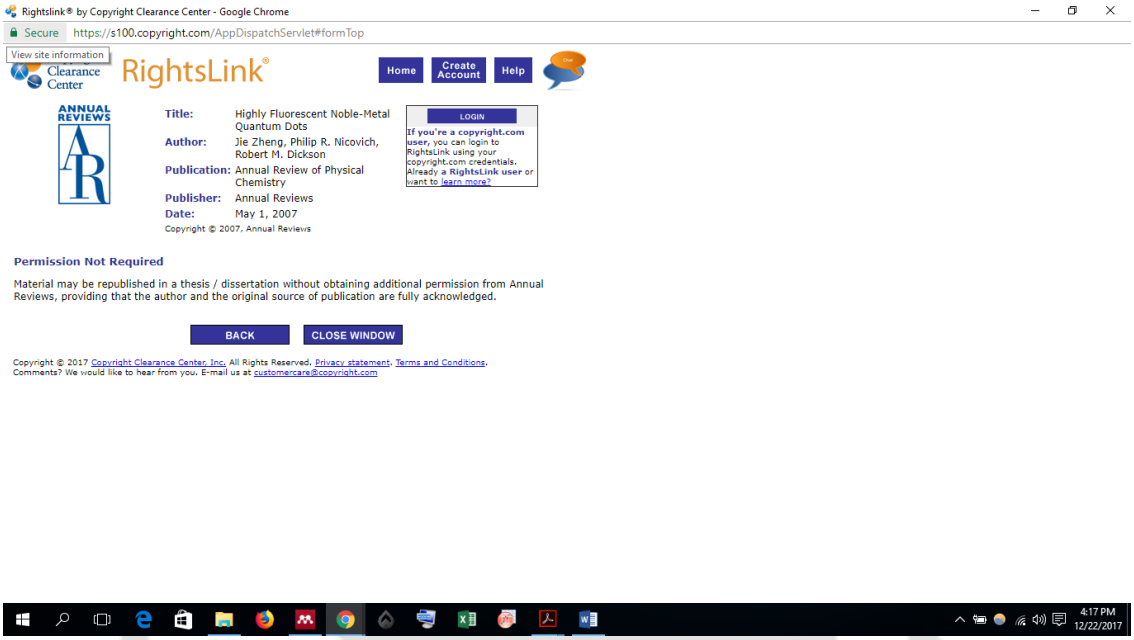

1/9/2018 RE: Copyright Permission

From: "Gill Cockhead" <CockheadG@rsc.org>
Subject: RE: Copyright Permission
Date: Tue, January 9, 2018 6:07 pm
To: "'c.bandhan@iitg.ernet.in'" <c.bandhan@iitg.ernet.in>

Dear Bandhan

The Royal Society of Chemistry (RSC) hereby grants permission for the use of your paper(s) specified below in the printed and microfilm version of your thesis. You may also make available the PDF version of your paper(s) that the RSC sent to the corresponding author(s) of your paper(s) upon publication of the paper(s) in the following ways: in your thesis via any website that your university may have for the deposition of theses, via your university's Intranet or via your own personal website. We are however unable to grant you permission to include the PDF version of the paper(s) on its own in your institutional repository. The Royal Society of Chemistry is a signatory to the STM Guidelines on Permissions (available on request).

Please note that if the material specified below or any part of it appears with credit or acknowledgement to a third party then you must also secure permission from that third party before reproducing that material.

Please ensure that the thesis states the following:

Reproduced by permission of The Royal Society of Chemistry

and include a link to the paper on the Royal Society of Chemistry's website.

Please ensure that your co-authors are aware that you are including the paper in your thesis.

Regards

Gill Cockhead
Publishing Contracts & Copyright Executive

Gill Cockhead
Publishing Contracts & Copyright Executive
Royal Society of Chemistry,
Thomas Graham House,
Science Park, Milton Road,
Cambridge, CB4 0WF, UK
Tel +44 (0) 1223 432134

Title: dGTP-Templated Luminescent Gold Nanocluster-Based Composite Nanoparticles for Cancer Theranostics

Author: Bandhan Chatterjee, Archita Ghoshal, Arun Chattopadhyay, et al

Publication: ACS Biomaterials Science & Engineering

Publisher: American Chemical Society

Date: Mar 1, 2018

PERMISSION/LICENSE IS GRANTED FOR YOUR ORDER AT NO CHARGE

This type of permission/license, instead of the standard Terms & Conditions, is sent to you because no fee is being charged for your order. Please note the following:

- Permission is granted for your request in both print and electronic formats, and translations.
- If figures and/or tables were requested, they may be adapted or used in part.
- Please print this page for your records and send a copy of it to your publisher/graduate school.
- Appropriate credit for the requested material should be given as follows: "Reprinted (adapted) with permission from (COMPLETE REFERENCE CITATION). Copyright (YEAR) American Chemical Society." Insert appropriate information in place of the capitalized words.
- One-time permission is granted only for the use specified in your request. No additional uses are granted (such as derivative works or other editions). For any other uses, please submit a new request.

If credit is given to another source for the material you requested, permission must be obtained from that source.

BACK | CLOSE WINDOW